Electronic recoils in XENONnT

Gaemers, P.W.

Publication date
2024
Document Version
Final published version

Electronic recoils in XENONnT

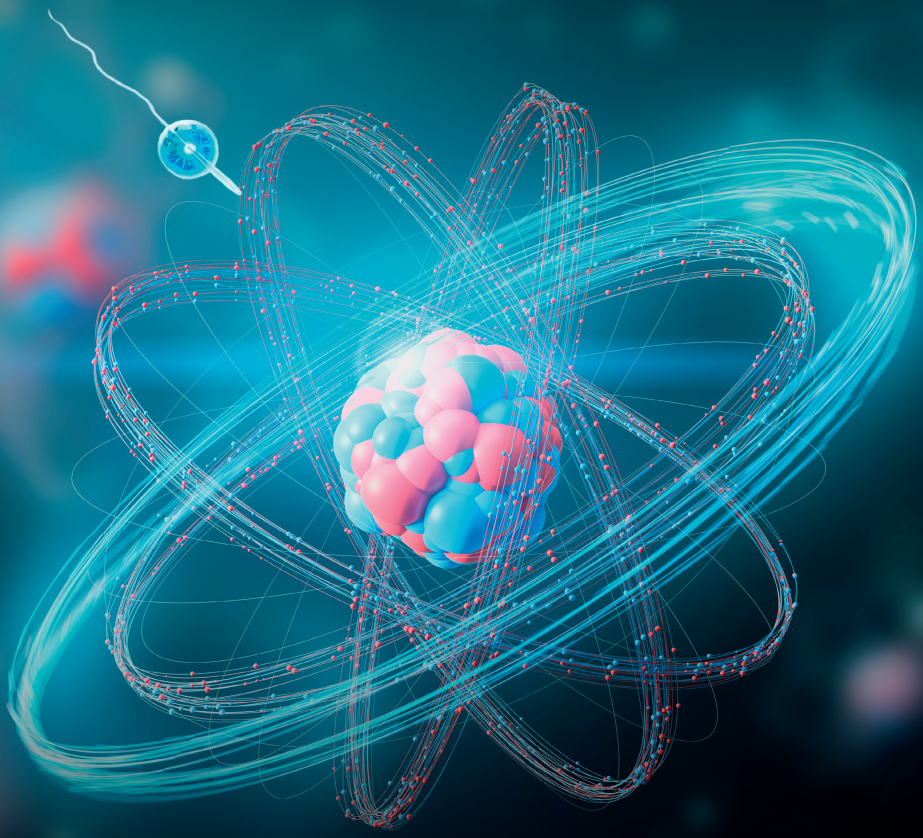

Peter Gaemers

Electronic recoils in XENONnT

ACADEMISCH PROEFSCHRIFT

ter verkrijging van de graad van doctor
aan de Universiteit van Amsterdam
op gezag van de Rector Magnificus
prof. dr. ir. P.P.C.C. Verbeek
ten overstaan van een door het College voor Promoties ingestelde commissie,
in het openbaar te verdedigen in de Agnietenkapel
op dinsdag 21 mei 2024, te 13.00 uur

door Peter Wiebe Gaemers
geboren te UTRECHT

Promotiecommissie

Promotores:	prof. dr. M.P. Decowski	Universiteit van Amsterdam
	prof. dr. A.P. Colijn	Universiteit van Amsterdam
Overige leden:	dr. R. Bruijn	Universiteit van Amsterdam
	prof. dr. N. de Groot	Radboud Universiteit
	prof. dr. M. Vreeswijk	Universiteit van Amsterdam
	dr. T.R. Pollmann	Universiteit van Amsterdam
	dr. C. Weniger	Universiteit van Amsterdam
	dr. C.D. Tunnell	Rice University

Faculteit der Natuurwetenschappen, Wiskunde en Informatica

In memory of

Shivata Upadhyay Grela (1994 – 2016),

Contents

1 Dark Matter **1**
- 1.1 Introduction . . . 1
- 1.2 Big Bang Cosmology . . . 2
- 1.3 Astrophysical evidence . . . 5
  - 1.3.1 Cosmic Microwave Background . . . 5
  - 1.3.2 Rotation curves . . . 8
  - 1.3.3 Galactic collisions . . . 10
  - 1.3.4 Stellar streams . . . 13
- 1.4 Dark Matter candidates . . . 13
  - 1.4.1 Alternatives to Dark Matter . . . 19
- 1.5 Dark matter detection . . . 19

2 Signals in a Dark Matter detector **21**
- 2.1 WIMP Interaction rate and recoil spectra . . . 21
- 2.2 The WIMP-nucleus cross-section . . . 23
  - 2.2.1 The Spin independent interaction . . . 25
  - 2.2.2 The Spin-dependent interaction . . . 25
- 2.3 Low energy electronic recoils . . . 27
  - 2.3.1 Solar axions . . . 27
  - 2.3.2 Neutrino magnetic moment . . . 28
  - 2.3.3 Axion-like particles . . . 30

3 The XENONnT experiment **33**
- 3.1 Liquid xenon detectors . . . 33
  - 3.1.1 Light and Charge yield . . . 36
- 3.2 The XENONnT experiment . . . 37
  - 3.2.1 Time Projection Chamber . . . 37
  - 3.2.2 Cryogenics, purification, distillation, and calibration . . . 41
  - 3.2.3 Veto systems . . . 42
- 3.3 Energy reconstruction . . . 43

4 The XENONnT Data Acquisition System 45
4.1 Overview . . . 47
4.1.1 Design requirements . . . 47
4.1.2 Hardware . . . 50
4.2 Software . . . 56
4.2.1 Redax . . . 57
4.2.2 Readout . . . 60
4.2.3 Strax . . . 61
4.2.4 User interface . . . 63
4.3 Performance . . . 63
4.3.1 Livetime . . . 63
4.3.2 Live processing . . . 65
4.3.3 Electronic noise . . . 66
4.4 Conclusion . . . 69

5 XENONnT Monte Carlo framework 71
5.1 Geant4 . . . 71
5.2 EPIX . . . 74
5.3 WFSim . . . 75
5.3.1 S1 simulation . . . 75
5.3.2 S2 simulation . . . 78
5.3.3 Pulse generation . . . 79
5.3.4 Readout . . . 81
5.4 WFSim validation . . . 82
5.4.1 Doke plot . . . 82
5.4.2 Low ER spectrum . . . 83
5.5 Conclusion . . . 87

6 Radon induced background 89
6.1 Beta decay spectra . . . 89
6.1.1 Beta energy spectrum . . . 91
6.2 Backgrounds . . . 94
6.3 Low energy recoil spectrum . . . 97
6.3.1 Electronic recoils . . . 97
6.3.2 Nuclear recoils . . . 101
6.4 Constraining the ^{214}Pb concentration . . . 104
6.4.1 S1-only alpha analysis . . . 107
6.4.2 Area Fraction Top correction . . . 107
6.4.3 x-y correction . . . 110
6.4.4 Fiducial mass . . . 112
6.4.5 Spectral Fit . . . 112

6.4.6 Rate determination 117
6.4.7 ^{214}Pb rate 120
6.5 Conclusion 121

7 Solar axions **123**
7.1 Flamedisx 124
7.1.1 XENONnT detector model 124
7.2 ER Band fitting 127
7.3 Low ER analysis 128
7.4 Conclusion 134

Summary of Electronic Recoils in XENONnT **135**

Samenvatting van Electronic Recoils in XENONnT **139**

Acknowledgments **143**

Bibliography **145**

1

Dark Matter

1.1 Introduction

One of the oldest questions we try to answer is, "What is the Universe made of? What is happening 'up there'?". Until very recently, this has always been done with the help of light. First, we would look up with our eyes and infer what was happening. With Copernicus, we needed to change our ideas of the Universe, that we were not in the center of everything. Through the centuries, our telescopes have become better and better. They allowed us to observe more details in our solar system and galaxy and much more distant galaxies using different wavelengths apart from visible light. We are not even limited to light anymore. Cubic kilometer-sized detectors let us study the Universe using neutrinos with energies up to almost a million times higher than we can produce in accelerators on Earth. We have even seen black holes and neutron stars merging in recent years using the gravitational waves emitted in this process. These measurements show our model of gravity, general relativity, and our parameterization of the Universe, Λ Cold Dark Matter (ΛCDM), as the best description. However, this leads to a problem. Because ΛCDM needs only six ingredients at minimum for the simplest case, there are two unidentified. One of them is called Dark Matter (DM).

Astronomers discussing unobservable matter goes back to the nineteenth century[1] when father Angelo Secchi talks about dark masses, discoverable by a bright background[2]. Fritz Zwicky was the first to suggest DM is present in larger quantities than ordinary matter. In 1933, at the Mount Wilson Observatory, California, he first measured the radial velocity of galaxies in the Coma Cluster, about 320 million light-years away from Earth, by studying the redshift published by Hubble[3], and applied the virial theorem to estimate the mass of the cluster. The virial theorem relates the potential energy and the

average kinetic energies of a gravitationally bound system[4]. By measuring the average galaxy velocity using the redshift measurements, he found the mass, according to the virial theorem, was much larger than the mass according to the luminous matter. Zwicky proposed the following solution: there was another form of matter, Dark Matter, which we do not see but interacts gravitationally and is present in much higher densities than luminous matter.

DM seems to dominate the Universe. Although we do not directly observe it, it does not interact with light. DM holds galaxies and clusters together in their current form and shapes the cosmic structure we observe at the largest scales, and nothing we know of provides an explanation. Typically, we assume DM to be an unknown elementary particle. This new particle interacts with gravity and, at most, only through the weak force with ordinary matter. Many possible new particles could be DM from theories beyond the Standard Model. For example, the lightest particle predicted by Supersymmetric models (the Neutralino)[5] or the lightest Kaluza Klein state of an extra-dimensional model [6] are viable DM particles. The question is, "Which one is the correct one? Or is it something different entirely?."

This chapter introduces Big Bang Cosmology, the ΛCDM model, and the need for DM with observations to validate this. After that, we will review popular DM particle models, including the most relevant for the XENONnT experiment and this work: Weakly Interacting Massive Particles (WIMPs). Finally, we focus on the primary experimental efforts of detecting DM particles.

1.2 Big Bang Cosmology

In the rest of this section, we will follow the argumentation and derivations given by [7]. In all the following equations, we use the convention $\hbar$=c=1. Figure 1.1 shows the evolution of the early Universe based on the ΛCDM model. The Big Bang model states the Universe started 14 billion years ago in an extremely hot and dense state.

With our current understanding of nature, the earliest time to make statements about is around 10^{-43} s; the *Planck time*, after the Big Bang, to go back further requires a theory of quantum gravity. During this time, the Universe consisted of a plasma with high particle densities and energies, in which particles were continuously created and annihilated. In the first 10^{-38} s, all particle interactions, strong, weak, and electromagnetic, are assumed to be unified in a single interaction, in a *Grand unified theory*[8], with particle energies over 10^{16} GeV. As the Universe expands, particle energies drop, and around 10^{-36} s after the Big Bang, the Universe underwent a phase of extreme expansion of up to a factor of e^{100}, which is called the period of *inflation*.

One μs after the Big Bang, the Universe cooled down enough for particle energies to drop below 1 GeV, after which quarks and gluons started to form hadrons, such as (anti-) protons and (anti-) neutrons. The next phase occurs around 3 minutes after the Big Bang; now, the temperature is low enough for protons and neutrons to bind together to form deuterons and other light elements, such as lithium and beryllium, in smaller quantities. The expansion of the Universe continued for several hundred thousand years, after which the temperature was low enough to form stable atoms from nuclei and electrons.

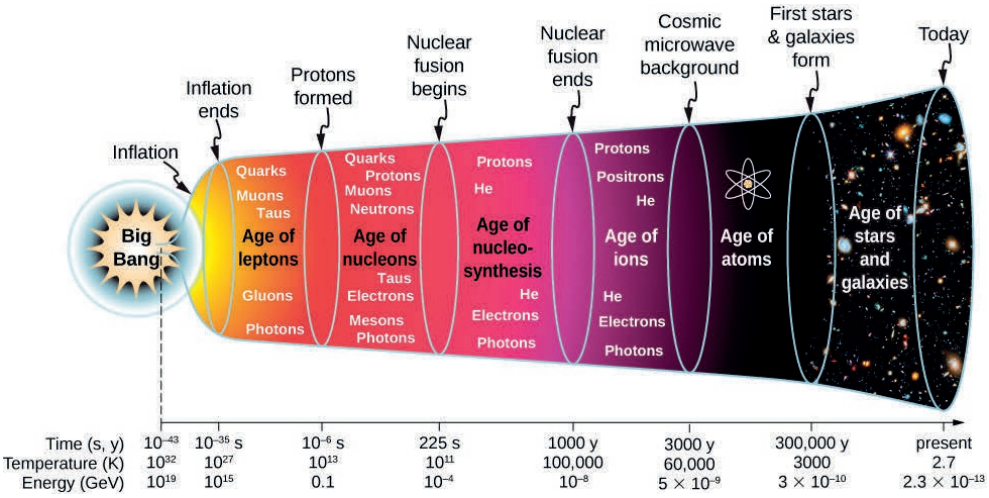

Figure 1.1 Evolution of the early Universe based on the ΛCDM model with the essential events, such as inflation, nucleosynthesis, the emission of the Cosmic Microwave Background (CMB), and the formation of structure, as a function of time and the equivalent temperature and energy on a non-linear scale. [9]

In Big Bang Cosmology, the Universe evolves due to the expansion of space. The metric tensor $g_{\mu\nu}$determines how the space-time interval ds^2 depends on changes to the space-time coordinate x^μ. This relation is given by:

$$ds^2 = g_{\mu\nu} dx^\mu dx^\nu, \tag{1.1}$$

where we follow Einstein's summation convention of repeated indices, in this case, μ,ν. The starting assumption is that the Universe is uniform and isotropic, which is a valid assumption on scales larger than around 100 Mpc[1]. This assumption is also known as the *cosmological principle*. For a isotropic and homogeneous universe, the most general form of the metric tensor is the

[1] about 3.262×10^8 light years

Robertson-Walker metric,

$$ds^2 = dt^2 - R^2(t)\left[\frac{dr^2}{1-kr^2} + r^2(d\theta^2 + \sin^2\theta d\phi^2)\right], \tag{1.2}$$

with the curvature parameter k, and scale factor R . This metric tensor follows as a solution to the Einstein field equations from General Relativity[10],

$$\mathcal{R}_{\mu\nu} - \frac{1}{2}g_{\mu\nu}\mathcal{R} = \frac{8\pi G_N}{c^4}T_{\mu\nu} - \Lambda g_{\mu\nu}. \tag{1.3}$$

In equation 1.3, $\mathcal{R}_{\mu\nu}$ and $\mathcal{R}$ are the Ricci tensor and scalar, $g_{\mu\nu}$ is the metric tensor, G_N is Newton's constant, $T_{\mu\nu}$ is the energy-momentum tensor and Λ the cosmological constant. The equation's left-hand side describes space-time's *curvature*. On the right-hand side, the energy-momentum tensor describes the density and flux of momentum and energy density, and the cosmological constant provides the energy of empty space. For a universe that is isotropic and homogeneous, the energy-momentum tensor takes the form

$$T_{\mu\nu} = \mathrm{diag}(\rho, -P, -P, -P), \tag{1.4}$$

where ρ is the energy density and P the pressure. The field equations can be combined with the Robertson-Walker metric and the above expression for $T_{\mu\nu}$ to get a differential equation for the scale factor R, given by:

$$H^2 = \frac{\dot{R}^2}{R^2} = \frac{8\pi}{3}G_N\rho - \frac{k}{R^2}. \tag{1.5}$$

This equation is known as the *Friedmann equation*, which relates the expansion of space, the Hubble parameter H, to the energy content and curvature of the Universe. The energy density ρ contains matter, radiation, and the vacuum contributions. If the curvature parameter $k < 0$, the right-hand side of Eq.1.5 will be positive. A positive right-hand side corresponds to a universe that keeps expanding forever; this Universe is called *open*. If $k > 0$, there will be a point where the right-hand side of Eq.1.5 will equal 0. In this case, the expansion will stop; this is called a *closed* universe. The final possibility is a universe with $k = 0$. This flat Universe will have its expansion decelerate asymptotically to zero. We can solve the Friedmann equation for k to see how the different scenarios depend on the energy density ρ,

$$k = R^2\left(\frac{8\pi}{3}G\rho - H^2\right). \tag{1.6}$$

The *critical density* is the density corresponding to an flat universe (k=0):

$$\rho_c = \frac{3H^2}{8\pi G_N} \tag{1.7}$$

and the energy density is commonly expressed by the ratio Ω,

$$\Omega = \frac{\rho}{\rho_c} \tag{1.8}$$

The contributions of radiation, matter, and vacuum energy to the energy density are expressed similarly as $\Omega_{r,0}$ (radiation), $\Omega_{M,0}$ (matter), $\Omega_{\Lambda,0}$ (vacuum energy), where the subscript 0 refers to present-day values. The matter component Ω_M is the sum of the baryonic and DM energy density:

$$\Omega_M = \Omega_b + \Omega_{DM}. \tag{1.9}$$

The value of the densities Ω_b (baryons, ordinary matter), and Ω_M is measurable by measuring anisotropies in the CMB, supernovae surveys, or cosmological large scale structure. Experiments inferring the matter distribution in our Universe from optical observations (telescopes) indicate the value of $\Omega_{M,0}$ to be approximately 5% of the critical density. However, other measurements determine this value to be around 30%. A large discrepancy between matter observed through gravity versus light suggests a large fraction of DM in our Universe. Given the theory's success in describing astrophysical phenomena on vastly different length scales, from dwarf galaxies up to large-scale structure of the Universe and measurements of the CMB dark matter is a very well-founded hypothesis.

1.3 Astrophysical evidence

Astrophysical observations support the Dark Matter hypothesis. Here, we describe the cosmic microwave background, rotation curves, galactic collisions, and stellar streams. For a complete overview, see [11].

1.3.1 Cosmic Microwave Background

One of the critical pieces of evidence for dark matter comes from the precision analysis of the Cosmic Microwave Background (CMB) [12]. The CMB is an almost uniform background of microwave radiation reaching us from all directions in the sky. We can use this radiation to measure the density fluctuations of the early Universe with extreme precision, giving access to the Universe when it was 380,000 years old. The CMB photons were emitted at higher energies, but the expansion of the Universe redshifted them to lower energies. After 380,000 years, the Universe cooled down enough to let *recombination* happen when electrons and nuclei (mainly protons) formed electrically neutral atoms (primarily hydrogen). Before this, the Universe

consisted of a plasma with photons continuously being absorbed and re-emitted through the reaction: $H + \gamma \quad \leftrightharpoons \quad p + e^-$.

After recombination, the mean-free path of photons became comparable to the size of the Universe, stopping this process. Photons could travel freely through the Universe without scattering, making the Universe transparent. CMB photons are the oldest light signals we can observe.

The spectrum of the CMB is that of a blackbody emitter with a temperature of 3000 K at the time of emission. Due to the expansion of space, the present-day measured value is 2.7K. For the temperature to be so uniform, there must have been a moment in the history of the Universe when all regions were in causal contact so the Universe could achieve thermal equilibrium. At present day, not all regions of the Universe are in causal contact with each other anymore. To achieve causal contact in the early Universe, but not at present, is explainable by the Universe to have undergone a period of *inflation*, a period of rapid expansion around $t \approx 10^{-35}$ s.

The CMB is not entirely homogeneous either; it has tiny fluctuations. As measurable in its Fourier power spectrum shown in Figure 1.2, the amplitude of fluctuations for different angular scales results from oscillations happening in the plasma of the early Universe. The oscillations (so-called *baryo-acoustic oscillations*) result from the interplay of baryonic matter, dark matter, gravity, and radiation (photons). For these oscillations, dark matter plays an important role. Since it is electrically neutral, it does not interact with the photons but contributes to the amount of gravity other particles experience. The oscillations correspond to density fluctuations, which provided the seed for forming observable galaxies today. The temperature anisotropies of the CMB were done first by COBE (1992) [13], then WMAP (2003) [14], and most recently, the Planck satellite (2015)[15]. Analyzing the temperature fluctuations is done by decomposition into spherical harmonics as a function of l, the angular scale where small values of l correspond to large angles. This decomposition gives a spectrum with multiple peaks from which the parameters of ΛCDM can be fitted and is shown in figure 1.2. The power spectrum has a series of peaks; these are the result of the baryo-acoustic oscillations. How the spectrum of the CMB changes for different values of Ω is shown in Figure 1.3.

Table 1.1 shows the resulting fit parameters. From this, we can determine that our Universe is spatially flat, the expansion is accelerating, and its composition is 5% baryonic matter, 27% cold dark matter, and 68% dark energy. Baryonic matter is the matter planets, stars, interstellar gas, and we are made of. Dark energy is a component that counteracts gravity and pushes galaxies apart, resulting in the expansion of the Universe. Apart from the baryon and DM density, the other parameters are the sound horizon at last scattering, the

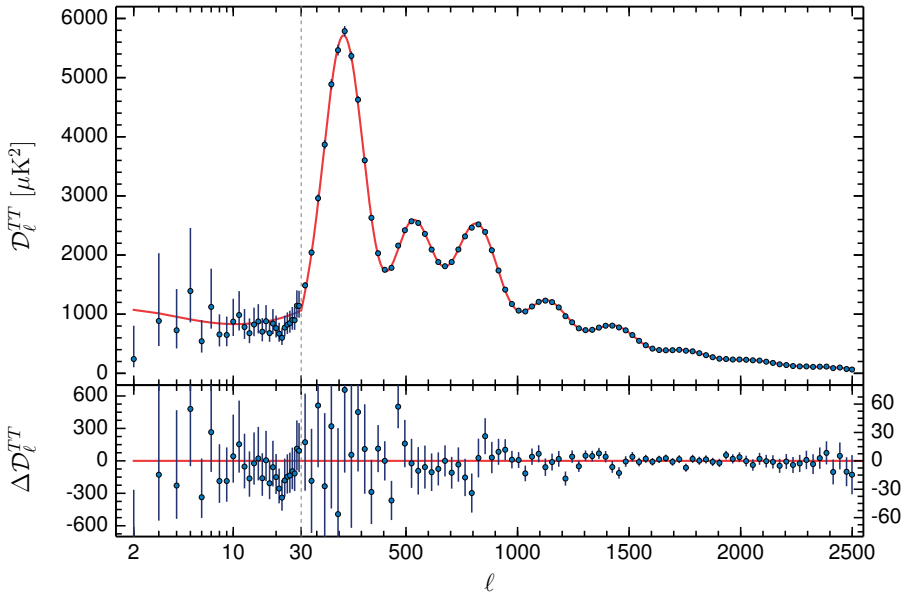

Figure 1.2 The Planck CMB temperature anisotropies (blue dots) with the best fit from ΛCDM in red in the top panel. The bottom panel shows the residuals of the fit. The position and amplitude of the peaks provide strong constraints on the energy density and other ΛCDM model parameters. From [15].

reionization optical depth, the primordial curvature perturbation amplitude, and the scalar spectral index. The sound horizon at last scattering is the maximum distance a soundwave could travel before recombination. The reionization optical depth is the distance photons could have traveled before scattering on free electrons. The primordial curvature perturbation amplitude refers to the original amplitude of the density fluctuations during inflation. The scalar spectral index measures how the density fluctuations vary with scale.

Parameter	Symbol	Value
Baryon density	Ω_{b}	0.03309 ± 0.00002
Dark matter density	Ω_{c}	0.1781 ± 0.0022
Sound horizon at last scattering	$100\ \theta_{\mathrm{MC}}$	1.04077 ± 0.00032
Reionization optical depth	τ	0.079 ± 0.017
Primordial curvature perturbation amplitude	$\ln(10^{10}\mathrm{A_s})$	3.094 ± 0.034
Scalar spectral index	n_s	0.9645 ± 0.0049
Dark energy density	Ω_Λ	0.6844 ± 0.0091
Matter density	Ω_{m}	0.3156 ± 0.0091

Table 1.1 The top group lists the six parameters for the simplest ΛCDM model from the Planck satellite observations. The bottom group shows the constraints on two derived parameters [15]

.

The amount of dark matter in the Universe shifts the amplitude and the position of the peaks in the CMB spectrum. This high-precision CMB measurement forms a powerful constraint for cosmological theories. In particular, the third peak at $l \approx 800$ is not seen in models without dark matter. This is illustrated in panels c and d from Figure 1.3, where the third peak is unaffected by a change in the baryon density (panel c) but varies widely for a change in the matter density (panel d). Also, alternative theories in which gravity is modified to describe astrophysical observations (see below) cannot easily fit this spectrum.

1.3.2 Rotation curves

The rotational velocity of an object at a distance r around the center of a mass distribution M(r) is given by:

$$v(r) = \sqrt{\frac{G_N M(r)}{r}}, \tag{1.10}$$

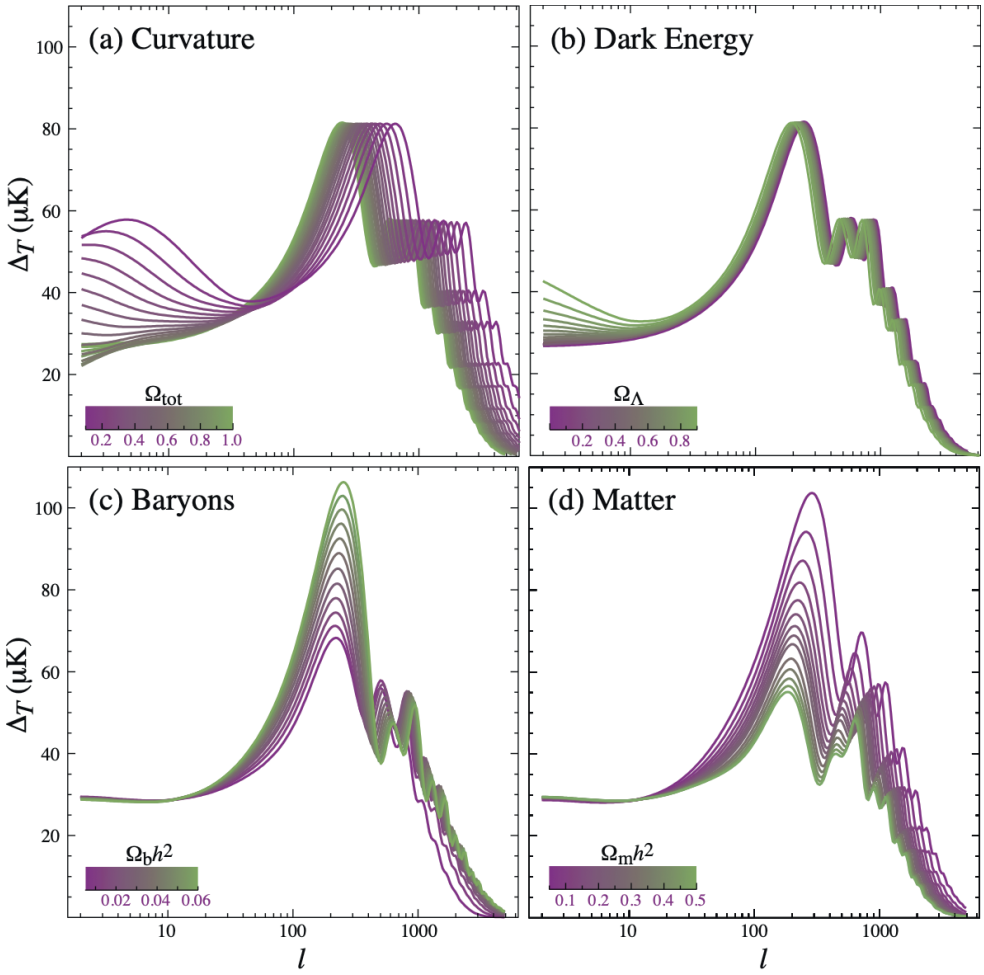

Figure 1.3 CMB power spectrum for different values of (a) Curvature (total energy density Ω) and different values for one of the components $\Omega_\Lambda(b)$, Ω_b (c) and Ω_M(d). From [16].

with G_N Newton's constant. Most of the luminous matter is concentrated in the central bulge of a typical galaxy. Therefore, the mass enclosed as a function of r will rise steeply at low r until r is larger than the radius of the central bulge. After this, the enclosed mass will remain almost constant. For $v(r)$ it increases as long as M(r) increases, and a decrease $\propto r^{-1/2}$ when M(r) becomes constant.

In 1970, Vera Rubin measured the rotation curves of spiral galaxies focusing on H-II regions[17], which are regions of interstellar ionized hydrogen at different distances to the galaxy centers. After an initial rise, the rotation curves stayed flat or went up for higher radii rather than going down as was expected based on the luminous matter distribution[18]. In the early 1980s, evidence for non-luminous matter mounted with measurements of the redshift of radio emission from the 21 cm of neutral hydrogen gas far beyond the optical radii of the galaxy[19]. These measurements can be explained by a dark component distributed homogeneously throughout the galaxy (the "dark matter halo").

Figure 1.4 shows a rotation curve for the Milky Way galaxy[20]. The red line shows the best-fit rotation curve; the blue line is the baryonic contribution, and the yellow is the dark matter component of the total rotation curve. These results also show missing mass close to the galactic center. The most likely interpretation of this is a stellar overdensity of $\sim 0.2 \times 10^{10}$ $M_\odot$ [20]. The baryonic contribution is the sum of two parts: the bulge, with its maximum at $\sim$1 kpc, and the disk, with its maximum at $\sim$7 kpc. The edge of the disk is at $\sim$18 kpc[21]. At distances >8 kpc, the dark matter contribution to the rotation curve becomes dominant and extends up to [22].

1.3.3 Galactic collisions

Galaxy clusters are large groups of galaxies bound together gravitationally. The typical baryonic mass is between 10^{14} and 10^{18} $M_\odot$. The most significant mass component is ionized interstellar gas, about 15% of the total, while the stellar component is between 1-2%. Two galaxy clusters can collide, and we can infer the mass distribution from the dynamics of such an event. The stars pass by each other without any collisions in such an event. However, the interstellar gas does collide. These collisions lead to a separation of luminous matter and dark matter. In the collision, the gas ionizes, causing the emission of X-rays.

The mass distribution can be measured using gravitational lensing. Gravitational lensing is the process of the path of light being distorted by an object between the source and the observer. The gravity of the intermediate object changes the light path, resulting in a distortion of the image seen by the observer. The amount of distortion allows a measure of the mass distribution of the lensing object. When we compare the observed mass distribution from

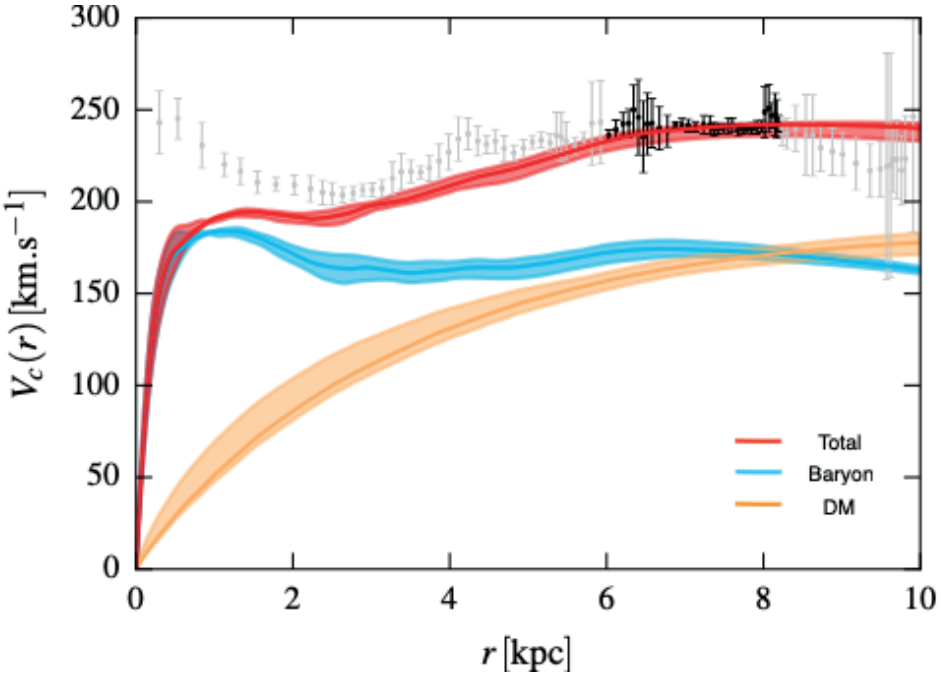

Figure 1.4 The data points show the rotation curve of the Milky Way galaxy from [23]. The rotation curve has three dominant components: the bulge(r $<$ 2 kpc), the disk (2 $<$ r $<$ 10 kpc), and the DM halo (r $>$ 10 kpc). Black data points are used to fit the dark matter halo. The red, blue, and yellow curves show the total best fit, the baryonic component, and the dark matter component of the rotation curve. From [20]

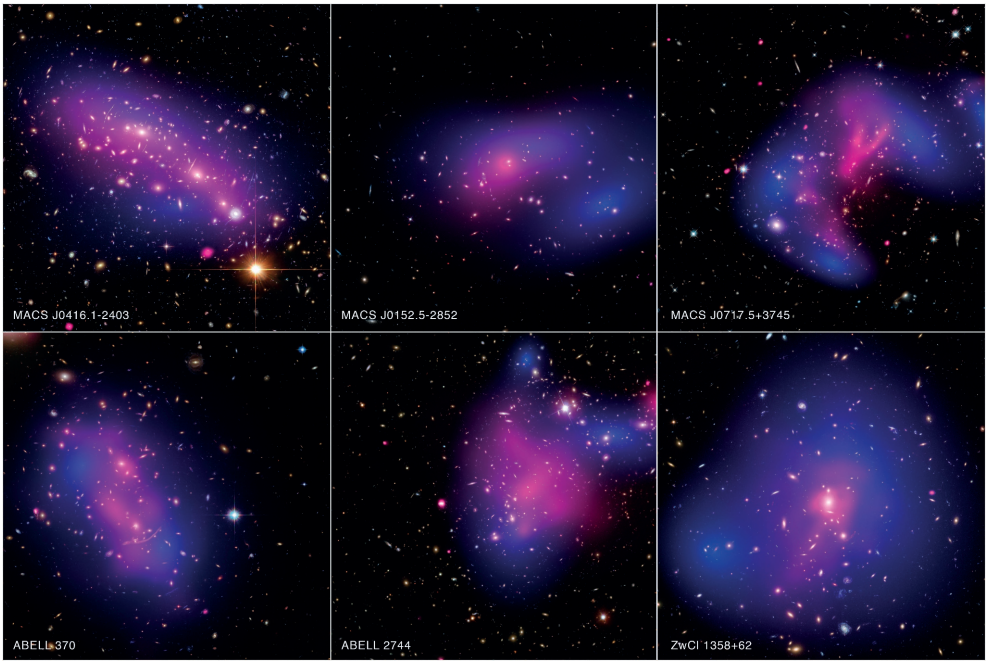

Figure 1.5 Images of six different galaxy cluster collisions. The blue color indicates the gravitational distribution derived from the Hubble space telescope measurements, and the pink color indicates the distribution of hot gas measured by the Chandra Observatory. These images indicate interstellar gas and visible galaxies are not the dominant sources of gravity in galaxy clusters. Taken from [24].

lensing in the galaxy cluster with the distribution of the x-rays, the gravity source seems to have passed through each other without any interactions. A famous example is the observations of the Bullet cluster[25]. In 2015, the Chandra and Hubble space telescopes measured 72 colliding galaxy clusters, all showing similar behavior[24]. Figure 1.5 shows the gravity (blue) and matter (pink) distributions of 6 different galaxy cluster collisions. This observation again supports a dark matter component responsible for the majority of gravity, about five times more than luminous matter, no (or extremely low) self-interactions, and moving at non-relativistic ("cold") velocities.

1.3.4 Stellar streams

A prediction of cold DM is the existence of many dark matter substructures inside galactic halos[26]. These subhalos would have very few stars, making them hard to observe directly. One of the methods of setting constraints on these types of subhalos is by analyzing the perturbations on stellar streams. Stellar streams are the remnants of the tidal disruption of dwarf galaxies or globular clusters merging into a galaxy. These stellar streams are lone, almost one-dimensional bands with a very uniform stellar distribution[27], and nearby dark subhalos will gravitationally perturb their stellar density. The power spectrum of the density fluctuations can measure the mass function of dark subhalos[28]. Figure 1.6 shows the subhalo mass function obtained from the analysis of the stellar steam perturbations of streams GD-1 and Pal 5, together with measurements of satellite galaxies of the Milky Way and strong lensing measurements from external galaxies converted to the subhalo mass function of the Milky Way[29]. The measures strongly constrain alternative DM models, which are shown in black, which predict a deviation from the WIMP CDM line.

1.4 Dark Matter candidates

All the evidence for DM is indirect, meaning only its gravitational effect on the luminous matter has been observed. We still do not know what the particle nature of dark matter is.

Based on the astrophysical measurements, we can make some general statements about the properties of DM:

- **Dark** - DM is not part of the luminous matter of galaxies and clusters observed today. The CMB spectrum measurements require only a gravitational component since DM density perturbations would not have

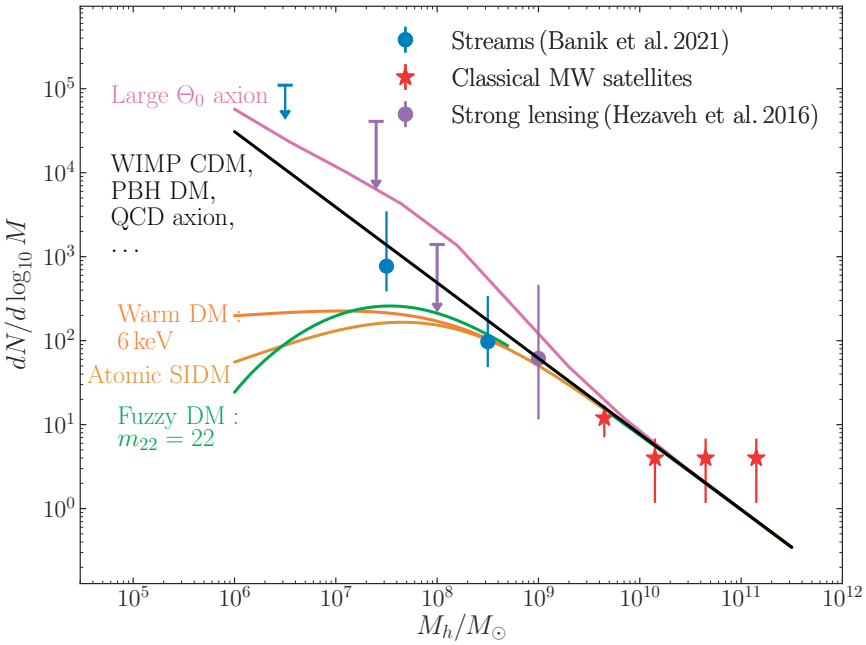

Figure 1.6 Sub halo mass function (SHMF) of the Milky Way out to 300 kpc. Data points come from stellar stream measurements on GD-1 and Pal 5 (blue), Milky Way satellite galaxies (red), and strong lensing measurements converted to constraints on the Milky Way. Theoretical models from well-known CDM models, such as WIMP, primordial black holes, and QCD axions (black), are included. Several theoretical DM models predict different SHMF as Large θ Axions (pink), Warm DM (orange), Fuzzy DM (green), and Atomic SIDM (yellow). Measurements at low SHMF provide strong constraints on DM models predicting a deviating abundance of DM subhalos. From [29].

formed if DM had experienced radiation pressure from Standard Model (SM) particles. DM is allowed to interact with matter at most weakly.

- **Cold** - DM should be cold i.e. non-relativistic by red-shift $\sim 10^7$. If DM had been warm, the subsequent structure formation in the Universe would have been different, like the different subhalo mass fraction, as shown in Figure 1.6.

- **Collisionless** - DM cannot have a significant self-interaction cross-section. DM self-interactions would have resulted in radiation pressure, preventing DM density perturbations from forming.

- **Stable** - DM particles should be stable with respect to the age of the Universe.

- **Not interfere with Big Bang Nucleosynthesis** - The abundances of light particles formed during Big Bang Nucleosynthesis depend on DM through its effect on the expansion rate. The physical processes involved are well understood and should not contribute significantly due to DM interactions.

This still leaves a lot of questions open, such as if dark matter is a particle. What is its mass or spin? Or what if dark matter consists of multiple particles? The range of allowed masses is enormous, from 10^{-22} eV to 10^{15} GeV, 46 orders of magnitude. Figure 1.7 shows different dark matter particle candidates over a wide mass range. The most interesting for this thesis is the WIMPs in the GeV to 100 TeV range. The point of this section is to give a very brief overview of the possibilities. More in-depth information about particular models can be found in the references cited at the end of each paragraph.

Ultralight DM The class of DM models with a mass range between $\sim 10^{-22}$ eV up to ~ 3 keV is known as *Ultralight Dark Matter* (ULDM). In these models, DM is assumed to be a boson and, because of its small mass, can be in a superfluid state or form Bose-Einstein condensates on galactic scales[31]. This behavior will cause a deviation of the standard CDM predictions on length scales below 10 Mpc, where observational constraints are weaker[32][33].

One of the most famous examples of Ultralight DM is the *axion*. Axions were initially not invoked to solve the dark matter problem but for another reason. In Quantum Chromodynamics (QCD), the theory of the strong interaction, Charge-Parity (CP) symmetry, seems to be conserved (known as the *strong-CP problem*). At the same time, there is no reason for QCD to do so from a theoretical perspective. The theory also predicts a dipole moment

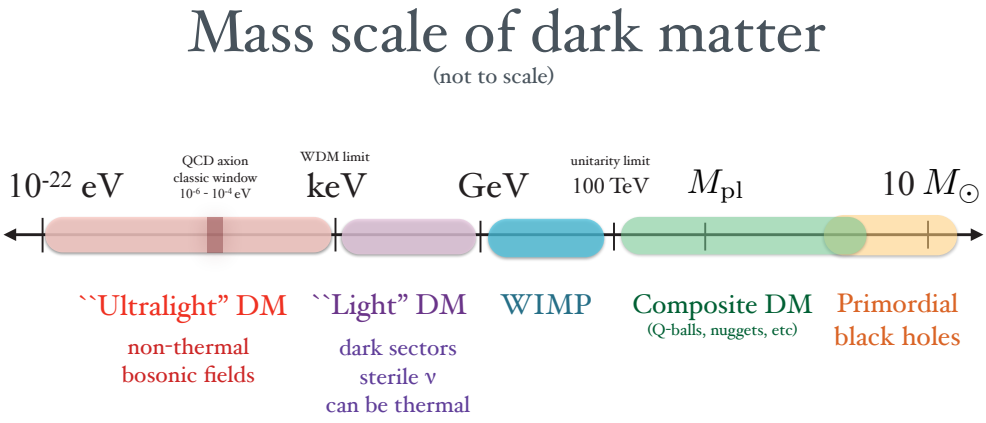

Figure 1.7 DM particle candidates over the complete mass range. Taken from [30]

for the neutron about ten orders of magnitude higher than the upper limits from experiments[34]. In 1977, Peccei and Quinn[35] hypothesized the addition of another symmetry, now called Peccei-Quin, which is spontaneously broken. A broken symmetry will result in a new particle through the Goldstone theorem[36]: in this case, the axion. The scale at which this symmetry would be broken was initially proposed around the electroweak scale (246 GeV). Since the mass is inversely proportional to the symmetry-breaking scale, this results in a particle with a mass of around 200 keV. Astrophysical observations excluded this hypothesis, as this would allow axion emission from red-giant stars, affecting its evolution in the Hertzprong Russel diagram and the lifetime of red giants[37]. Laboratory experiments further constrain the allowed axion mass range[38]. With the addition of the Axion, the allowed CP violation will be tiny: this will solve the strong CP problem. As a bonus, the Axion is also a viable dark matter candidate. Since the production mechanism is non-thermal, they would be cold in the early Universe. The currently allowed mass range is between 1 μeV to 3 meV. See [39] for a review on Ultralight DM.

Fermions have a lower mass bound of 100 eV[40]. A lower mass would increase DM's number density and velocity so that DM would not be bound to a galaxy. However, ultra-light fermionic dark matter models exist by assuming many distinct fermion species with (near) degenerate masses.[41]

Light DM The DM mass range of $\mathcal{O}$(keV) - 10 GeV, *light DM*, separates itself from ULDM in two ways. First, light DM can be either a fermion or a boson, while ULDM has to be bosonic. The maximum velocity of DM is constrained by the requirement to be bound within a galaxy. Fermions must

obey the Pauli exclusion principle, which, together with the velocity constraint, leads to a maximum number density of DM. Data from Dwarf Spheroidal Galaxies put the lower limit on fermionic DM models between $0.147^{+0.044}_{-0.026}$ - $0.468^{+0.137}_{-0.082}$ keV [42]. Second, DM produced thermally by the heat bath in the early Universe requires a DM mass of $\mathcal{O}$ (keV) to obtain the number density consistent with observations.

Typical DM models are *dark sector models* and *sterile neutrinos*. Suppose DM is produced thermally in the early Universe. In that case, dark sector models require a new light mediator since weak scale interactions would result in a number density whose energy density is higher than observations of Ω_{DM}(Lee-Weinberg bound) [43]. The dark photon is an often studied dark sector model, which kinematically mixes with the Standard Model photon [44].

Sterile neutrinos are another DM candidate[45]. Since sterile neutrinos only very weakly interact with ordinary matter, if at all, sterile neutrinos would have never been in thermal equilibrium with SM particles. Depending on the sterile neutrino model, they can be hot, warm, or cold dark matter. For a review, see [46] [47].

WIMP *Weakly Interacting Massive Particles* (WIMPs) are a class of particles hypothesized to be dark matter, with an expected mass between 1 GeV - 100 TeV[30]. The Standard Model does not contain a WIMP particle. However, many theories beyond the standard model do have a WIMP particle. The lightest particle predicted by Super Symmetry[48], the lightest Kaluza-Klein particle from theories with extra dimensions[49], and the lightest particle in Little Higgs models[50] are all WIMP candidates. As with the axion, none of these theories were proposed with the intent of explaining dark matter. The dark matter candidate comes for free in these theories.

WIMPs are assumed to be thermally produced in the early Universe and are now moving with non-relativistic velocities[51]. The early Universe ($t < 1$ ns) was a hot plasma of relativistic particles. At such high temperatures, particle masses are negligible with respect to their energy, and all particle species are in equilibrium. The only drop in number density comes from the expansion of space; the expansion leads to a cooling of the Universe. After the temperature drops below the mass of a particle species, thermal production will no longer be possible, and this particle will not be in equilibrium with the rest of the Universe. The number density will still be high enough for annihilation to occur. After further expansion, the annihilation probability drops to zero, and the density (the so-called *relic abundance*) remains constant. This process is called *freeze out*, and the remaining particle density depends on the particle species' initial interaction cross-section. Figure 1.8 shows the density of a WIMP

particle for three cross-sections leading to three different WIMP densities at present. Thermal production of WIMPs leads to the measured relic density of $\Omega_{\mathrm{DM}} \sim 0.3$ for interaction cross sections σ of the order of the Electroweak scale of $\sim 10^{-39}$ cm^2.

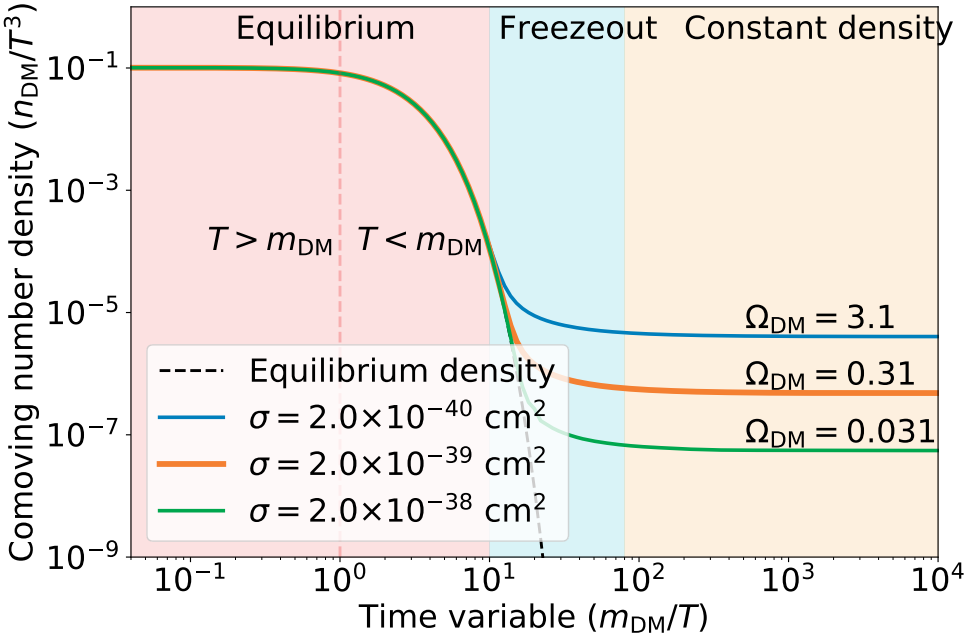

Figure 1.8 The WIMP freeze-out process. The comoving number density, $\mathrm{n}_\chi/\mathrm{T}^3$ as a function of time, in $\mathrm{m}_\chi/\mathrm{T}$, as the temperature is inversely proportional to time. The lines show the different possible relic densities for various cross-section values. The colored region represents the time in which dark matter was in equilibrium with the Universe (red), the time of freeze-out (blue), and the period of constant density (yellow). Method based on [52], source code available at [53].

Composite DM The dark sector particles are not limited to just dark photons. One of the original ideas of what constitutes DM was dark atoms and nuclei [54]. The simplest composite dark matter model has dark protons, electrons, and photons to form dark hydrogen[55] from a hidden $U(1)$ gauge symmetry. However, DM candidates also include dark mesons, dark baryons, and dark glueballs[56].

Primordial black holes Primordial black holes are black holes formed in the very early Universe, meaning before Big Bang Nucleosynthesis. The merger of such black holes produces gravitational waves detectable by experiments

such as LIGO and VIRGO. If all DM in the Universe were made of primordial black holes, the merger rate of binary black holes would be higher than is observed. It is still possible for primordial black holes to make up a fraction of DM.

1.4.1 Alternatives to Dark Matter

There is another possibility to explain, e.g., rotation curves. Alternative formulations of gravity alleviate the need for a dark matter component. These theories include Modified Newtonian Dynamics (MOND)[57] or its relativistic formulation Tensor-Vector-Scalar Gravity (TeVeS)[58]. Alternative gravity models can adequately explain rotation curves but fail to account for galaxy cluster collisions and the CMB power spectrum[59]. In addition, these theories are in tension with measurements of gravitational waves and their electromagnetic counterparts. For example, a delay of 1.7 s was observed between the gravitational waves and gamma-ray signals from neutron star merger GW170817[60]. The class of alternative formulations of gravity called "dark matter emulators"[61] in which gravitons couple to a different metric tensor than ordinary matter, predicting a delay of 400 days [62].

1.5 Dark matter detection

The parameter space is shrunk considerably with the restriction of only considering WIMPs. However, it still covers approximately five orders of magnitude in mass and cross-section. No experimental technique is sensitive to the full parameter range; therefore, multiple experiments must be employed to search for WIMPs. A rough classification of the different types of searches is production, annihilation, and scattering.

Production Particle colliders can produce dark matter during the collision of, e.g., protons. Its signature would be missing energy-momentum since the dark matter particle does not interact with the detector. For such an event, the momentum of the detected decay products will not add up to zero for electron-positron colliders or zero transverse momentum for a hadron collider. Even if such an event is found, whether this would be a DM or another new particle is uncertain. For a review see [63][64].

Annihilation DM can annihilate too Standard Model particles when interacting with anti-DM particles. Annihilation searches are based on DM/anti-DM annihilation in space regions with very little matter to minimize astrophysical backgrounds, such as galactic halos or with a very high expected dark matter excess, like in the galactic center. In the annihilation process, such a process should produce an excess of particles like gamma rays, neutrinos, or positrons.

Accurate background modeling is extremely challenging: many astrophysical backgrounds produce similar signals. The result can set limits on the thermally averaged annihilation cross-section $\langle \sigma_{\mathrm{A}} \mathrm{v} \rangle$ under present-day dark matter velocities. This field has many possible excess signals, such as from FermiLAT[65]. However, given the uncertainties in the astrophysical backgrounds, it is hard to interpret these as hints of dark matter.

Scattering Scattering searches use Earth-based detectors looking for a scattering signal from a WIMP interacting with an atomic nucleus. The idea originated with Goodman and Witten in 1985[66]. Recoiling off the electron shell of atoms is highly suppressed due to the large difference in mass between the DM and the electron, except for specific models like leptophilic dark matter[67]. These experiments primarily constrain the DM-nucleon cross-section σ_{N}. The signal is extremely small (in the keV-MeV range) and rare (expected rates in the order of 1/year); therefore, these detectors are built to have ultra-low radioactive backgrounds and are operated in underground laboratories to minimize the flux of cosmic muons.

2

Signals in a Dark Matter detector

This chapter discusses potential signals in a Dark Matter (DM) detector. The obvious signals of Weakly Interacting Massive Particles (WIMPs) interacting with ordinary matter are the central focus of most DM direct detection experiments. If DM is made of WIMPs, they are hypothesized to have a weak interaction with ordinary matter, which can be either spin-independent or spin-dependent. The rate of WIMP-nucleus interaction is dependent on various factors, such as the dark matter density, WIMP-nucleon cross-section, and the velocity distribution of WIMPs. In this chapter, we present the theoretical background for the expected WIMP interaction rate and recoil energy for three different target atoms: xenon, argon, and germanium. These materials are commonly used as the target in direct detection experiments for DM. We include the calculations for the spin-independent and spin-dependent contributions to the WIMP-nucleus cross-section. Due to the low-background nature of a dark matter experiment several other interesting physics searches become accessible. We also discuss more exotic signals from solar axions, neutrino magnetic moment, and axion-like particles.

2.1 WIMP Interaction rate and recoil spectra

In the standard halo model, the DM density is assumed to be spherical with a density profile of $\rho \propto 1/r^2$. This is a density profile that matches the flat rotation curves that have been observed. DM-scattering experiments typically assume the standard halo model with parameters shown in Table 2.1. According to more recent measurements, the values should have slightly different values[68]. To ensure a fair comparison of results from different experiments, a convention

has been adopted for the current direct detection searches given by[69]. DM-scattering experiments do not quantify the impact of these differences. For light DM models, there can be significant effects; they only produce measurable signals if their speeds are at the far end of the distribution, which can be significantly affected by a tiny shift in the distribution.

Parameter	Standard halo model[70]	Standard halo model ++[68]	Current convention [69]
ρ (GeV/(c^2 $\times$ cm^3))	0.3	0.55 $\pm$ 0.17	0.3
v_0 (km/s)	220	233 $\pm$ 3	238
v_E (km/s)	232	246.1	298
v_{esc} (km/s)	544	528^{+24}_{-25}	544

Table 2.1 Table with standard halo model parameters compared with the updated standard halo model++[68] and a recent convention[69]. ρ is the DM density, v_0 the modal DM velocity, v_E the velocity of Earth with respect to the Galactic center, and v_{esc} the escape velocity of the Milkey Way.

The *differential event rate*, the expected interaction rate of WIMPs scattering on a target nucleus with mass m_N, as a function of the deposited energy, is given by[70]:

$$\frac{dR}{dE_R} = \frac{\rho}{m_\chi}\frac{1}{m_N}\int d^3\mathbf{v} F(\mathbf{v})|\mathbf{v}|\frac{d\sigma}{dE_R}(\mathbf{v}), \tag{2.1}$$

with $F(\mathbf{v})$ the dark matter velocity distribution in the laboratory frame, $\frac{dR}{dE_R}$ the differential rate and $\frac{d\sigma}{dE_R}$ the differential cross-section. The minimum WIMP velocity to induce a recoil on a nucleus with mass m_N is given by:

$$v_{\min} = \sqrt{\frac{E_R m_N}{2\mu^2}}, \tag{2.2}$$

with μ, the WIMP-nucleus reduced mass, and E_R the recoil energy i.e., the energy deposited in the detector.

The velocity distribution $F(\mathbf{v})$ determines the energy DM can deposit in a detector. The *standard halo model* assumes the distribution F(v) of DM particle velocities v_g in the galactic rest frame is a Maxwell-Boltzmann distribution with a cutoff at an escape velocity v_{esc}[71]. This gives:

$$F(v) = \begin{cases} k\frac{1}{\sqrt{\pi v_0}^3}\exp(\frac{-v^2}{v_0^2}), & v < v_{\text{esc}}, \\ 0, & \text{otherwise} \end{cases} \tag{2.3}$$

with v_0 the modal (most probable) DM velocity, v the DM velocity in the galactic rest frame and k a normalization constant given by[70]:

$$k = \mathrm{erf}(\frac{v_{\mathrm{esc}}}{v_0}) - \frac{2}{\sqrt{\pi}}\frac{v_{\mathrm{esc}}}{v_0}\exp\left(-\frac{{v_{\mathrm{esc}}}^2}{v_0}\right). \tag{2.4}$$

DM with a velocity higher than the escape velocity of the Milky Way is not gravitationally bound to the Milky Way. Thus, the distribution is truncated for velocities above the escape velocity. The differential rate can subsequently be written as:

$$\frac{dR}{dE_{\mathrm{R}}} = \frac{N_A\rho_0}{A_T m_\chi}\frac{1}{E_0 r}\exp\left(\frac{-E_{\mathrm{R}}}{E_0 r}\right), \tag{2.5}$$

The orbit of Earth around the Sun with a velocity of ~ 30 km/s, resulting in an annual modulation of the expected WIMP rate of a few percent[70]. The variation of the differential event rate is approximated by[72]:

$$\frac{\mathrm{d}R}{\mathrm{d}E_R} \approx \left\langle \frac{\mathrm{d}R}{\mathrm{d}E_r} \right\rangle [1 + \Delta(E_r)\cos(\omega(t - t_0))], \tag{2.6}$$

with $\left\langle \frac{\mathrm{d}R}{\mathrm{d}E_r} \right\rangle$ the average differential event rate, $\Delta(E_r)$ the annual modulation amplitude (~ 0.05), ω=2π/yr, and t_0 the time when Earth moves fastest with respect to the DM rest frame (June). The movement of Earth with respect to the DM Halo is illustrated in Figure 2.1.

2.2 The WIMP-nucleus cross-section

The differential event rate, Eq. 2.1, depends on the WIMP-nucleus cross-section. This, in turn, depends on the WIMP-quark interaction with hadronic matrix elements to describe the dynamics of quarks and gluons inside a nucleon. The leading order contributions to the WIMP-nucleus are the Spin Independent (SI) and Spin-Dependent (SD) interactions. Experimental measurements assume a WIMP can undergo only either SI or SD, not both. At small momentum transfer q, the WIMP scatters to all nucleons coherently. While at higher values of q, coherence is lost and the WIMP will only scatter on the part of the nucleons. The *form factor* F is added to account for such loss of coherence. The resulting WIMP-nucleus cross-section becomes[74]:

$$\frac{d\sigma}{dE_{\mathrm{R}}} = \frac{m_N}{2\mu^2 v^2}(\sigma_0^{\mathrm{SI}} F_{\mathrm{SI}}^2(E_{\mathrm{R}}) + \sigma_0^{\mathrm{SD}} F_{\mathrm{SD}}^2(E_{\mathrm{R}})), \tag{2.7}$$

with $\sigma_0^{\mathrm{SI/SD}}$ the WIMP-nucleon cross section at zero momentum transfer.

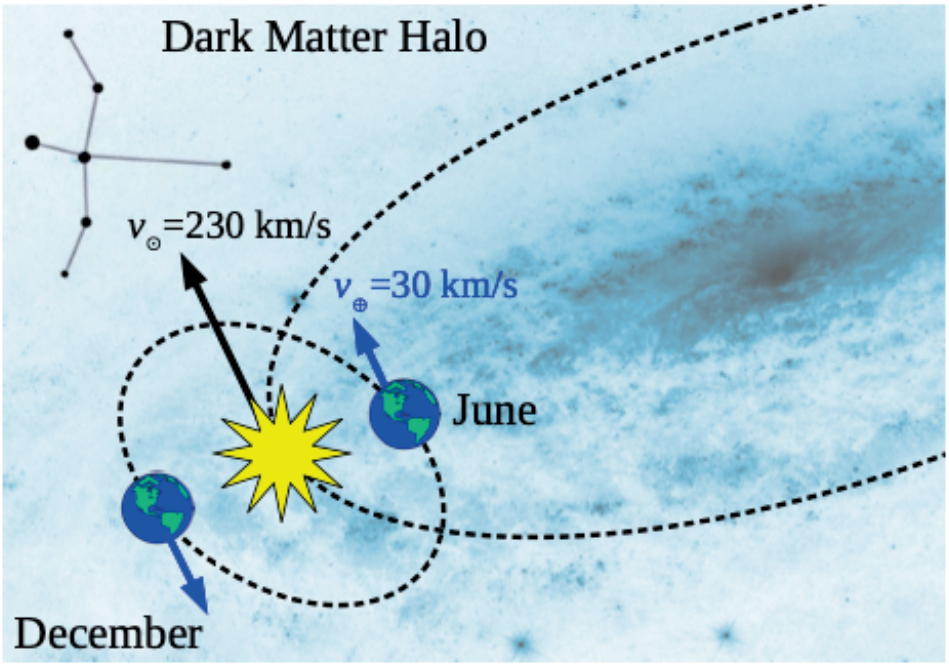

Figure 2.1 Illustration of the Sun-Earth system moving around the galactic center and through the dark matter halo in the direction of the constellation Cygnus. The varying vector addition of the velocities over a year is expected to induce a modulating dark matter signature. Taken from [73].

2.2.1 The Spin independent interaction

The SI interactions arise from the effective scalar ($\alpha_q^S \overline{\chi}\chi\overline{q}q$) and vector ($\alpha_q^V \overline{\chi}\gamma_\mu\chi\overline{q}\gamma^\mu q$) couplings of WIMPs to quarks. For SI interactions, the Helm form factor[75] is sufficient for describing the nucleus. The form factor is a Fourier transform of the nucleon density and its parameterization in terms of momentum transfer is given by[11][76]:

$$F(q)^2 = \left(\frac{3j_1(qR_1)}{qR_1}\right)\exp\left[-q^2s^2\right], \tag{2.8}$$

with j_1 the spherical Bessel function of the first kind, $q = \sqrt{2m_A E_r}$ is the momentum transfer, $R_1 = \sqrt{R^2 - 5s^2}$ with $R \approx 1.2\ A^{1/2}$ fm, and $s \approx 1$ fm is a measure of the nuclear skin thickness. The normalization is such that F(0)=1. The Helm form factor is shown in Figure 2.2 for three commonly used isotopes in DM experiments, ^{131}Xe, ^{73}Ge and ^{40}Ar.

At zero momentum transfer, the spin-independent WIMP-nucleus cross-section is given by:

$$\sigma_0 = \frac{4\mu_N^2}{\pi}[Zf^p + (A-Z)f^n]^2, \tag{2.9}$$

with $f_{p(n)}$ the effective WIMP-proton (neutron) coupling, μ_A the reduced WIMP-nucleus mass, Z the atomic number, A the mass number of the nucleus, and $f^{p(n)}$ the WIMP couplings to protons (neutrons)

In most cases, the WIMP couples in the same way to neutrons and ($f^p = f^n$), which let the SI cross-section be written as:

$$\left(\frac{d\sigma_{WN}}{dE_{\mathrm{R}}}\right)_{\mathrm{SI}} = \frac{m_N\sigma_0 F^2(E_{\mathrm{R}})}{2\mu_N^2 v^2} \tag{2.10}$$

2.2.2 The Spin-dependent interaction

The SD interactions arise from the effective axial current $(\bar{\chi}\gamma^\mu\gamma_5\chi)(\bar{q}\gamma_\mu\gamma_5 q)$, which is in supersymmetric models with a fermionic WIMP, for example[11].

The differential cross-section becomes, in this case[11]:

$$\left(\frac{\mathrm{d}\sigma}{dE_R}\right)_{\mathrm{SD}} = \frac{16m_N}{\pi v^2}\Lambda^2 G_F^2 J(J+1)\frac{S(E_{\mathrm{R}})}{S(0)}, \tag{2.11}$$

with G_F the Fermi constant and J the total angular momentum of the nucleus. Λ is defined as $\Lambda = \frac{1}{J}[a_p\langle S_p\rangle + a_n\langle S_n\rangle]$, where $\langle S_{p/n}\rangle$ is the spin expectation value of the protons/neutrons of the nucleus and $a_{p,n}$ contain the contributions of the up, down and strange quarks. The form factor is parameterized in S(q)

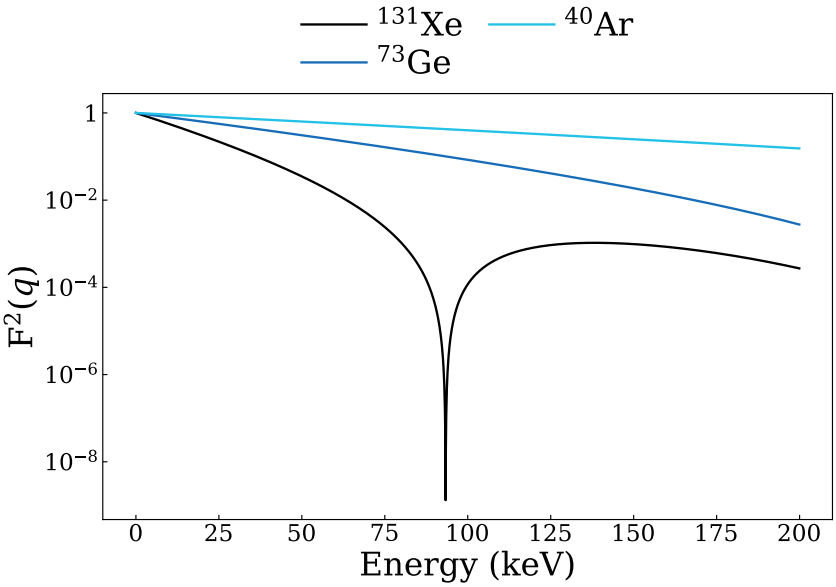

Figure 2.2 Helm form factor $F^2(q)$ as function of deposited energy (keV) for ^{131}Xe (black), ^{73}Ge(dark blue), and ^{40}Ar (light blue).

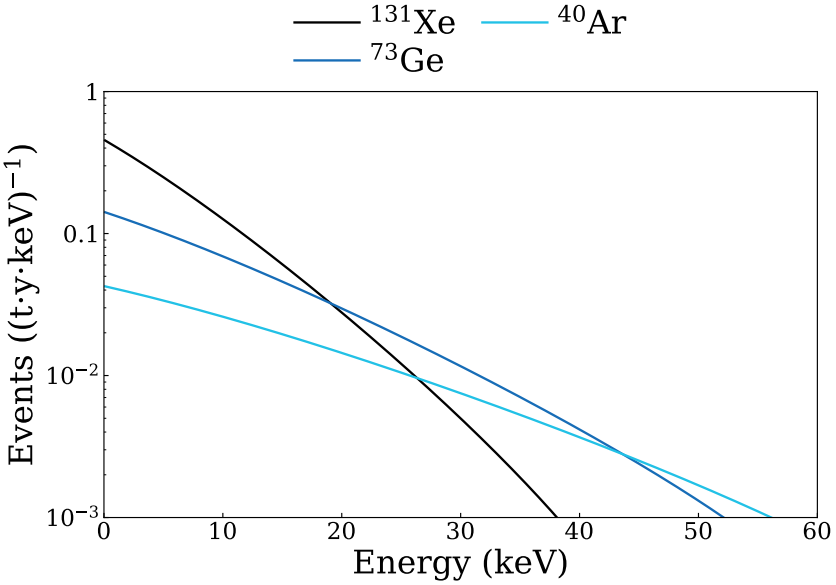

Figure 2.3 Expected event rate per tonne year per keV as a function of deposited energy (keV) for a 30 GeV WIMP with a spin-independent WIMP-nucleon cross-section $\sigma_0 = 10^{-47}$ cm^2 on ^{131}Xe (black), ^{73}Ge(dark blue), and ^{40}Ar (light blue). The cross-section's A^2 dependence leads to higher rates for heavier elements. However, the shape of the form factor causes a steep decrease in the rate at higher recoil energies.

using a decomposition into isoscalar $a_0 = a_p + a_n$, and isovector, $a_1 = a_p - a_n$ couplings[77].

$$S(q) = a_0^2 S_{00}(q) + a_0 a_1 S_{01}(q) + a_1^2 S_{11}(q), \tag{2.12}$$

where S_{ij} are experimentally determined parameters.

2.3 Low energy electronic recoils

Next to the DM models described in the previous section, various other models give measurable recoil signals on a target atom. An important distinction is that these models scatter on the electron shells of the nucleus rather than the nucleus itself. Electronic recoils allow us to investigate a different class of physics models.

2.3.1 Solar axions

As the constraints on axion mass as DM candidate are smaller than 1 keV[78], the energy deposition in liquid xenon is too small to measure. However, as axions couple to electrons, photons, and nucleons, they can be produced in places like the Sun. Three mechanisms can produce solar axions. First is from the interactions of axions and electrons, namely atomic deexcitation and recombination, bremsstrahlung, and Compton scattering[79][80]. This is referred to as the ABC process, and the flux scales with the square of the axion-electron coupling g_{ae}:

$$\Phi_a^{ABC} \propto g_{ae}^2. \tag{2.13}$$

Second, the M1 nuclear transition transition of ^{57}Fe (14.4 keV)[81]. This state can be thermally excited as the average temperature in the core of the Sun is ~ 1.3 keV and the relatively high abundance of ^{57}Fe ($(9.0 \pm 1.2) \times 10^{19}\,\mathrm{cm}^{-3}$). If axions couple to nucleons, this state can decay by emitting a 14.4 keV axion. The expected flux is given by[82]:

$$\Phi_a^{^{57}\mathrm{Fe}} = \frac{k_a}{k_\gamma} \times 4.56 \times 10^{23} g_{\mathrm{an}}^{\mathrm{eff}2} \tag{2.14}$$

with k_a (k_γ) the momentum of the emitted axion (photon).

The third mechanism is through the conversion of a photon into an axion. This is called the Primakoff process[83], and the flux is given by[84]:

$$\frac{d\Phi_a^{Prim}}{dE_a} = \left(\frac{g_{a\gamma}}{\mathrm{GeV}^{-1}}\right)^2 \left(\frac{E_a}{\mathrm{keV}}\right)^{2.481} e^{-E_a/1.205keV} \times 6 \times 10^{30}, \tag{2.15}$$

with E_a the axion energy, and $g_{a\gamma}$ the axion-photon coupling.

Axions can be absorbed through either the axio-electric or inverse Primakoff effect. The axio-electric effect has a cross-section[82][85][86]:

$$\sigma_{ae} = \sigma_{pe}\frac{g_{ae}^2}{\beta}\frac{3E_a^2}{16\pi\alpha m_e^2}(1-\frac{\beta^{2/3}}{3}), \tag{2.16}$$

with σ_{pe} the photoelectric cross section, g_{ae} the axion-electron coupling, β the axion velocity, E_a the axion energy, α the fine-structure constant, and m_e the electron mass. The axioelectric cross section is independent of axion mass for axions with $m_a \lesssim 100$ eV[87].

The inverse Primakoff effect gets contributions of elastic and inelastic scattering. The differential cross sections are given by[88][89][90]:

$$\frac{d\sigma_{el}}{d\Omega} = \frac{\alpha g_{a\gamma}^2 E_a^3 p_a \sin^2\theta}{4\pi(E_a^2+p_a^2-2E_a p_a\cos\theta)^2}(Z-F(q))^2, \tag{2.17}$$

$$\frac{d\sigma_{inel}}{d\Omega} = \frac{\alpha g_{a\gamma}^2 E_a^3 p_a \sin^2\theta}{4\pi(E_a^2+p_a^2-2E_a p_a\cos\theta)^2}S(q,Z), \tag{2.18}$$

with α the fine structure constant, E_a the axion energy, p_a the axion momentum, θ the scattering angle, Z the atomic number, q the momentum transfer, $F(q)$ the atomic form factor, and $S(q,Z)$ is the incoherent scattering function.

The total axion event rate is the of the axio-electric cross-section, and the inverse-Primakoff cross-section convolved with the axion flux. For given values of the couplings $g_{ae}=3\times10^{-13}$, $g_{an}^{eff}=10^{-6}$, and $g_{a\gamma}=2\times10^{-11}\text{GeV}^{-1}$, the axion event rate of the axio-electric cross-section is shown in the top panel of Figure 2.4, and the inverse-Primakofff cross section in the bottom panel. The ABC axion flux is taken from[80]. The values are chosen to give the same order of magnitude in the spectra and do not correspond to any particular model.

2.3.2 Neutrino magnetic moment

Observation of neutrino oscillations showed that neutrinos have non-zero mass. Extending the Standard Model to include these massive neutrinos leads to the prediction of a small magnetic moment of the neutrino given by: [91][92][93]:

$$\mu_\nu \simeq 3\times10^{-19}\frac{m_\nu}{1\text{eV}}\mu_B \sim 10^{-20}\mu_B, \tag{2.19}$$

with m_ν the neutrino mass, and μ_B the Bohr magneton.

A magnetic moment that would be significantly larger may be a manifestation of supersymmetric particles or other new physics phenomena. In addition, if the magnetic moment would be as large as $\sim 10^{-15}\ \mu_B$ this could be interpreted as an indication that the neutrino is a Majorana particle[92].

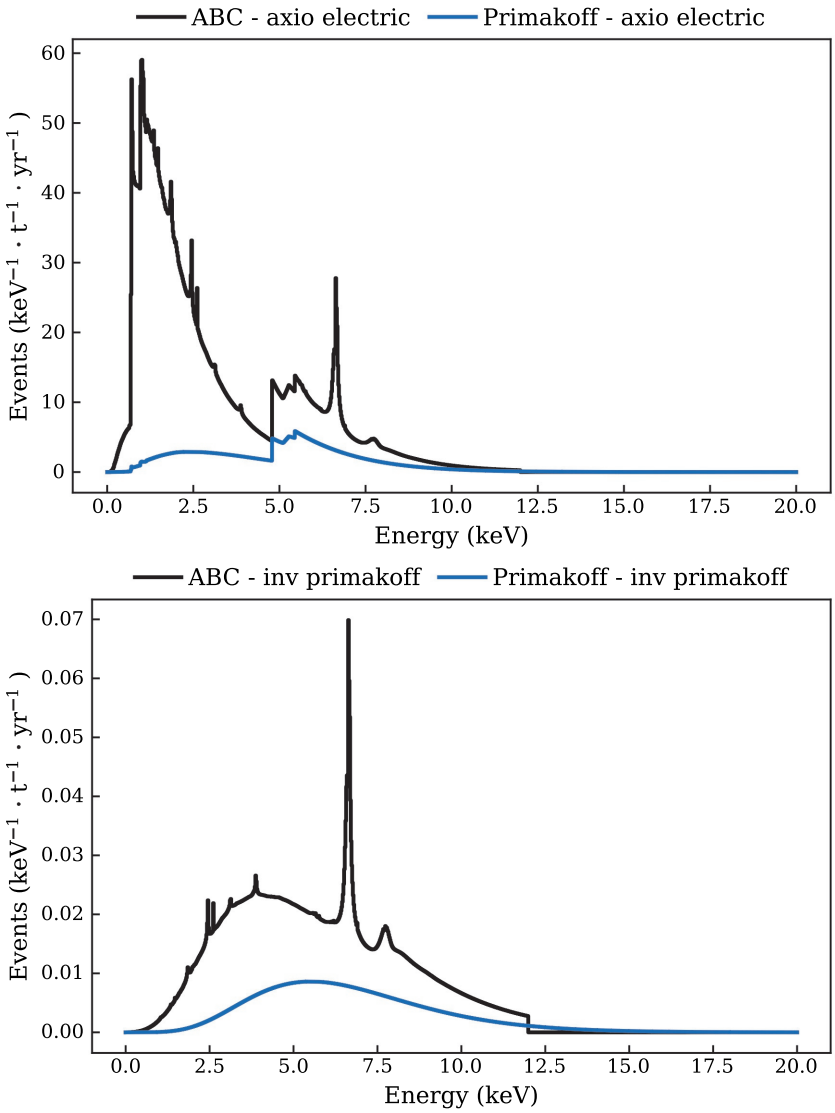

Figure 2.4 Axion event rate as a function of the energy of the three different production mechanism, ABC[80], Primakoff and ^{57}Fe with fixed values of axion couplings g_{ae}, g_{an}^{eff}, and $g_{a\gamma}$ for the axio-electric detection channel (top), and the inverse-Primakoff detection channel (bottom). The features in the ABC spectrum arise from the electron shells. The relatively high contribution of ^{57}Fe to inverse-Primakoff scattering comes from the increase of the inverse-Primakoff cross-section with energy.

The current limits are $\mu_\nu < 2.8 \times 10^{-11}\ \mu_B$ from direct detection by Borexino[94] and $\lesssim 10^{-12}\ \mu_B$ from indirect measurements on cooling of globular clusters and white dwarfs[95][96]. A large magnetic moment would increase the neutrino cross sections at low energy on electrons and nuclei, thus increasing the event rate of neutrino events. The increase in the elastic scattering differential cross section on electrons is given by[97]:

$$\frac{d\sigma_\mu}{dE_R} = \mu_\nu^2 \alpha \left(\frac{1}{E_R} - \frac{1}{E_\nu} \right), \tag{2.20}$$

with α the fine structure constant, $\mathrm{E_R}$ the electronic recoil energy, and E_ν the neutrino energy.

Figure 2.5 shows the event rate of solar neutrino's interacting with xenon with a magnetic moment of $\mu_\nu = 7 \times 10^{-11}\ \mu_B$.

2.3.3 Axion-like particles

Axion-like particles (ALPs) are similar to QCD-axions; with the omission of the strict relation between their mass and coupling strength. This allows ALPs to have higher mass than QCD-axions although they can no longer solve the strong CP problem. The expected event rate of ALPs is a mono-energetic peak at the particle mass m_a, with the rate given by[98][99][87]:

$$R \simeq \frac{1.5 \times 10^{19}}{A} g_{ae}^2 \left(\frac{m_a}{\mathrm{keV}} \right) \left(\frac{\sigma_{pe}}{b} \right) kg^{-1} d^{-1}, \tag{2.21}$$

with A the average atomic mass of the target. Figure 2.5 shows the event rate of a 20 keV ALP interacting with xenon.

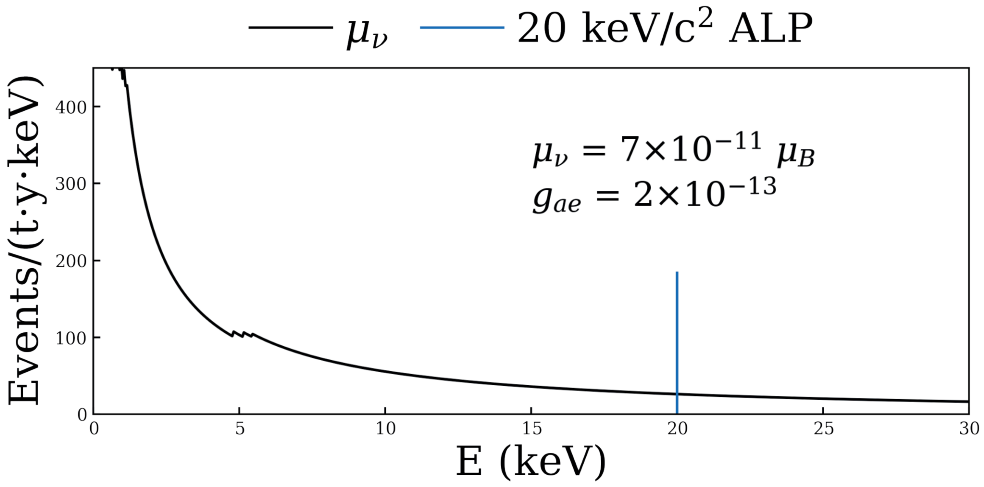

Figure 2.5 Rate as a function of energy for solar neutrinos with a neutrino magnetic moment of $\mu_\nu = 7 \times 10^{-11}\ \mu_B$ (black), and of an axion-like particle with a mass of 20 keV (blue) with xenon as target material. The step in the neutrino spectrum at 5 keV corresponds to the electron binding energy.

3

The XENONnT experiment

In this chapter, we describe the XENONnT experiment. This liquid xenon Time Projection Chamber (LXe TPC) is used to study DM particle interactions and other rare processes. We start with a general overview of how LXe TPCs work and how deposited energy is distributed over measurable light and charge. Next, we discuss the infrastructure used by XENONnT, which includes the detector design and supporting instrumentation. The Data Acquisition System (DAQ) is presented in the next chapter with a complete description of its capabilities and technical details.

Finally, we will discuss the method used to reconstruct the energy of measured interactions. This method is a crucial benchmark for the performance of the detector, and the same method is used in section 5.4 to validate the performance of the Monte Carlo framework.

3.1 Liquid xenon detectors

A dark matter detector is designed to transfer the energy deposition of a DM interaction in a measurable signal. In the case of liquid xenon detectors such as XENONnT, the signal is photons measured by photomultiplier tubes. The following section discusses the response of liquid xenon, the underlying physical processes, and the resulting light and charge yields. A quantitative model for xenon scintillation is discussed in Section 7.1.1.

Xenon has a few properties that make it an excellent choice for DM detectors:

- Xenon, as well as other noble elements, is an excellent scintillator. LXe has a yield of 45×10^3 photons/MeV for relativistic electrons [100].
- Xenon is transparent to its scintillation light (178 nm) due to the pro-

duction mechanism. This will be discussed in more detail in the next section.

- Particles cannot penetrate very far into LXe. This effect, known as *self-shielding*, is due to the high density (3.0 kg/l) and high atomic number. This causes background radiation to be unable to get to the inner volume of the detector, making background rejection based on selecting only the inner part of the detector a potent discrimination mechanism. This inner volume is called the fiducial volume, the region in the detector most free of background interactions.

- It has an ultralow electron affinity[101], making the drift of electrons through LXe very efficient. With an electric field of $\mathcal{O}$(100 V/cm), electrons reach drift velocities of $\mathcal{O}$(km/s).

- Xenon has a large number of nucleons per atom. This makes it very sensitive to the SI coupling since this scales with the number of nucleons squared (see Section 2.2.1).

- Xenon has two isotopes, ^{129}Xe and ^{131}Xe, with an unpaired neutron. The expectation values of the neutron (proton) spin are 0.29 (0.01) for ^{129}Xe and -0.272 (-0.009) for ^{131}Xe. This makes xenon sensitive to the spin-dependent interactions with both neutrons and protons.[102]

- Xenon has a large number of stable isotopes. Xenon isotopes are either unstable with half-lives in the order of a month (36.3 days for ^{127}Xe), or have half-lives that are so large they do not present a dominant background (^{124}Xe with $t_{1/2}$=1.8$\times$ 10^{21}[103] years and ^{136}Xe with $t_{1/2}$= 2$\times$ 10^{20}[104] years)

These properties lead to the development of LXe TPC)[105]. The operating principle is illustrated in Figure 3.1. The target xenon material is enclosed in a cylinder, typically made of PTFE, with two arrays of photomultiplier tubes (PMTs) monitoring the xenon. During a particle interaction within the LXe, energy is transferred to either the xenon nucleus or one of the atomic electrons, producing scintillation photons, ionization electrons, and heat at the interaction position. The scintillation photons, the S1 signal, is directly measured by the PMTs. The ionization electrons are drifted to the top of the TPC with an electric field to produce a secondary scintillation signal, the S2 signal, at the gas-liquid interface. The hit pattern of the S2 is used to reconstruct the x-y position, and the time delay between the S1 and S2 is used to calculate the z position.

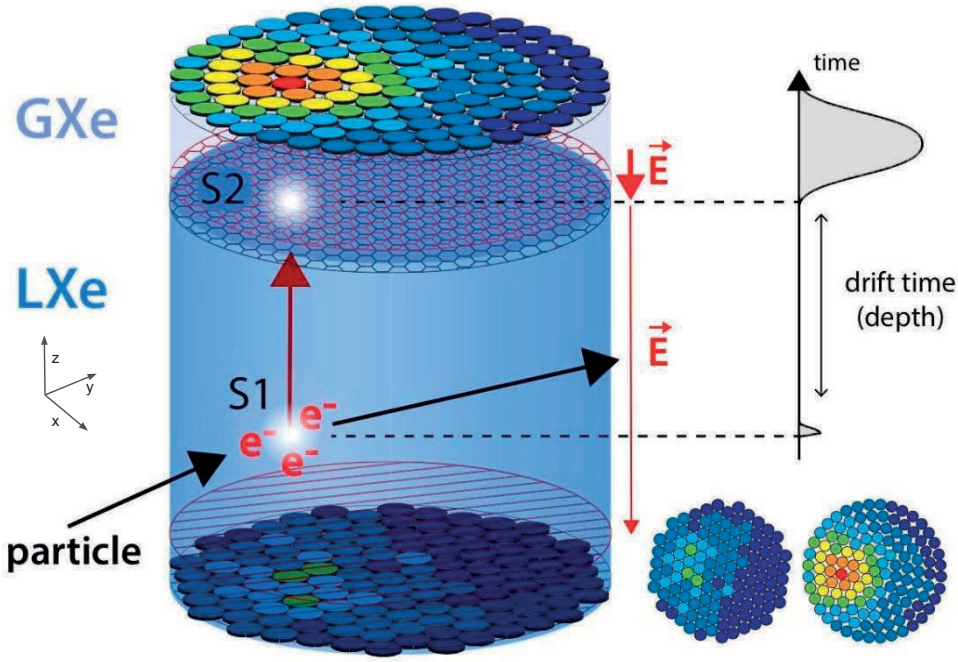

Figure 3.1 Illustration of the operating principle of an LXe TPC. An incoming particle interacts with the LXe, producing direct scintillation photons (S1) and electrons that drift to the top of the TPC, which are extracted into the GXe. The drift time corresponds to the depth, and from the hit pattern of the S2, the x-y position is reconstructed. From [106].

3.1.1 Light and Charge yield

The energy distribution over light, charge, and heat depends on the particle interacting with the LXe.

When a particle interacts with LXe, the incoming particle can either scatter on the xenon nucleus (nuclear recoil, NR) or one of the electrons of the electron shell around the nucleus (electronic recoil, ER). In this process, an ionization and excitation track is produced. Along the track, the excited xenon atoms (excitons, Xe^*) combine with neutral xenon to form excited xenon dimers (excimers, Xe_2^*). The ionized xenon atoms can form excimers via the process:

$$\begin{aligned} &Xe^+ + Xe \rightarrow Xe_2^+, \\ &Xe_2^+ + e^- \rightarrow Xe^{**} + Xe, \\ &Xe^{**} \rightarrow Xe^* + heat, \\ &Xe^* + Xe \rightarrow Xe_2^*. \end{aligned} \tag{3.1}$$

Depending on whether an electric field is applied, the ionization electrons either drift along the electric field lines or recombine and form excimers. The excimers will decay, with a lifetime of 5 ns (singlet state) or 25 ns (triplet) (at 0 external electric field), depending on the spin state of the excimer, to produce a scintillation photon via the process

$$Xe_2^* \rightarrow 2Xe + h\nu. \tag{3.2}$$

The scintillation wavelength of LXe is 178 nm (7 eV), with a width of 12 nm[107]. Unfortunately, the difference in lifetimes between the singlet and triplet states is too small to be used to identify ER or NR. This is unlike liquid argon detectors, where the difference between lifetimes is of the order of several microseconds.

The produced electron/ion pair can recombine before the electron is pulled away from the interaction site. This lowers the charge yield, and the resulting xenon atom is in an excited state in favor of the emission of a photon.

If the ionization density is high enough, such as coming from an α particle, two excimers can collide to produce one electron-ion pair through a process named "bi-excitonic" quenching[108]:

$$Xe^* + Xe^* \rightarrow Xe_2^{**} \rightarrow Xe + Xe^+ + e^- \tag{3.3}$$

This process results in a reduction of the scintillation yield in high-energy-density collisions.

The way the energy deposition is distributed over light and charge is dependent on the electric field in a complicated manner. The NEST collaboration

provides global fits to light and charge yield measurements of various noble element experiments[109]. The light (charge) yield of ER and NR interactions for two field configurations (22 V/cm, the XENONnT operating, and 200 V/cm, the XENONnT design voltage) is shown in Figure 3.2 (Figure 3.3). Qualitatively, the external electric field results in a higher charge yield as electrons are pulled away from the interaction site before recombination can occur. The lower yields of NR interactions are due to the energy lost to heat. An up-to-date description of the NEST model is out of scope for this work and can be found in [110]. A simplified model to describe xenon scintillation yields is described in the Section 7.1.1.

3.2 The XENONnT experiment

This section will focus on a general overview of XENONnT[111] [112][113], a dual-phase xenon Time Projection Chamber (TPC). At the same time, the XENONnT DAQ is discussed in the next chapter.

XENONnT is the latest and largest experiment of the XENON collaboration, located at *Laboratori Nazionale del Gran Sasso* (LNGS) in Italy. The experiment is shielded from cosmic rays by an overburden of 1500m of rock, equivalent to 3600m of water. The infrastructure used for XENON1T is mostly reused, including the water tank, TPC support structure, and neutron and muon veto sub-detectors. The TPC hangs inside the water tank, surrounded by neutron and muon veto sub-detectors. The service building holds the purification and distillation systems, the electronics and data acquisition, and the storage and further distillation systems. The central piece of the experiment is the TPC, as described before. This is a cryogenic stainless steel vessel filled with liquid and gas xenon. All materials used in the detector have been selected after an extensive radioactive screening campaign.

For every particle interaction, 494 Photo Multiplier Tubes (PMTs), divided into a top and bottom array, record the photons from the primary (S1) and the secondary (S2) scintillation signals.

3.2.1 Time Projection Chamber

The TPC is the core component of the XENONnT experiment, and all components in or near the TPC are made from materials with extremely low radioactivity levels. The TPC is made of interlocking panels of polytetrafluorethylene (PTFE or Teflon), which form a cylinder with a diameter of 1340 mm and a length of 1500 mm at room temperature. During operation, the TPC will enclose an active liquid xenon mass of 5.9 tonnes, with the PTFE contracting by 1.5% to a length of 1479 mm. The thickness of the PTFE panels ranges

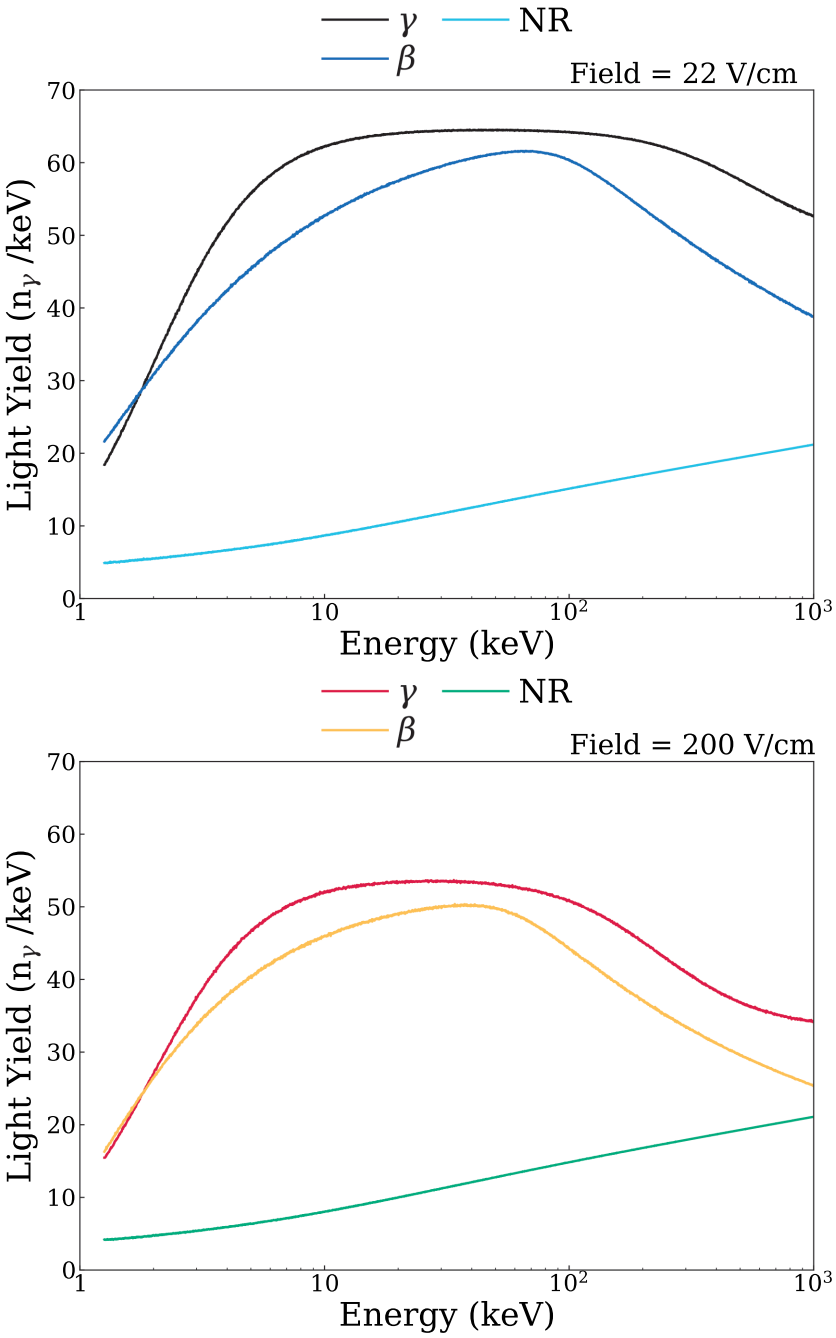

Figure 3.2 Light yield of γ, β and nuclear recoil interactions in LXe with an external electric field of 22 V/cm (top), and 200 V/cm (bottom) as a function of energy (keV), according to NEST v2.3

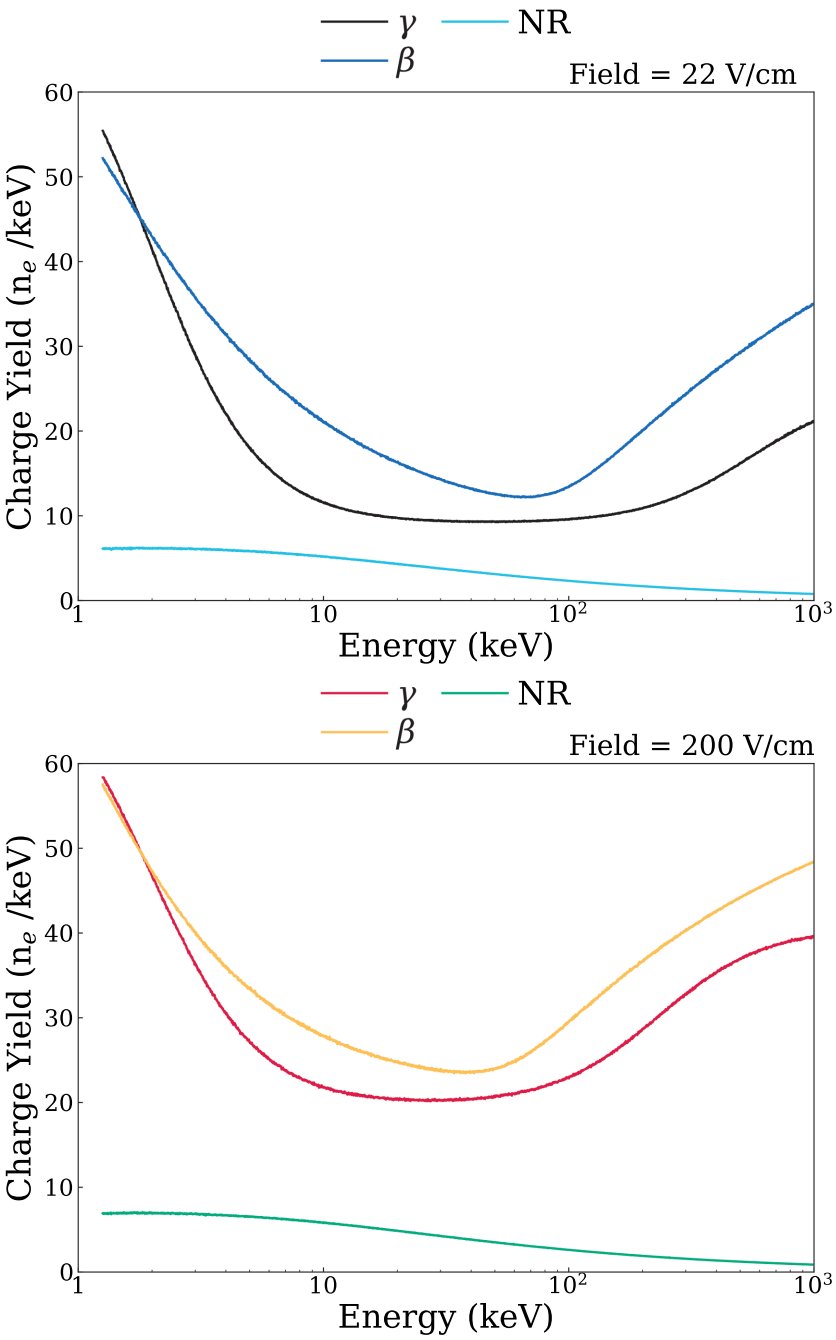

Figure 3.3 Charge yield of γ, β and nuclear recoil interactions in LXe with an external electric field of 22 V/cm (top), and 200 V/cm (bottom) as a function of energy (keV), according to NEST v2.3

from 2 mm to 5 mm, depending on their position, to minimize the impact of the high (α,n) cross-section of ^{19}F in the PTFE, which can contribute to the neutron background.

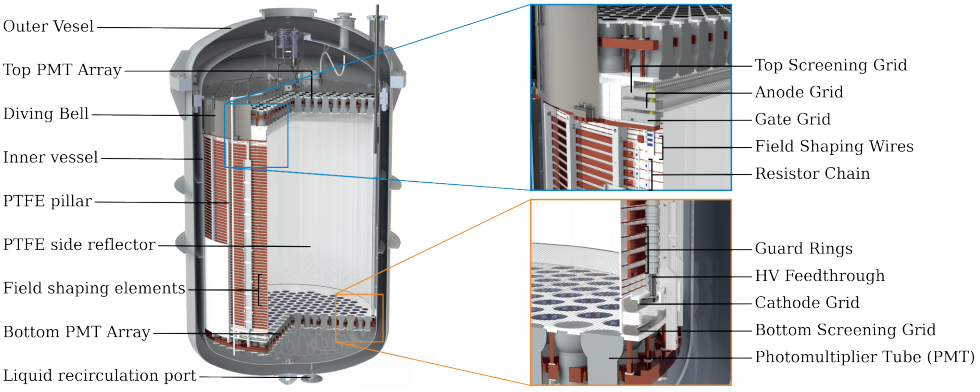

Figure 3.4 CAD drawing of the XENONnT TPC. On the left side is the full TPC, and on the right side are zoomed-in figures of the top and bottom electrodes. The components are labeled, including the outer vessel, top PMT array, diving bell, inner vessel, PTFE pillar, side reflector, field-shaping elements, bottom PMT array, and liquid recirculation port. The TPC is filled with LXe between the Anode and gate grids.

At the top and the bottom of the TPC, two arrays are mounted holding 253 and 241 3-inch diameter Hamamatsu R11410-21 Photo Multiplier Tubes (PMTs) observing the liquid xenon target. In both arrays, the PMTs are arranged in a hexagonally close-packed structure; in this formation, the position reconstruction is more robust against non-functional PMTs. They have an average quantum efficiency of 34.5 percent at the xenon scintillation light wavelength (178 nm). Each PMT has a base that divides the high voltage over the different dynode stages and connects the signal and ground to the readout electronics.

Two sets of electrodes at the top and bottom of the TPC contain the drift volume. At the top are the top screening mesh, the anode, and the gate, and at the bottom are the cathode and the bottom screening mesh. Massive copper field shaping rings are linked in series along the drift volume. The electric field over the TPC is designed to be 200 V/cm, requiring a bias voltage of -30 kV on the cathode with the gate at the ground. The gate is connected to the top field-shaping ring by two 5GΩ resistors per link, while the cathode grid and the bottom-most field-shaping ring are linked via two 25 GΩ resistors. The values of the resistors and grid shapes are optimized using electric field simulations (COMSOL) to define an electric potential. The gradient is constant over the

drift volume, resulting in a homogeneous drift field. Electrons that drift toward the gas phase are extracted by a 2.9 kV/cm extraction field generated between the gate and the anode electrodes to generate the S2 signal. Two screening meshes are installed between the electrodes and the PMTs to shield the PMTs from the high electric fields. These two meshes are biased at the average bias voltage of the PMTs (-1500 V) to minimize the strength of the electric field in those regions of the detector.

All five electrodes are grids made from parallel wires. The field must be homogeneous in the extraction region to minimize position-dependent S2 corrections. To accomplish this, very stringent requirements are on the flatness of the anode. Two perpendicular wires have been added to the frame to avoid the sagging of the anode wires.

The TPC is submerged in the LXe during operation. Since the proportional scintillation has to be done in the gas phase, the liquid level is stabilized between the gate and anode electrodes. The stabilization is done via a diving bell construction where pressurized xenon is flushed into the gas phase through an exhaust tube. The xenon gas pressure can be used for tuning the liquid level. It is monitored using six capacitive level meters, two long level meters to monitor the liquid level during the filling of the TPC, and four short level meters used for precise measurements of the liquid level during regular operation.

The cryostat has to be thermally insulated to maintain the cryogenic temperatures inside the TPC. The cryostat used in XENONnT has an inner vessel of 1.46 m diameter and 1.87 m height inside the 1.62 m diameter and 2.49 m height outer vessel. The volume between the inner and outer vessel is continuously pumped to maintain an insulation vacuum. The inner and outer vessels of the cryostat feature a vacuum-insulated liquid xenon feedthrough that will serve as a liquid connection to the liquid xenon cryogenic purification system located on the ground floor next to the service building.

A cryogenic pipe connects the detector to the supporting cryogenic infrastructure and the data-acquisition system, which passes through the water tank. It allows for xenon in and outflow and leads sensor cables to feedthroughs that connect them to the outside.

3.2.2 Cryogenics, purification, distillation, and calibration

The cryogenics system uses two pulse-tube-refrigerators (PTRs) and an additional liquid nitrogen (LN_2)-based cold head to cool the xenon gas. During operation, one of the PTRs runs with the other as backup. The LN_2 is used for cooling the xenon in case of a loss of power. Continuous gas purification is achieved through a hot zirconium getter, while liquid purification is done in parallel. A method of quantifying the purity is through the *electron lifetime*.

This represents the timescale of electrons being captured by impurities in the LXe. Using liquid purification, the electron lifetime of XENONnT reaches up to 20 ms. This is exceptionally high compared to other experiments, i.e., the electron lifetime of XENON1T was between 380 - 650 μs[114], and LZ reports an electron lifetime of between 5 - 8 ms[115].

Before the start of the experiment, all xenon used in the detector is passed through a distillation column to remove contamination of ^{85}Kr. This makes the background due to ^{222}Rn and its daughters the dominant background in XENONnT. We will discuss these backgrounds in more detail in Chapter 6.

To measure the performance and calibrate the detector's response to expected signals, radioactive sources emitting α, β, γ, or neutron radiation are used. ^{220}Rn is dissolved into the LXe for electronic recoil calibration, while ^{212}Pb is used for low-energy ER calibration. Blue LED light transferred through fibers calibrates the PMTs, while ^{231}AmBe outside the cryostat or a neutron generator is used for nuclear recoil calibration. The metastable ^{83m}Kr calibration source, generated from ^{83}Rb, maps out the entire TPC with high statistics for electron lifetime and energy scale calibration of low-energy electronic recoils.

For the calibration of nuclear recoils, neutron calibrations are done at the beginning and end of a science run and take up to a week or two. After a neutron calibration, gamma lines resulting from neutron-activated isotopes calibrate the energy response. Monthly ^{220}Rn and bi-weekly krypton calibrations monitor for any time-dependent effects in the TPC, taking several days or a day or two, respectively. Weekly LED calibrations monitor any gain changes.

3.2.3 Veto systems

The entire structure sits inside a cylindrical water tank of 9.6 meters in diameter and 10m in height. The water tank is a passive shield against gamma rays and an active Cherenkov muon veto. The water tank is covered in reflective foil and instrumented with 84 PMTs of 20.3 cm in diameter (Hamamatsu R5912ASSY) with a bialkali photocathode on a borosilicate window with a quantum efficiency of about 30% of visible light wavelengths. The muon veto detector records the signals of a crossing muon, allowing the timestamps to be used to reject interactions contained within the time region by muon-induced neutrons with an efficiency of 99 percent[116].

The expected neutron background in XENONnT is 0.27 per tonne year exposure. This results in 5.5 neutron events for the 20 t $\times$ yr exposure required to achieve the projected XENONnT sensitivity[117]. A Neutron Veto (NV) system surrounds the outer cryostat to identify and mitigate the neutron background. The NV consists of reflective panels holding 120 8" Hamamatsu

R5912ASSY PMTs. During the first science run (SR0), the NV was operated with pure water. This resulted in a neutron tagging efficiency of ~ 0.65. The water inside the NV will be doped with ^{157}Gd and ^{155}Gd at a later stage of operation. Gadolinium, ^{157}Gd and ^{155}Gd, in particular, has the highest neutron capture cross-section of all stable elements[118]. Upon capturing a neutron, gadolinium emits a cascade of gamma rays with a total energy of $\sim$ 8 MeV. The gamma rays undergo Compton scattering in the water, exciting electrons above the Cherenkov emission threshold, the measured signal. This will increase the NV tagging efficiency to ~ 0.87. This will drop the neutron background of XENONnT to 0.041 events/ton/year.

3.3 Energy reconstruction

In XENONnT, the light and charge signals produced by interactions are combined to reconstruct the energy. The observed S1 (S2) signals are related to the produced number of photons (electrons) by the mean number of detected photons g_1 (electrons, g_2). The values of g_1 and g_2 are detector-specific and are calibrated using mono-energetic electronic recoil calibration data. Determining the parameters g_1 and g_2 is crucial for accurate energy reconstruction and subsequent data analysis in XENONnT. The observed S1 and S2 signals are related to the energy deposition by the simplified Palzman equation[119]:

$$E = W(n_\gamma + n_e) = W\left(\frac{\mathrm{cS1}}{g_1} + \frac{\mathrm{cS2}}{g_2}\right), \tag{3.4}$$

with W the work function, the required amount of energy to produce one photon or electron, $\mathrm{n}_\gamma(\mathrm{n}_e)$ the number of produced photons (electrons), cS1 (cS2) the corrected S1 (S2) signal in photoelectrons (pe), and g_1 (g_2) the number of measured photoelectrons per photon (electron). W is a fixed parameter with a value of 13.7 eV[109]. The S1 and S2 need to be corrected for the spatial variations in the TPC. The light yield is affected by spatial variation of the Light Collection Efficiency and the quantum efficiencies of the PMTs. Impurities reduce the charge yield in the LXe for interactions lower in the TPC, and sagging of the anode mesh changes the extraction efficiency. Inhomogeneity of the drift field changes the drift trajectory of electrons, resulting in a change in the reconstructed position. This affects all position-dependent corrections.

Figure 3.5 shows the Doke plot, illustrating the relationship between the light yield and charge yield of energy depositions from different sources, such as ^{83m}Kr, ^{136m}Xe, ^{134m}Xe, and ^{36}Ar. The data points are fitted to the function Q_{ee} to extract the values of g_1 (0.151 pe/ph) and g_2 (16.49 pe/e). These values are used extensively in subsequent analyses for energy reconstruction.

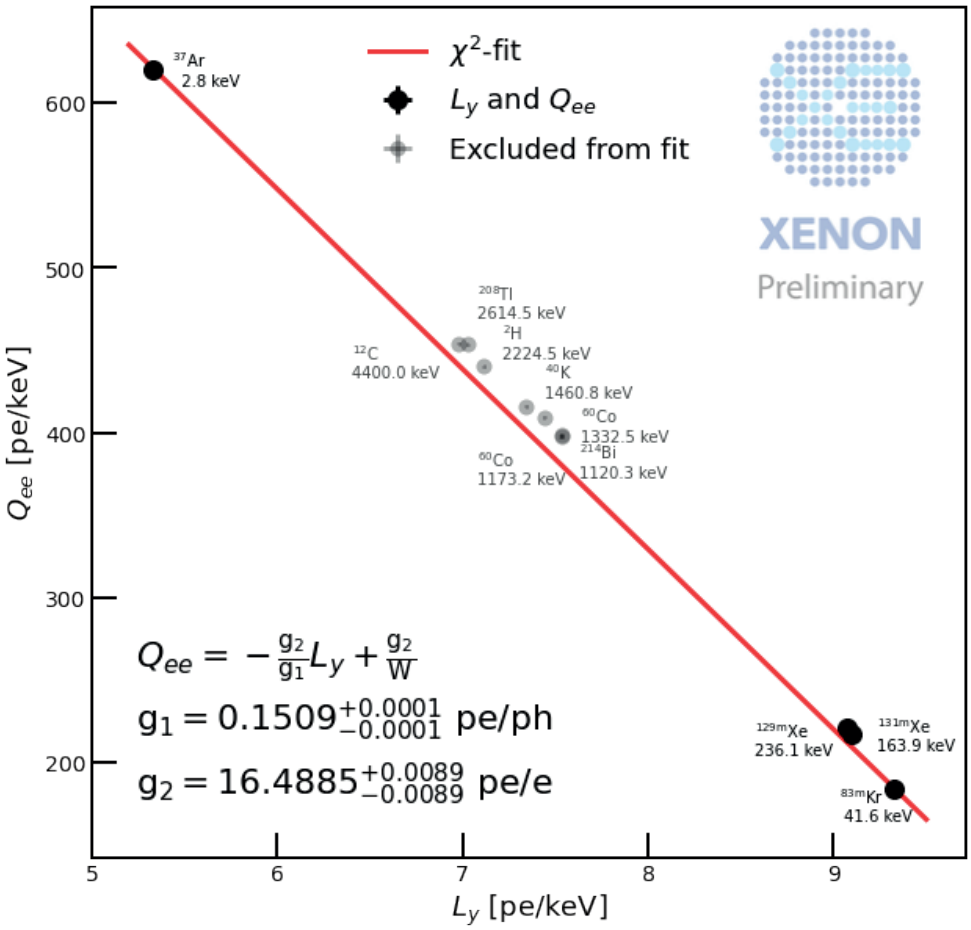

Figure 3.5 The Doke plot showing the relation between the light yield (x-axis) and charge yield (y-axis) of energy depositions from ^{83m}Kr, ^{136m}Xe, ^{134m}Xe, and ^{36}Ar. Grayed out points are from ^{208}Tl ^{60}C, ^{12}C, ^{2}H, ^{40}K, and ^{214}Bi The error bars show the statistical uncertainty of the data points. The function Q_{ee} is a least-square fit to the data to extract the values of g_1 (0.151 pe/ph) and g_2(16.48 pe/e). The values of g_1 and g_2 are crucial parameters for energy reconstruction and further analysis of the data of XENONnT.

4

The XENONnT Data Acquisition System

The XENONnT data acquisition system (DAQ) comprises all electronics responsible for amplifying, reading, and processing each Photomultiplier Tube (PMT) signal. The DAQ extended the existing XENON1T DAQ[120] and was designed as a triggerless system; data is acquired constantly without a global trigger but on a per-channel basis with a threshold as low as possible. All data is stored on disk, and physical interactions are identified later in software. This requires custom readout logic to allow for independent readout of all detector channels while keeping full time-synchronization. Data is read from the digitizers and written to a storage buffer. Usually, within minutes after the acquisition, the data is fully processed as required for data analysis. The files are then transferred to external sites for storage, where they become available for analysts. The DAQ is located in the XENONnT service building next to the water tank on the second floor. This chapter gives an overview of the DAQ. The focus is on the DAQ for the TPC, although similar schemes have been implemented for the muon and neutron veto systems.

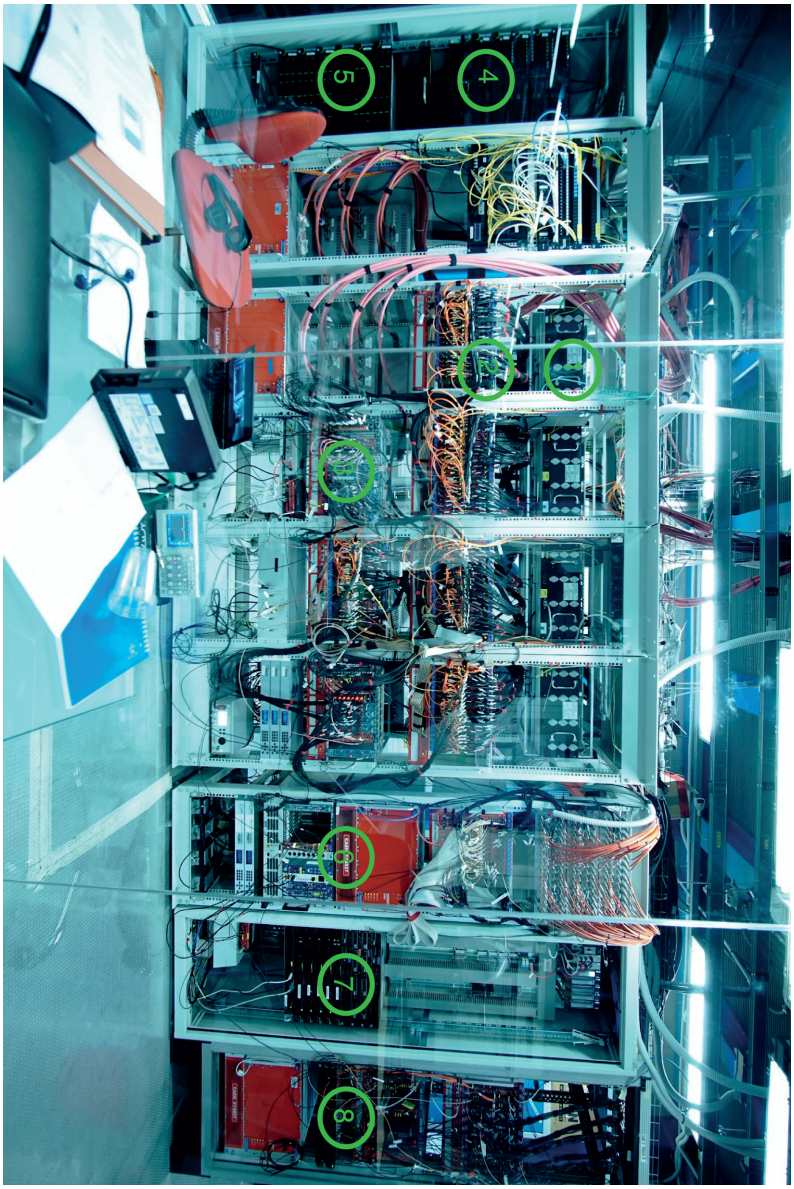

Figure 4.1 Front view of XENONnT's Data Acquisition System (DAQ) on the second floor of the service building in Hall B of Laboratori Nazionali del Gran Sasso (LNGS). Numbers indicate the main components: 1: Amplifiers, 2: Digitizers, 3: Logic Modules, 4: Readout servers, 5: Processing servers, 6: Muon Veto DAQ, 7: Slow Control, 8: Neutron Veto DAQ.

4.1 Overview

Figure 4.1 shows a frontal view of the DAQ system, and a schematic diagram is presented in Figure 4.2. Three separate systems register the data from the TPC, Muon Veto (MV), and Neutron Veto (NV) PMTs. The systems can either run entirely independently of each other or run in "linked mode" as a single system. The DAQ automatically stops and restarts every 30 minutes or 1 hour, depending on detector conditions. These intervals, called *runs*, organize the data in continuous periods with a non-changing configuration.

This section is organized as follows: first, we introduce the design requirements for this system. Then, we follow the layout of Figure 4.2 from left to right, explaining all components in detail.

4.1.1 Design requirements

The XENONnT DAQ is designed to fulfill the following criteria:

Low energy threshold XENON1T used a triggerless readout to write to a buffer database to have an energy threshold that was as low as possible. A software trigger identified events to store from the buffer. Data outside of the events were deleted. Although this method was successful in achieving a low energy threshold, it made the identification of some backgrounds more complicated, such as for S2-only[121] and the Single electron analysis[122]. The DAQ can, therefore save all data to disk. All relevant events are identified later during processing. This does not lead to a significant increase in data storage requirements. The main driver for data volume is high-energy gamma rays, with a rate of $\sim$ 1 Hz. A 2 MeV gamma-ray produces a $\sim$ 3.5 MB S2 signal; this number increases when the gamma-ray undergoes Compton scattering before being absorbed, as this widens the temporal spread of the S2. These high-energy events are used for detector calibration and high-energy analysis.

Low noise The noise level of the DAQ has to be minimal to have a low energy threshold. High-frequency noise can mimic a small single photoelectron signal. Besides affecting the energy threshold, high noise levels cause jitter in the digitizer time synchronization cables. This causes a PLL (phase-locked loop) unlock, interrupting data acquisition.

Low deadtime The dead time during a run, flagged as bad by the busy, must be minimal. If a DM interaction occurs during dead time, the signal is lost. As DM interactions are expected to occur $\mathcal{O}$ (1 yr^{-1}) and the background

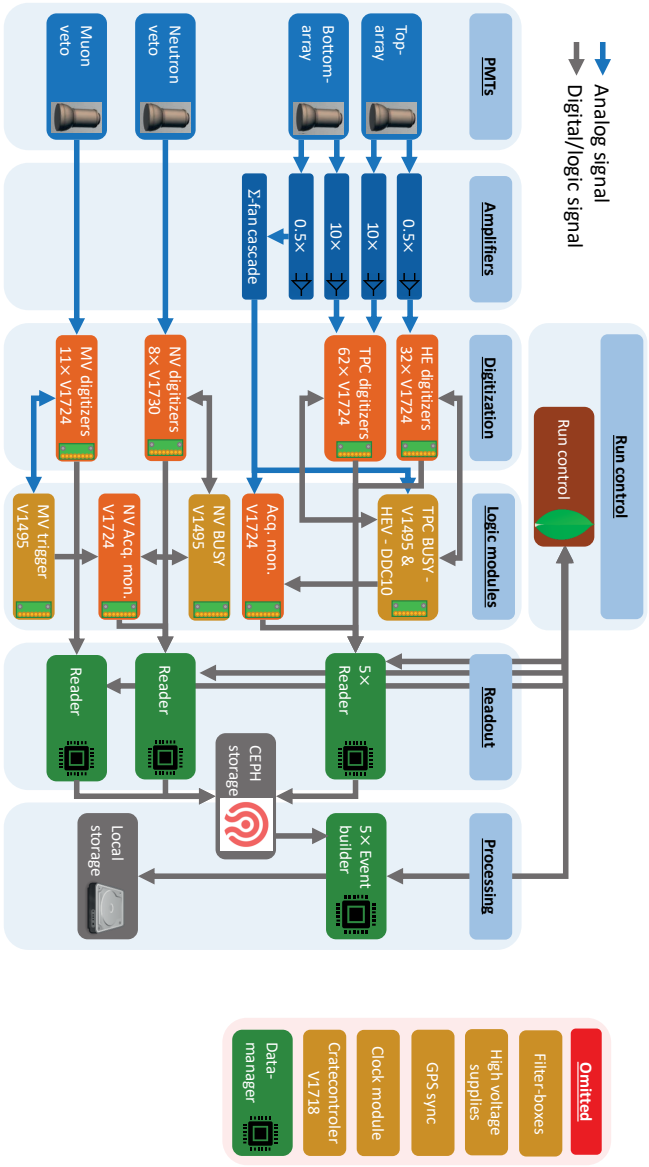

Figure 4.2 Schematic overview of the XENONnT DAQ, showing the most important components from the start at the PMTs (left) until the final local storage (right). The arrows show the analog (blue) or digital (gray) data. The TPC, MV, and NV have separate DAQs, which can be run as a single system.

increases linearly with time, the loss of data cannot be offset by measuring longer as the background expectation has increased too much.

High data rates We use radioactive sources in and around the detector to calibrate the signal response. As this time is unsuitable for dark matter searches, the time spent on calibration should be as little as possible while still acquiring the required statistics. Therefore, the DAQ is designed to read out high rates of $\mathcal{O}$ (500 MB/s). The limiting factors in the data rate are the source strength and the rate at which pileup events start occurring. Due to the detector conditions on SR0, pileup started at rates $\sim$ 150 MB/s.

Dual gain readout The XENONnT experiment is optimized for measuring small, low-energy signals for DM interactions. The PMT signals require amplification before the digitization to ensure the pulses are large compared to the sample size of the digitizers.

One of the other science channels is the search of the neutrinoless double beta decay of ^{136}Xe, with a Q-value=2.48 MeV[123]. Such highly energetic decay can cause large enough signals in a single PMT that the pulse voltage is larger than the range of the digitizer (2 V). This will cause the digitizer to saturate, the pulse amplitude to cut off at the maximum voltage of the digitizer, and the information on the original pulse amplitude to be lost.

To avoid digitizer saturation and thus improve the energy and position reconstruction accuracy of large signals, the amplifiers have an amplified (10x) and an attenuated (0.5x) output. Both signals of PMTs in the top array are digitized; the bottom array PMTs have the amplified output digitized, and the attenuated signal is summed and digitized separately and used as input for the high-energy veto.

Fast data processing The data should be available as fast as possible after being acquired. After the acquisition, the DAQ fully reconstructs data within $\mathcal{O}$(10 s). This allows accurate monitoring of detector conditions in almost real-time

High-energy veto Due to the SR0 detector conditions, the data rates are increased by a factor of $\sim$ three during science data taking. On top of that, the limited calibration rates required significantly longer calibration times. To minimize the burden on the computing system, the High-energy veto (HEV) was designed to veto high-energy data during calibration aimed at calibrating the low-energy response of the detector.

4.1.2 Hardware

This section describes all the hardware components of the DAQ, from the PMTs to the final storage of the data.

PMTs The TPC DAQ reads signals from the TPC's 494 Hamamatsu R11410-21 3-inch PMTs[124]. The PMTs are distributed over the amplifiers, digitizers, VME crates, and readout servers to distribute the data load equally. This is illustrated in Figure4.3, which shows how the PMTs of the top and bottom array are distributed over the high-voltage connectors and digitizers. The PMTs detect incident photons on the photocathode with an average quantum efficiency of 35% and are amplified by a channel-dependent gain of (1.0-5.0) $\times$ 10^6[125]. The signals are routed by 12 m PTFE-coated RG 196 coaxial cables from the PMT arrays through the umbilical pipe connected to the top of the cryostat to the top floor of the service building. The cables come into the DAQ room on the floor below, connected to custom-made amplifiers.

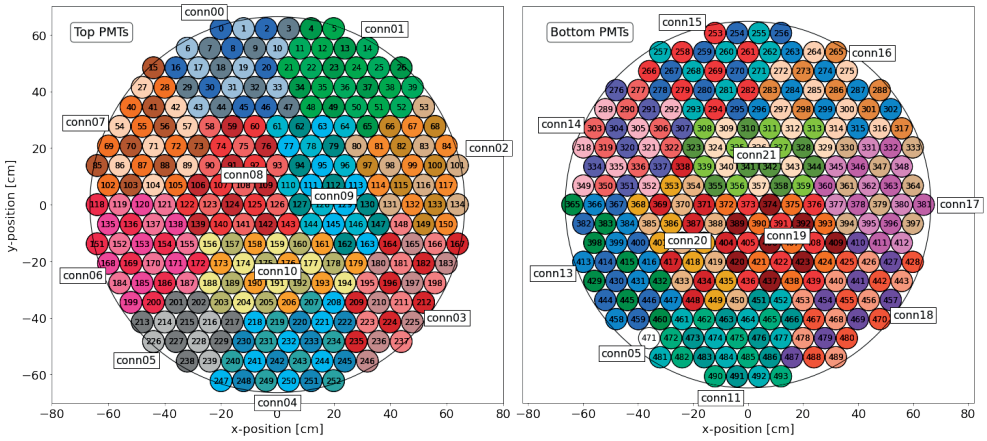

Figure 4.3 Top (left) and bottom (right) array PMT cable map. The colors indicate different high-voltage connectors and the color shades indicate which digitizer the PMT is connected to within the connector.

Amplifiers The PMT signal cables are connected to custom-made amplifiers made by the University of Zurich with two separate outputs. One output provides a factor 10 gain, the other 0.5. The 10x and the 0.5x amplified top array outputs are connected to the input channels of CAEN V1724 digitizer modules to record signals from each PMT. The 0.5x signals from the bottom array go to a reverse fan cascade, to sum up all channels. This is digitized

by a separate V1724, the Acquisition Monitor (AM), and is used to input a DDC-10 for the HEV after attenuation to fit inside the dynamic voltage range.

Digitizers The digitizers used for the TPC are CAEN V1724 digitizers[126][127]. This module reads eight channels with 14-bit 100 MS/s sampling and has a 2.25 V input range, 40 MHz bandwidth, and 8 MB dual-ported onboard memory. The TPC DAQ has 94 of these modules that record the data from the TPC, and the acquisition monitor is used to monitor the state of the DAQ. 62 of the V1724 are used to digitize the outputs of the 10x amplifiers. The 32 other V1724 are used to digitize the attenuated outputs of the top array PMTs. The digitizers are housed in five CAEN VME crates connected to the dedicated DAQ ethernet network to allow experts to control all the crates remotely. The power consumption and temperatures of the crates are written to the DAQ database (see 4.2.1) for diagnostics every second.

The digitizers sample at ten and run custom firmware, the Digital Pulse Processing with Dynamic Acquisition Window (DPP-DAW), developed initially together with CAEN for XENON1T[120] to allow channels to trigger independently of each other. The self-triggering mechanism is illustrated in Figure 4.4. The digitizer continuously compares the signal per channel to the baseline. If the signal exceeds the threshold (THR), the acquisition starts with a minimal event window (MRL). If the pulse lasts longer than the minimal event window, it is automatically extended (EXT) until it returns below the threshold. The digitizers write all data above the threshold, with a pre-and post-trigger time window to memory. The pre-and post-trigger windows (PRE-TRG, samples under threshold SUT) are set to 50 samples (500 ns) to allow enough data to calculate the pulse baseline. The digitizer's internal memory determines the maximum trigger window, which is over 2 ms. This maximum is much larger than typical signals occurring during stable readout conditions. The trigger threshold defaults to 15 ADC counts, corresponding to 2.06 mV ($\sim$ 0.1 pe). The trigger threshold is raised if a channel shows high trigger rates due to electronic noise or strange PMT behavior. The digitizers are programmed to delay their readout by 10 μs to accommodate the high energy veto. The data read from the digitizers are the Event Time Tag (ETT), channel number, and pulse amplitude in ADC counts. As the digitizers share their clock, the ETT determines what pulses occurred simultaneously. The start of the acquisition is synchronized by a NIM logic signal from a CAEN V2718 crate controller to ensure all digitizers start simultaneously.

Acquisition monitor The Acquisition Monitor (AM) is a specific V1724 used to track general information on the TPCs and veto systems. One of the

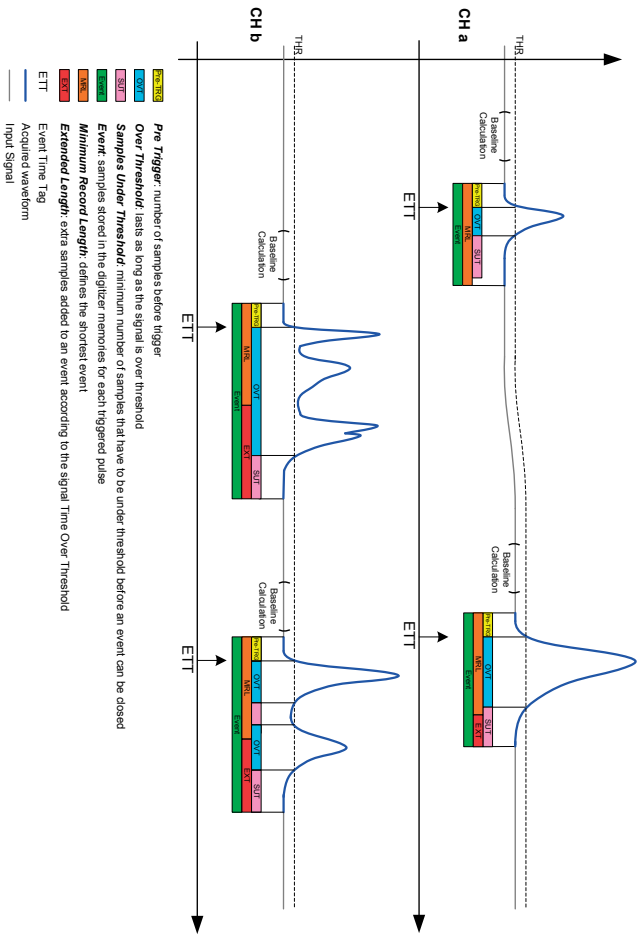

Figure 4.4 Illustration of the trigger conditions used by the DPP-DAW firmware on the V1724 digitizers for two conditions. The top shows a single pulse; the bottom shows multiple pulses. The moving average of the baseline is continuously compared to the threshold for every channel individually. When the pulse goes over the threshold, it is written to memory as long as it is over the threshold, with a set pre- and post-trigger window of 50 samples. The minimum pulse length is 100, while the maximum is 2^{17} ($\sim$1.3 $\times$ 10^5 samples, 1.3 μs). The Event Time Tag (ETT) is the timestamp given to the event during acquisition. This timestamp determines which pulses come from the same signal of the LXe. The Pre-Trigger (PRE-TRG), Samples Under Threshold (SUT), and Minimum Record Length (MRL) are set configuration values (50, 50, 100 samples). The event (EVT) and Extended Length (EXT) depend on the time over the pulse threshold and vary per event. From [128].

inputs is the attenuated bottom array sum signal, which is used to monitor the TPC when the DAQ goes busy and for the commissioning of the HEV. The AM also receives a periodic signal from the GPS module to track the synchronization of the DAQ. Furthermore, the AM receives the start and end signals of the busy and HEV systems.

Busy During operation, the onboard memory of the digitizers will fill up until it is read out by one of the reader servers. At that point, the memory will be available for writing again. However, if the digitizers are not read out in time, and the memory is filled up completely, the digitizers will not be able to store new pulses. When this happens, the digitizer will raise a busy signal from the front panel connected to a CAEN V1495 module. This module has firmware configured to raise a NIM logic signal if any digitizers raise a busy condition. The NIM signal is propagated to all digitizers to stop acquisition and to the acquisition monitor until the memory of the busy digitizer is read out and cleared. The NIM signal is lowered at that point, and the acquisition continues. This is illustrated in Figure 4.5, which shows the summed raw waveform of the PMTs, with the start of the busy indicated in blue. The red line marks the determined veto interval. As soon as the busy starts, data taking is stopped for the duration of the busy. The veto region is 0.25 ms before and after the busy is raised. Events and peaks overlapping with a veto region in time are removed from the analysis.

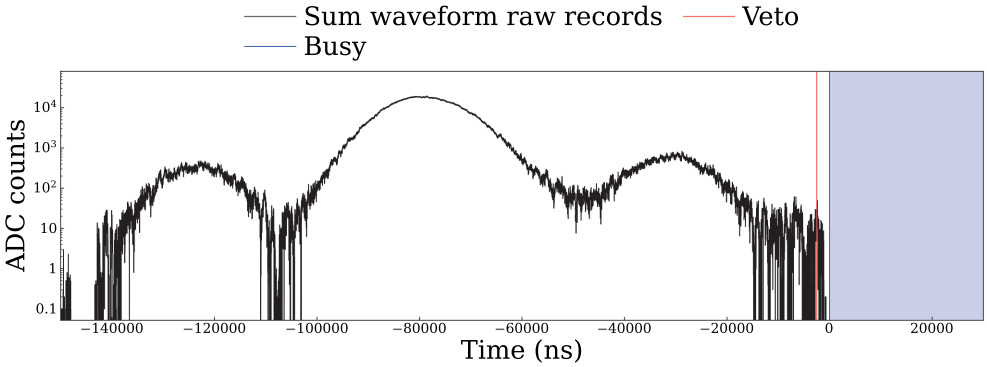

Figure 4.5 Raw waveform of a large S2 with busy from XENONnT. The black line is the summed waveform as recorded by the digitizers. The blue vertical line indicates the start of the busy signal, after which the acquisition is halted. The red line indicates the veto interval, which ignores data close to the busy. Events and peaks overlapping with a veto region in time are removed from the analysis. On the x-axis, 0 indicates the start of the busy signal.

The timestamps from the signals recorded by the acquisition monitor are

later used to cut out any leftover events near the time window around the busy condition, as data is missing from this period, and for calculating the correction to the livetime of the run. If the DAQ is operated using a hardware trigger signal, such as during LED calibration and noise measurements, the acquisition is not stopped during a busy. Events occurring during the busy are later removed during analysis.

In the case of the TPC, the V1495 can also generate periodic veto signals to halt data taking when the detector runs at an extremely high rate. This mode was used to take ^{83m}Kr calibration data when the water tank was still empty. This resulted in high data rates ($\mathcal{O}$ (1 GB/s)) from high-energy gamma rays from detector materials that the water would have shielded in regular operation.

High-energy veto When taking calibration data, especially with the YBe, AmBe, and ^{220}Rn calibration sources, a significant part of the acquired data comes from high-energy gamma-ray and alpha decays rather than the low-energy neutron, gamma-ray, and beta decays of interest. The high energy events are followed by a long tail of delayed single electrons, causing high readout rates. This takes up large amounts of disk space, while the data is useless for most analyses. We developed a high-energy veto system to veto data taking of the high-energy events. The system uses a Skutek digital pulse processor, DDC-10[129]. This module receives the summed waveform of the attenuated bottom array as input. It gives a veto signal to the V1495 to halt the acquisition of a high-energy event for 10 ms [130].

Crate controller The crate controller is a CAEN V2718[127] module that sends signals to the DAQ. Every subdetector has its down V2718. Its primary function is to send the S-IN signal to all digitizers; this signal is used to start and stop the acquisition. The S-IN signal is distributed to all digitizers using logic fans, with the arrival time spread lower than four ns for all digitizers.

The TPC crate controller has three outputs for generating the S-IN signals. One is for the TPC, and the other two are for generating gate signals to propagate the TPC S-IN to the NV and MV when operating in linked mode. The other use of the crate controller is during the LED calibration of the TPC PMTs. The V2718 can generate pulses with frequencies between mHz and MHz, which are propagated hardware modules. The V2718 can also generate a gate pulse, used as a periodic trigger to send the LED signals to the TPC. After a 10 μs delay to account for the time it takes to generate and propagate the LED signal into the TPC through optical fiber, this trigger is sent to the digitizers to acquire the data.

Time synchronization The V1724 uses its internal clock or receives an external reference clock signal. It is also programmed to output its clock. The CAEN DT4700 clock generator module generates the clock signal, which is then propagated to the digitizers. The Phase-locked loop (PLL) circuit inside the digitizer synchronizes the internal clock with the external source clock, allowing multiple digitizers to be synchronized to the external clock. This is used to synchronize the entire system to the same clock. The first digitizer in every VME crate receives the clock signal from the clock module, and this signal is further propagated through the entire crate. The time offsets in the clock chain are manually calibrated to ensure synchronization across a crate.

GPS Synchronization A GPS module, Septentrio PolaRx4[131], propagates a periodic timestamp to all DAQ subsystems to provide an external time reference. The clock module receives signals from GPS satellites at the above-ground lab to generate a clock signal. This signal is sent to the underground lab via an optical link to a secondary module. The module generates a 0.1 Hz NIM output propagated to the TPC and NV acquisition monitors. This timestamp provides a global timestamp to every event in the DAQ system with 10ns precision. As XENONnT is sensitive to neutrino interactions, the GPS timestamp can precisely record the absolute timestamp of a possible neutrino interaction from a supernova. The GPS timestamp allows correlating the signal from XENONnT to that of other experiments[132].

Readers The digitizers are readout with three 2U Fujitsu PRIMERGY RX2530 M4 servers[133], 2 Xeon Silver 4114 CPUs, and 192 GB of memory each. Two additional PRIMERGY RX2540 M2 servers are connected and can be used as backup machines if one of the primary servers becomes unavailable. All reader servers have CAEN A3818 PCI express controller cards to connect to the digitizers and crate controllers, capable of supporting a maximum of 48 digitizers per reader. The CAEN V2817 module used as crate controller is connected to reader 0. The data outputs of the V1724s are daisy-chained in groups of eight and connected to one of the readout servers. The Acquisition Monitor is connected with its own optical link. The connection uses the CAEN proprietary CONET2 protocol.

The readers have four 960 GB write-intensive SSDs each, used to create a 10 TB CEPH[134] storage cluster. This allows all readers to write to a shared disk mountable by the *event builder* machines. As the CEPH drive is used as a short-term buffer, its configuration is set to the equivalent of RAID0. In RAID0, data is distributed evenly over all disks, without redundancy or fault tolerance[135]. This allows maximum read and write speed at $\mathcal{O}$ (1 GB/s).

While the data rate in normal run conditions is approximately 30 MB/s, the rate can increase substantially during calibration runs.

Event builders The event builders (EBs) are three Fujitsu PRIMERGY RX2540 M4[133], with 202 GB memory each, and three PRIMERGY RX2540 M1, 192 GB memory servers as backup. The primary servers are responsible for the live processing of the incoming data. Two of the three backup servers act as extra redundancy. The third is used to produce online monitor plots and handle slack requests. DAQ experts can also use it to access the data quickly for diagnostics. The hard disks of the EBs are accessible by other servers in the LNGS network. When one of the event builders marks data as processed, it is uploaded by one of the other servers into a rucio catalog [136] and distributed over various analysis sites.

Neutron veto DAQ The neutron veto DAQ acquires signals from 120 Hamamatsu R5912 100WA D30 8-inch PMTs[124]. The structure of the DAQ is a smaller version of the TPC. The PMTs are connected to 8 CAEN V1730B[127], 14-bit 500MS/s digitizers, running the DPP-DAW firmware for triggerless readout of every channel. It also has a V2718 create controller, a V1724 acquisition monitor, and a V1495 logic module in a VME crate. The neutron veto digitizers are connected to a Fujitsu server with an Intel Xeon Silver 4114 CPU via optical links using the CONET2 protocol.

Muon veto DAQ The Muon veto[137] DAQ operates differently than the TPC and NV systems. The Muon veto is a triggered system. 11 CAEN V1724 digitizers are connected to 84 Hamamatsu R5912 HQE ASSY 8-inch PMTs, operating using the default Zero Suppression (ZLE) firmware. If a signal is above the threshold in one of the channels, an LVDS signal is sent to a CAEN V1495 module. This module runs firmware programmed to send a trigger signal to the MV DAQ if it records a coincidence signal of five PMTs within 300 ns. The trigger signal is propagated to the digitizers, leading to the data recording. The MV does not have an acquisition monitor; the MV trigger is connected to the NV acquisition monitor.

4.2 Software

This section describes the two software systems required to operate the DAQ. The first system is required for the readout, *redax*. While the second system, *strax*, is used for data processing.

4.2.1 Redax

The DAQ software system *redax*[138] functions as the system's core, controlling the DAQ hardware from initialization to readout. Figure 4.6 shows a schematic of the readout logic. Redax is centered around two MongoDB databases[139], the DAQ and the Runs databases, and a dispatcher software module. What every part of the system is and should be doing is stored in the DAQ database. The user interacts with the database to start or stop acquisition, and the dispatcher ensures that the system reacts accordingly. In case of a DAQ problem halting the acquisition, either in software or hardware, the dispatcher calls a separate module, the hypervisor, to solve most issues without expert intervention. The readout software continuously polls the digitizers to read out new data. When new data is available, it is transferred from the digitizers to the readers via block transfers mediated by the CAENVMElib C++ library. After transfer, the data is parsed into individual pulses and reformatted from the binary CAEN format to the tabular structure used in later processing. The data is written to disk in files, called chunks, of 5-20 second time intervals. As data is processed per chunk, the 5-second time interval was chosen to reduce memory usage per chunk. However, due to the short time interval, the number of files produced per run ($\sim$ 1000) is problematic for the computing pipeline. Therefore, the time interval was increased to 20 seconds. A pre-and post-chunk overlap region is written for 0.5 seconds alongside every chunk; this data is thus written twice. The processor uses this overlap interval to find a suitable time region with no data for 1 μs and disregards the data before (pre-chunk) and after (post-chunk). The disregarded time region is grouped with either the previous or next chunk. If no suitable time window is found, 1 μs of data is marked as artificial deadtime. The 0.5-second chunk overlap is chosen to minimize this; artificial deadtime was not inserted during the background data taking in SR0 of XENONnT.

Databases The readout is organized around two databases: the DAQ database for system control, internal communication, and monitoring and the Runs database for storage of run metadata, both implemented in the so-called NoSQL database MongoDB[139]. The databases are further subdivided into separate collections for various purposes, such as for logging and the storage of configurations.

The Runs database has the primary server hosted at LNGS, with two replica sets hosted at Rice University and the University of Chicago, the main sites used for analysis. This ensures analysts can always access the Runs database and prevent data loss in case of a hardware failure. The Runs database tracks all run metadata, such as start and end times, operation modes,

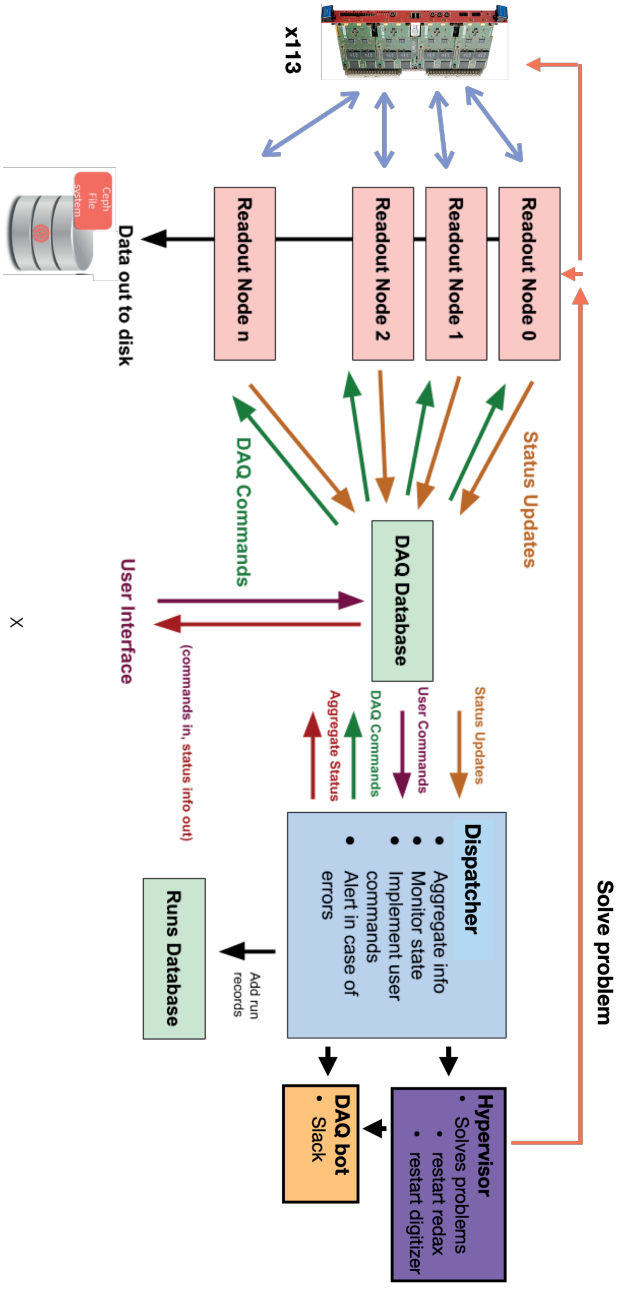

Figure 4.6 Schematic of the readout logic in *redax*. The user interacts with the system through a user interface connected to the DAQ database. The dispatcher monitors the user input, ensures all readout nodes correspond with the correct configuration, and writes metadata to the run database. If the system is in error, the hypervisor can solve most problems by restarting the failing subsystem. From [138].

DAQ configuration, and the file locations where all the data is stored. In a separate collection, data from the online monitor is stored so analysts can access summary data within $\mathcal{O}$ (30) seconds after the DAQ has recorded the data. This is used for monitoring during hardware installation or calibration runs.

The DAQ database is only for the operation of the DAQ and is not accessible by analysts. The data in the DAQ database is not stored long-term. The status of all redax readout processes, the status of the live processing, and the servers' performance are all tracked in this database. It is configured to store data only for three days to keep the database size limited. Apart from this internal communication, the database also stores run configurations and the operational goal state set by the user using the website.

The run configuration contains all the settings required to run the DAQ, such as the configuration of the digitizers, the location to store data, and the time duration of each run. Table 4.1 gives the values of used registers on the V1724.

Register	**Value**	**Comment**
EF1C	FF	Events per BLT
811C	D10	Front panel IO (0x80 to turn busy on)
81A0	200	Front panel IO new features
EF00	10	BERR register, 10=enable BERR
8100	1	Acquisition control register. 1 - S-IN control.
8120	FF	Channel enable mask. FF= all channels on
8000	3310	Front panel I/O register. 3310 - new FW with DPP
8080	510000	DPP register. 510000 - DPP on, 256 sample baseline
8034	1FF	Input delay in words
8038	19	Words in pretrigger window
8020	32	Event size register.
8078	19	Samples under the threshold to close event.

Table 4.1 Addresses and values in hex of the used configuration of the V1724. More information on the registers can be found in the CAEN user manual[128].

Dispatcher The dispatcher is a Python program running on one of the DAQ servers to take the user's operational goal state and ensure the system reaches the desired operating state. The dispatcher monitors the status of all the readout processes continuously. The system can be idle, arming, running, or not responding, and the dispatcher matches this to the operational goal state by sending out the corresponding commands or by doing nothing. The

readout is stopped and restarted if the active run reaches the maximum run time (30 minutes by default during SR0). If one of the readout processes is not responding, the dispatcher can kill and restart the specific process. If one of the digitizers or VME crates is not responding, the dispatcher can power cycle the crate to restore normal operational behavior. A reader will be restarted if it is unresponsive for 10 seconds. The arm, start and stop have a 60, 20, and 30-second response time, respectively, between command issue and acknowledgment. If the state is not reached within the timeout, it will be retried up to three times before one of the crates is restarted. The dispatcher also communicates with the Runs database by adding a document when starting a run with the readout configuration and the required settings for the live processing. When stopping a run, the document is updated with the end time of the run and additional operational data, such as the average data rates.

4.2.2 Readout

This section describes the three operational states of the DAQ: arming, starting, and stopping.

Arming The arming sequence has to be completed before starting the readout. Redax will read the user-specified configuration used for the readout. During this sequence Redax will configure the digitizers and perform a baseline fitting routine to set the DAC values close to 16000 ADC counts, slightly below the maximum of 16385 (14-bit), to optimize the usage of the dynamic range of the digitizer (0-2.25V). One readout thread per optical link is started, and a user-specified number of processing threads, 8 per reader by default, are to reformat the read data.

Starting After completing the arming sequence, redax can start the readout. When the crate controller raises the S-IN signal, the data is read from the digitizer, unpacked from its CAEN event structure, and formatted for processing by the analysis framework. The data is compressed and written to the CEPH storage disk in chunks.

Stopping If the acquisition is stopped, the S-IN signal is lowered, and the last data is read from the digitizer buffers and written to disk. The digitizers are reset, and all remaining threads and links to the digitizers are closed.

4.2.3 Strax

The data acquired by the front-end electronics are processed with XENONnT's analysis framework *Straxen*[140], built upon the generic TPC data processor framework *Strax*[141]. We refer to the framework as strax for simplicity.

Strax is the Python-based analysis framework developed for XENONnT, aimed at fast reading and processing triggerless data. It is centered around *array-oriented programming*[142]. In XENON1T, the DAQ organized data in an event with a fixed start and end time set by the software trigger at the readout level. Data processing was done by looping over a list of events. In XENONnT, the data is represented as a stream using fixed-length NumPy arrays. The difference is illustrated in Figure 4.7. A significant advantage of this method is computation speed[143]. All algorithms are written using extensive NumPy[144] and Numba[145]-optimized routines to ensure fast processing Numba is a just-in-time python compiling Python into LLVM machine code that comes close to C or Fortran in performance.

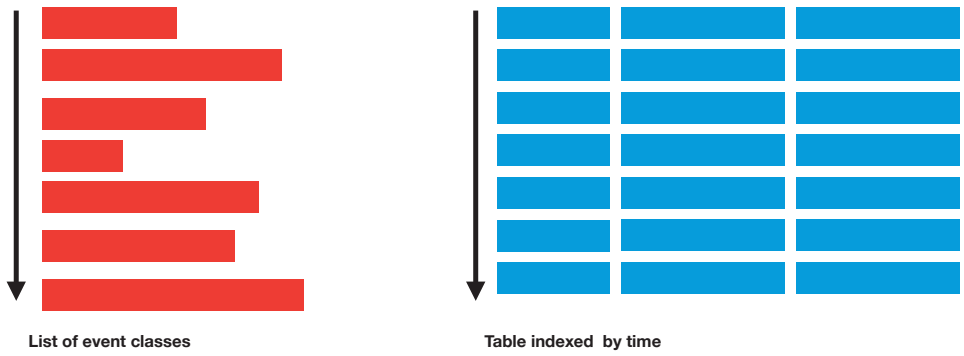

Figure 4.7 Illustration of the XENON1T data processing structure (Pax[146]), where processing is done by looping over a list of event objects (left), compared to the structure of XENONnT (strax), the processing is done over the same-size length arrays, resulting in a significant performance boost.

For raw data, this comes with a complication. The data from the DAQ digitizers are not fixed in length; they can be anywhere between the minimum and maximum pulse length set in the configuration. A pulse is distributed over multiple arrays to ensure the data fits on a fixed-length array. An index keeps track of which pulse the array belongs to.

The data processing is done in steps called *data types*. Figure 4.8 shows some of the data types' dependency graphs. Note the arrows show the dependency, not the flow of the data. The different colors indicate *data kinds*. Every row of data in the same data kind is guaranteed to have the same start and end time.

For example, the fifth entry of peak positions holds the position of the fifth entry in peaks. This allows data types of the same kind to be loaded together.

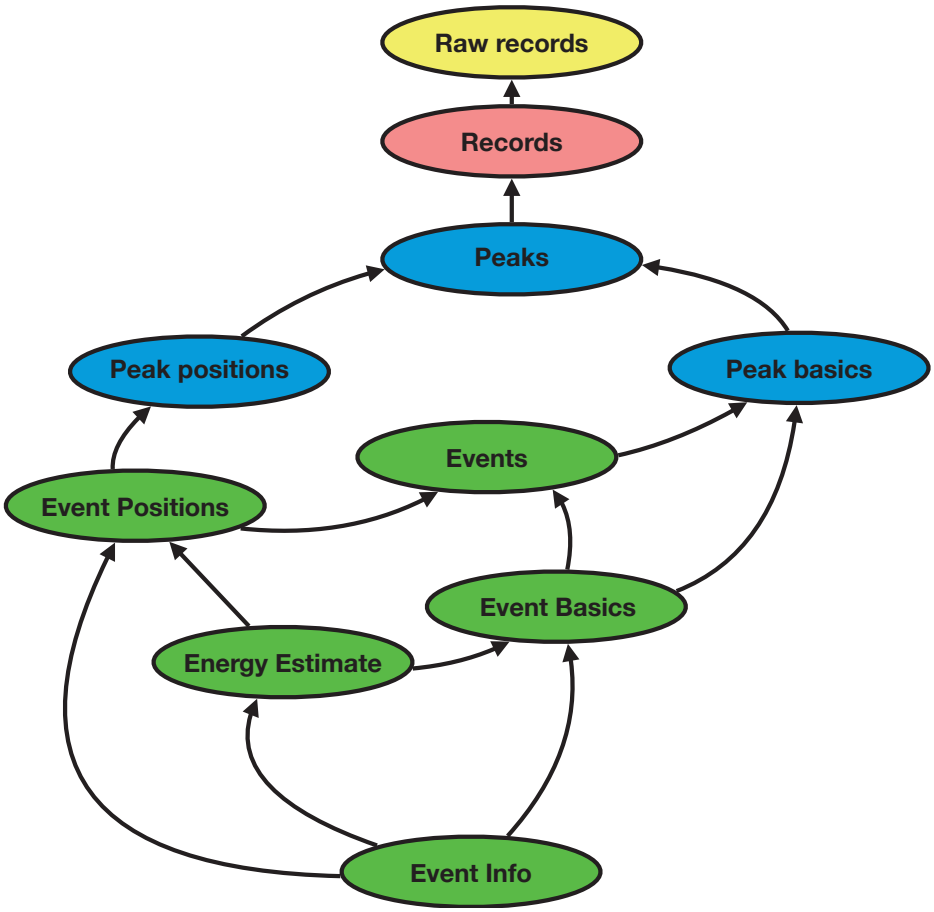

Figure 4.8 Dependency graph of different data types used in strax. Arrows indicate dependency, not data flow. Colors indicate *data kinds*; these data types can be loaded together.

The configuration used to process the data is stored in a metadata file for every data type. If a configuration changes, the data type is recalculated with all data types that depend on this. For example, if a position reconstruction algorithm changes, peak positions will have a different configuration. This will trigger the reprocessing of peak positions, event positions, energy estimates, and event info. Peak basics, events, and event basics, on the other hand, are independent of peak positions. Therefore, these data types do not have to be reprocessed. This avoids having to redo all data processing every time a

particular step is changed.

After processing, the data is uploaded to a Rucio catalogue[136] and distributed over various computing facilities worldwide for storage and analysts to work with. The EBs monitor the Runs database for runs whose data is ready for processing. When an EB is finished processing a run, it marks it ready for transfer in the Runs database, after which it will be uploaded to the Rucio catalog.

Online monitoring One of the event builders runs online monitoring software together with a Slack[147] bot to allow analysts fast access to data while it is being recorded. The online monitoring script uploads data as soon as the event builder is finished processing the chunk of data, between 5 - 20 seconds, to the MongoDB, making data available within $\mathcal{O}(30$ s) after detection by the PMTs. The Slack bot lets anyone with access to the XENONnT Slack channel request summary plots of recent runs. The variables used for DM searches are not included; therefore, they cannot circumvent blinding cuts.

4.2.4 User interface

The DAQ user interface is run by Nodiaq, a NodeJS website linked to the DAQ database. A control page lets the user specify the run mode and duration. The status page shows the performance and status of all the DAQ servers. The monitor page, shown in Figure 4.9, views the TPC with the live data rates of all channels. Finally, the website offers API access to the DAQ database used by Slow Control to monitor for hotspots, high data rates ($>2\ \sigma$ of the median PMT rate) of four PMTs next to each other for an extended period (5 minutes), or a high data rate (>30 MB/s) on one reader. In both cases, an alarm is raised to alert operations.

4.3 Performance

To assess the performance of the DAQ, we use several metrics. Here we focus on the data rate, livetime, electronic noise conditions, and live processing speed.

4.3.1 Livetime

All three DAQ subsystems operated stably during XENONnT's commissioning and SR0, approximately 300 days. The median and RMS of the data rates for Science data and calibration modes ^{83m}Kr, ^{222}Rn, and ^{241}AmBe are shown in Table 4.2. The median dead time per chunk during this period is shown in Figure 4.10. During science data taking, the dead time is well below 1% (black

Figure 4.9 The status page of the DAQ website. The plot shows the data rates of all three subsystems. The status cards indicate the rate of each server in real time, showing data rates of all reader servers, the activity of the event builder servers, the health of the storage disk CEPH, and recent DAQ commands issued by the user.

points). The science data points with data rates higher than 40 MB/s are due to a muon interacting with the xenon. The muon deposits large amounts of energy over its entire track through the TPC. This leads to abnormally high rates and, thus, dead time. In the high rate ^{220}Rn and AmBe calibration, the dead time increases up to $\sim$ 10%. Above $\sim$ 150 MB/s, we start seeing pileup events, making the data unusable for standard analysis.

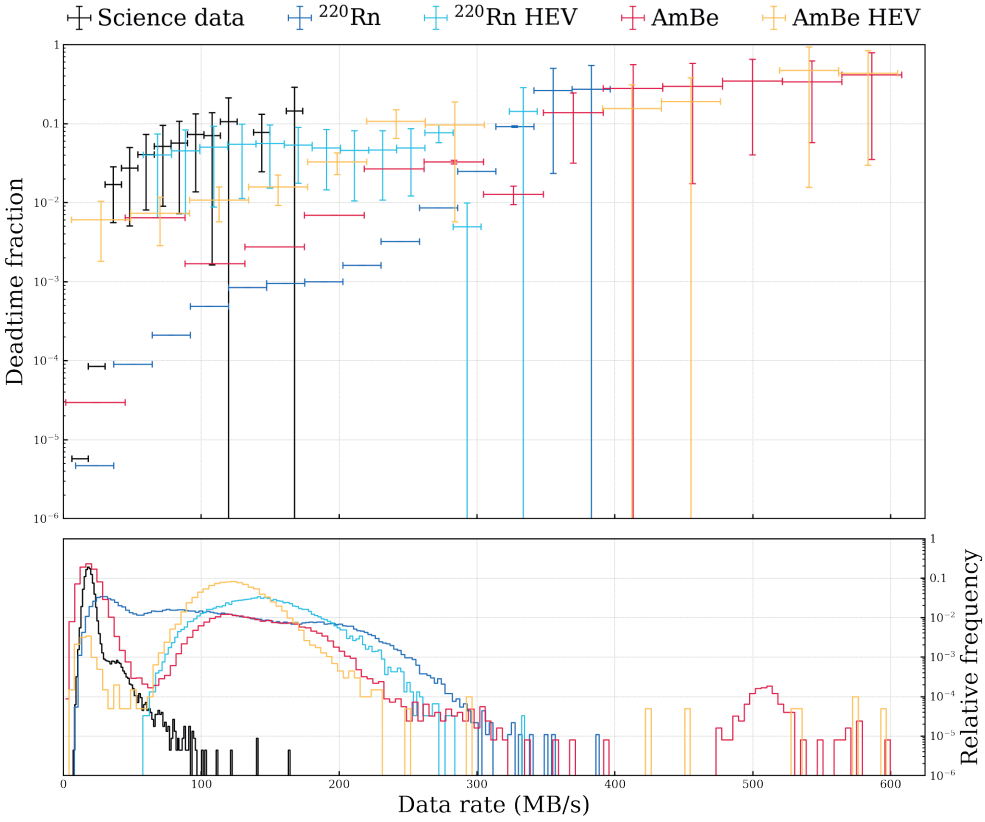

Figure 4.10 DAQ median deadtime fraction as a function of data rate for science data, ^{222}Rn, and AmBe calibration runs per chunk (5 - 20 s of data). Regular science data taking has rates up to $\sim$ 50 MB/s; higher rates are caused when cosmic-ray muons pass through the xenon ($\sim$ 1 per hour). Above 150 MB/s pileup, due to the SR0 detector conditions, makes data unusable for analysis. Adapted from [148]

4.3.2 Live processing

After the data is written to disk by the readers, the event builders are responsible for processing the data. During SR0, the EBs could process data faster than the incoming data rate. This allows the live monitoring of the detector. Figure

Mode	Median (MB/s)	RMS (MB/s)
Science data	14.6	3.8
^{83m}Kr	51.8	7.2
^{222}Rn	80.5	8.9
^{241}AmBe	53.4	7.3

Table 4.2 Median and RMS of the data rates of the DAQ during science data taking (background) and ^{83m}Kr, ^{222}Rn and AmBe calibration modes.

4.11 shows the processing speed, as run duration over processing time, as a function of the data rate for different levels of processing of high statistics ^{83m}Kr calibration data taken during the commissioning phase of XENONnT. Raw records are the lowest-level data type, peaks are an intermediate data type, and events represent the fully processed data. The break-even points using one (three) EBs are indicated with the dashed line. As mentioned in the previous paragraph, science data does not exceed 50 MB/s, while pileup starts occurring above 150 MB/s in the calibration data. Both will occur before the break-even point of live processing with one EB.

4.3.3 Electronic noise

The pulses measured from the PMTs are on top of electronic noise. Low noise levels are crucial to ensure a low threshold experiment, as a noise spike can appear as a photoelectron pulse. Another possibility is that electronic noise causes a jitter in the digitizer's clock cables. This can cause a PLL to unlock, i.e., lose the time synchronization between the external and internal clock of the digitizer, causing the acquisition to stop. We carefully minimize the electronic noise by following a "star-shaped" grounding scheme and routing cables.

To measure the noise level in XENONnT, 1-minute runs are taken weekly after LED calibration of the PMTs. Noise runs use forced acquisition to read 1 ms of data every second. Figure 4.12 shows the mean RMS of the baseline taken during a noise run. The median value of the RMS is 1.7 (0.23), 2.6 (0.35), and 1.2 (0.16) ADC counts (mV) for the top, bottom, and top high energy arrays, respectively. The difference between the top and bottom arrays is likely due to the different High Voltage (HV) filter boxes used. For XENON1T, three low-pass filter boxes, made of an array of LRC low-pass filters with ten kΩ resistors, were manufactured to reduce the high-frequency noise from the HV supply[120][149]. For XENONnT, three additional filter boxes were manufactured with 12 kΩ resistors. However, this was not expected to affect performance and is used for the power supply to the bottom array PMTs, while

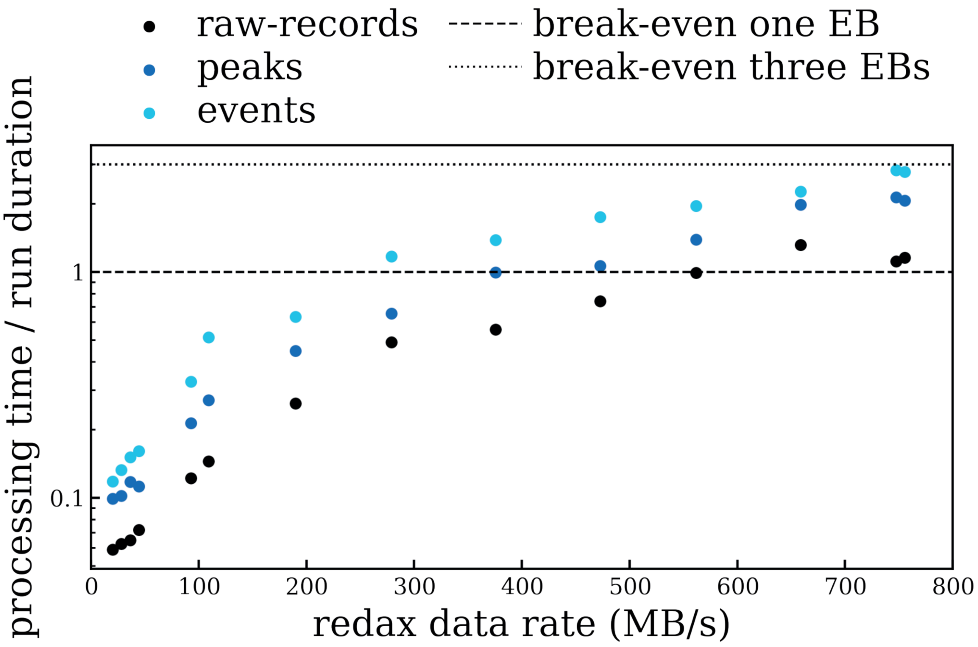

Figure 4.11 DAQ median deadtime fraction as a function of data rate for science data, ^{222}Rn, and AmBe calibration runs per chunk (5 - 20 s of data). Regular science data taking has rates up to $\sim$ 50 MB/s; muons cause higher rates. Above 150 MB/s pileup makes data unusable for analysis. Adapted from [148]

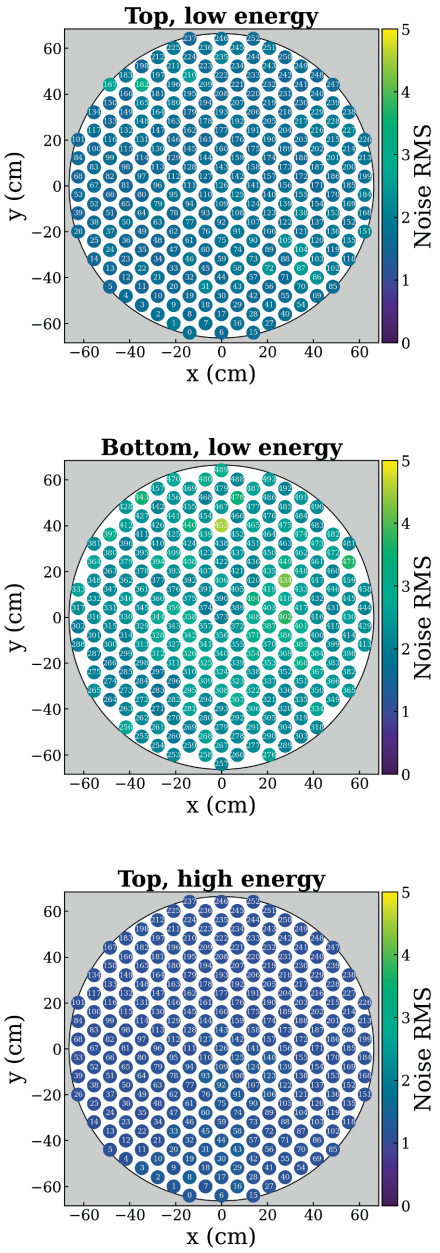

Figure 4.12 RMS of the pulse acquired during noise data taking of the top and bottom array for the low-energy and high-energy top array channels. The median RMS of the top array is 1.7 ADC counts, while the bottom array RMS is 2.6 ADC counts. The difference is attributed to the different designs of the low-pass filter boxes used for the top array concerning the bottom array. The high-energy channel RMS is 1.16 ADC counts.

the XENON1T filter boxes are used to power the top array PMTs.

Figure 4.13 shows the noise power spectrum averaged over five events. Here, we identify individual components of the noise spectrum. The most prominent peak is around 25 kHz, related to the internal clock of CAEN digitizers and below the cut-off frequency of the filter boxes of 338 kHz and 282 kHz for the10kΩ and 12 kΩ versions[130].

4.4 Conclusion

The XENONnT DAQ is a well-performing, triggerless system, which took ∼400 days of data in various detector conditions during commissioning, calibration, and science data modes. The system can read out and process high data rates with high live time throughout its operation. The triggerless design allows for data storage, allowing analysis a high degree of flexibility for setting their own trigger and coincidence requirements on the signals. The three subsystems can acquire data independently or be run as a single system in linked mode. The DAQ has taken data with rates up to 500 MB/s. The deadtime fraction during science data operation is $\mathcal{O}(10^{-5})$, and up to ∼10% during high rate calibration. High-level data is available for analysis directly due to online processing. This also enables analysts to monitor detection conditions during hardware operations on the detector.

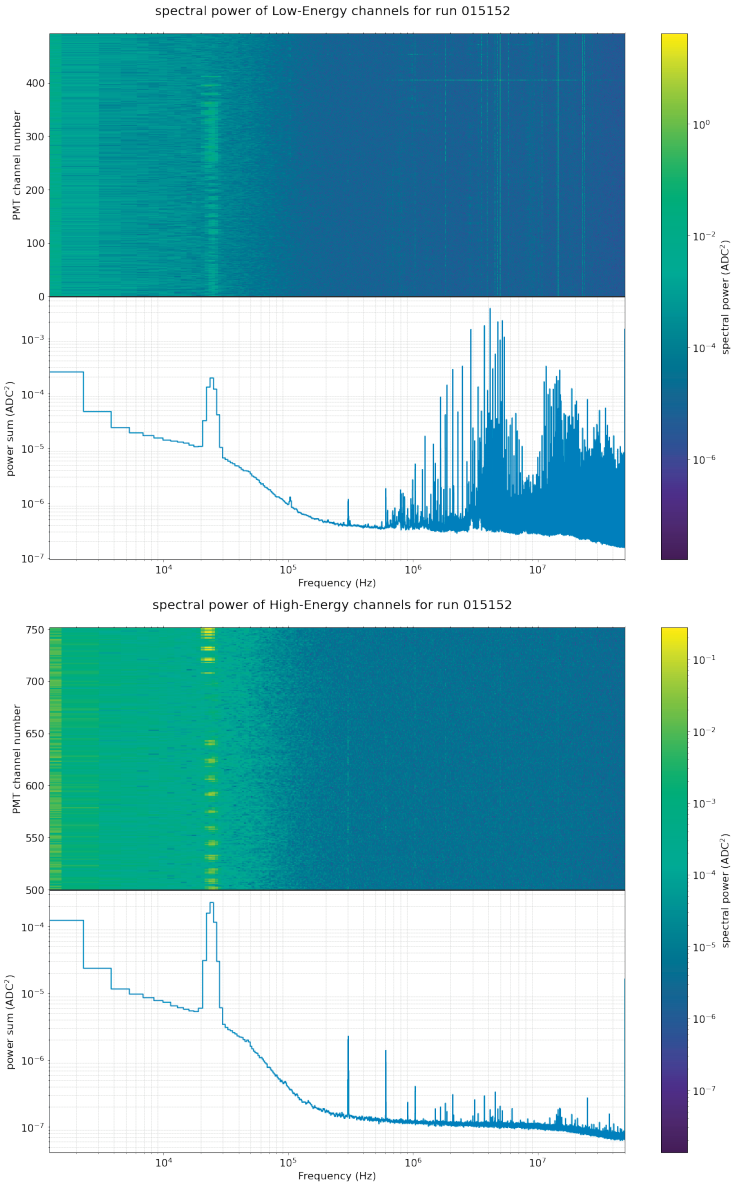

Figure 4.13 Noise power spectrum of the low energy (top) and high energy (bottom) channels. The plot shows the amplitude (spectral power) of all noise frequencies and is summed over all channels. The peak at 25 kHz corresponds to a frequency used inside CAEN digitizers. The high-frequency noise ($>10^6$ Hz) comes from the PMTs, which is significantly reduced in the high-energy channels due to the attenuation of these channels.

5

XENONnT Monte Carlo framework

Monte Carlo (MC) simulations are a crucial tool used at every stage of an experiment, from assessing the feasibility of a detector design to providing input for data analysis. This chapter focuses on the XENONnT simulation software. The framework consists of three separate packages: Geant4[150] (G4), EPIX[151], and WFSim[152] as shown in Figure 5.1. The first component involves generating and tracking particles through the detector, which G4 performs. The second component is responsible for calculating the xenon response and is done by EPIX. Finally, WFSim is responsible for simulating the response of the detector. Each component has a specific function and follows a series of steps to generate the desired output. The entire framework is contained within a CernVM File System (CVMFS) container[153], which includes scripts for mass-producing simulations.

5.1 Geant4

Geant4 (G4)[150] is a software package to generate events and track particles that pass through a detector[155]. In the context of the XENONnT experiment, G4 is used to simulate the interactions of particles within the detector accurately, taking into account the geometry and all relevant physics processes. Here, we only give a brief overview of the XENONnT G4 implementation.

The XENONnT G4 detector model closely resembles the real experiment, including the chemical compositions of the materials, optical properties, and exact dimensions of the XENONnT design. Figure 5.2 shows a visualization of the XENONnT detector model.

Accurately modeling optical properties is crucial to ensure a faithful

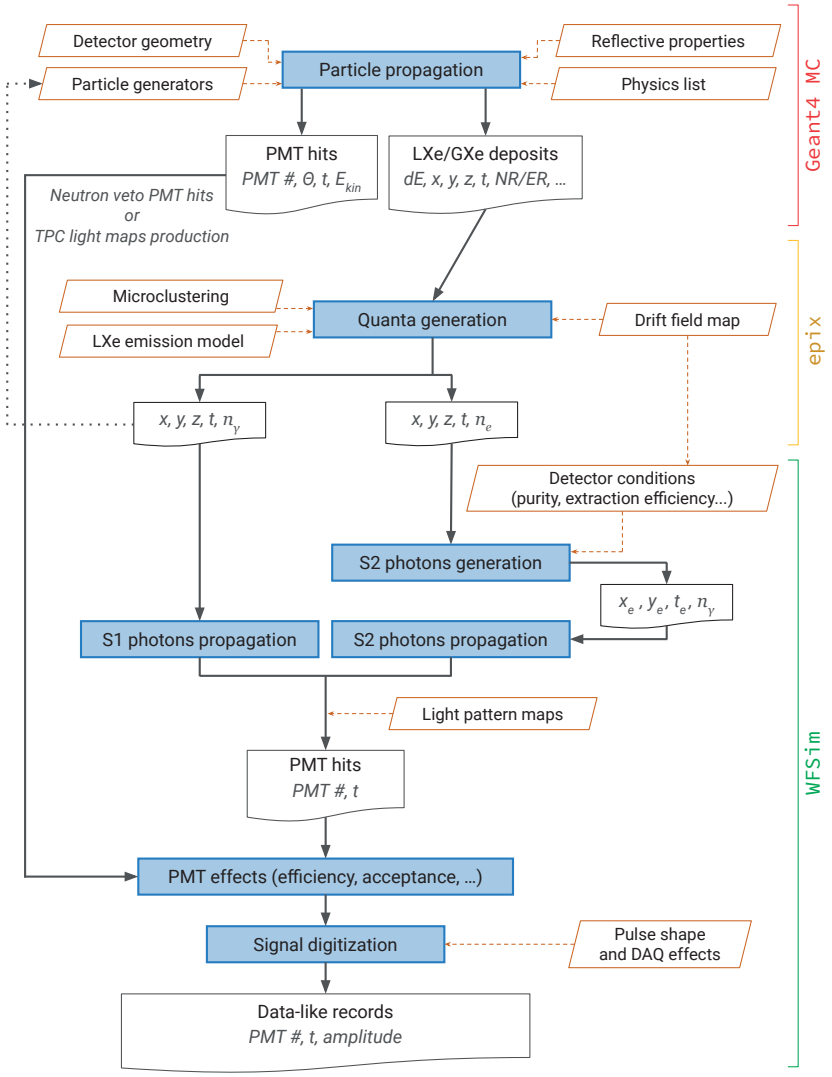

Figure 5.1 Flowchart of the XENONnT simulation framework. The colored brackets on the right indicate the package responsible for each step (red: Geant4, yellow: EPIX, green: WFsim). Geant4 propagates particles through the detector volume, providing information on energy deposits and interaction vertices. EPIX takes the energy deposits and calculates the light and charge yield of the deposited energy after microclustering. WFSim uses the number of photons and electrons produced to simulate the corresponding pulses in a format similar to the data acquisition (DAQ) system's PMT pulses. From [154].

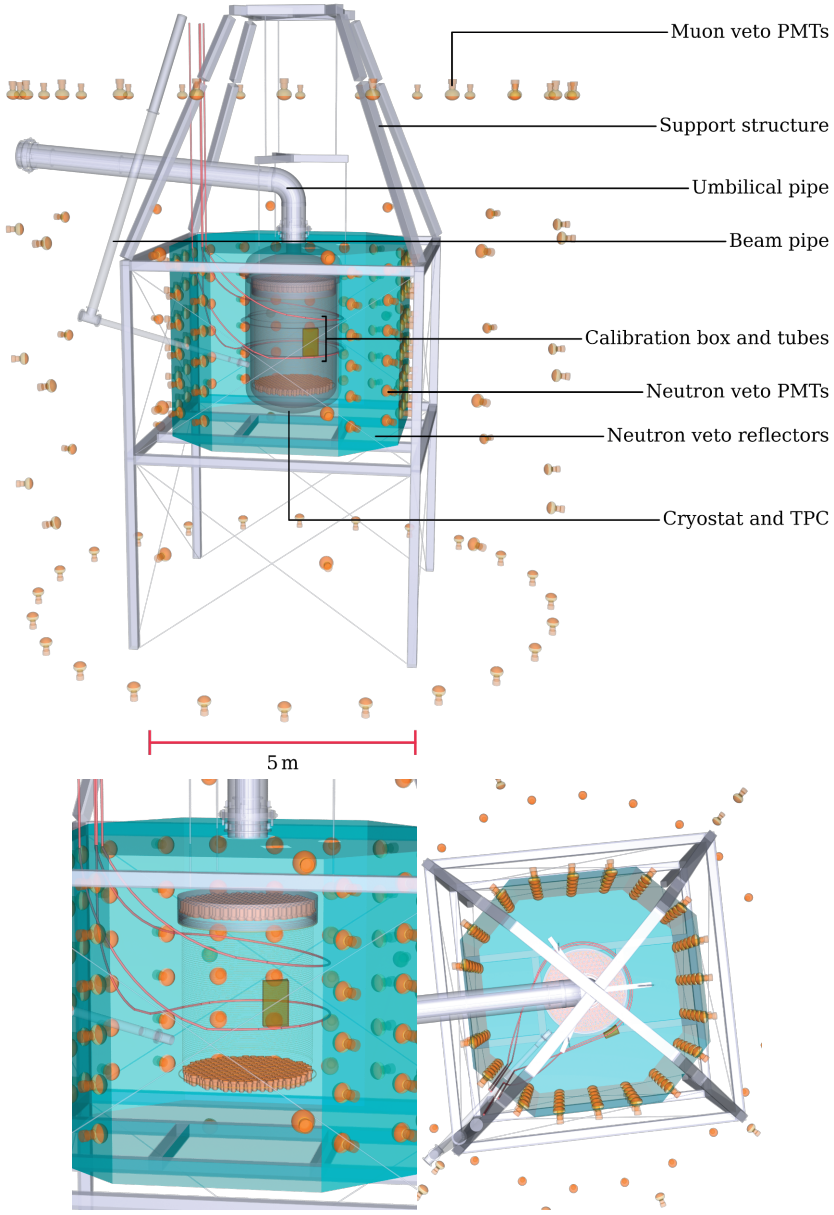

Figure 5.2 Geant4 rendering of the XENONnT experiment. For clarity, the water tank, neutron veto support structure, and parts of the calibration system have been omitted. The turquoise box represents the reflector panels of the Neutron Veto. (Bottom) Close-up view of the Time Projection Chamber (TPC) from the side (left) and top (right), excluding the cryostat. This detailed view showcases internal components such as the top and bottom array of Photomultiplier Tubes (PMTs), top electrodes, and field-shaping wires. Adapted from [154].

XENONnT simulation. The optical parameters for the TPC simulation are carefully determined. The refractive index of LXe is set to 1.63, approximating the average refractive index of LXe at the scintillation peak wavelength of 175 nm. The refractive index of gaseous xenon (GXe) is assumed to be 1. Rayleigh scattering, which describes the elastic scattering of light on particles smaller than the wavelength of light, is characterized by a scattering length of 30 meters, based on theoretical calculations and data-MC matching[106]. The photon absorption length depends on the concentration of impurities in LXe and is currently set to 50 meters based on the XENON1T data. The reflectivity of the PTFE surfaces is assumed to be 99%, as determined by measurements in XENON1T[106].

Currently, G4 version 10.4-patch02 is used for XENONnT. Radioactive decays are simulated via the G4RadioactiveDecay process. If the daughter is an isomer, prompt-de-excitation is done by G4PhotonEvaporaition, where the relevant parameters are taken from Evaluated Nuclear Data Files (ENDF)[156]. The Livermore physics list is used for high-precision gamma- and electron interaction tracking.

5.2 EPIX

The EPIX (Electrons and Photons Instructions for Xenon) package is a component of the simulation chain in the XENONnT experiment. It converts the energy deposited obtained from Geant4 simulations into detectable photons and electrons used to simulate data.

One of the primary functionalities of EPIX is clustering energy depositions. Due to the non-linear relationship between energy and light/charge yield in LXe, it is essential to group interactions occurring within a specific length scale. EPIX employs the DBSCAN (Density-Based Spatial Clustering of Applications with Noise) algorithm for this clustering process. This algorithm merges energy deposits close together in space (within five µm) and time (within one ns). The individual energy deposits are combined by adding their energies, and the new position and time are calculated as the weighted averages of the individual interactions. The interaction type, nuclear or electron recoil, is determined based on the most significant energy deposit within the cluster.

To calculate the final number of electron and UV photon quanta, EPIX uses the LXe emission model from NEST[109], which depends on the electric field, energy deposition, and interaction type. The electric field is obtained from a drift field map calculated using the COMSOL Multiphysics package. Only the produced photons are stored in cases where interactions occur outside the drift region, as the electrons will not contribute to a measurable signal.

EPIX converts the Geant4 simulation output into detectable quanta by performing these steps, facilitating subsequent waveform simulation (WFSim) in the XENONnT experiment.

5.3 WFSim

The WFSim package[152] simulates the detector response for a given number of quanta, photons, or electrons at a given position. The bottom part of Figure 5.1 shows all the required steps. WFSim provides a strax interface to simulate XENONnT data in the same format as the XENONnT DAQ. It can be run as a standalone package, with user-specified instruction, or with Geant4 and Epix for high-precision simulations.

5.3.1 S1 simulation

To simulate the detector response of an S1, the distribution of photons over all channels and their arrival time needs to be calculated. The timing distribution is calculated using a combination of NEST to calculate the scintillation delay of the LXe and G4 spline to account for the propagation time.

Scintillation delay The scintillation of LXe comes from the decay of the excimer state. This state is the singlet ($\sim$ four ns decay time) or the triplet state ($\sim$ 22 ns). The ratio of the population of the two states depends on the interaction particle type, energy deposition, and the electric field at the interaction vertex[157]. As recombination leads to delayed excimer production, this process broadens the time distribution[158]. The delay of ERs is higher for higher energies, while for NRs, the delay is smaller for higher energies. For ERs, the additional delay is due to the increased contribution of recombination to the excimers, increasing the scintillation delay. For NRs, this effect is suppressed.

Photon propagation Photons are propagated to PMTs via the *S1 pattern map*. This map gives every PMT the probability of absorbing a photon for a given position in the TPC. When the S1 pattern map is summed over all PMTs, it is called the *light collection efficiency* (LCE) map, giving the fraction of detected photons as a function of R and z within the TPC. The LCE map is shown in Figure 5.3. The R^2-dependence on the LCE map, a relative variation of 3 percent, comes from the PMTs with the highest QE in the center of the TPC, and the outer layer of PMTs partially overlaps with the TPC wall. The z-dependence comes from the increased distance photons need to travel before

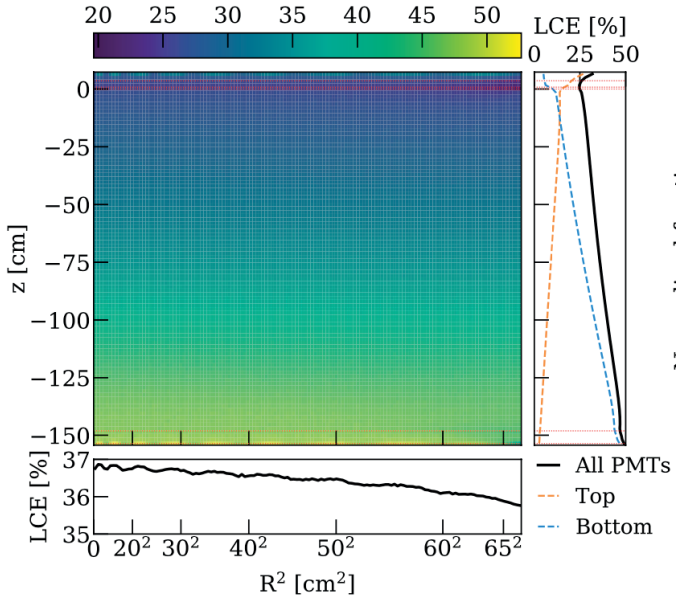

Figure 5.3 Light collection efficiency map of the XENONnT detector. The map illustrates the spatial distribution of light collection efficiency across the detector volume, providing insights into the detector's sensitivity to scintillation signals. Yellow represents regions with higher efficiency, while blue indicates lower efficiency.

reaching a PMT. The average LCE is 36%. The S1 photons are distributed over the PMTs, with the probabilities given by the S1 pattern map.

The scintillation delay time is calculated using NEST with the energy deposition and interaction time. The propagation time is derived from the same optical simulation. Figure 5.4 shows the cumulative distribution function of time distribution of photon arrival time on the photocathode of a PMT for different bins in z. The time distributions between the arrays are not symmetric in z. Due to the LXe/GXe interface, propagation times are longer to reach the top array. The CDFs draw photon arrival times for photons reaching the top and bottom array. Both delay times are added together for the final photon arrival time.

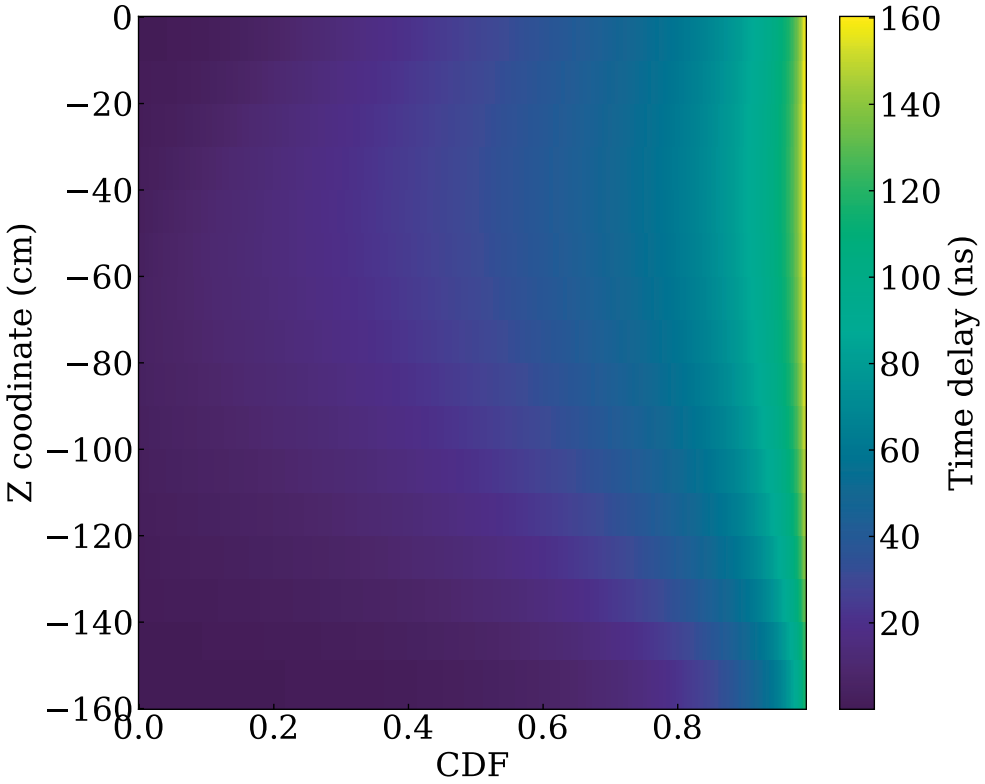

Figure 5.4 Propagation delay for S1 photons to arrive at the PMT photocathode modeled by Geant4 for different bins in z in XENONnT used in WFSim. The arrival time of every photon is sampled from this map according to the z-coordinate of the interaction.

5.3.2 S2 simulation

The first step in modeling the S2 signal is the transport of the electrons towards the LXe/GXe interface. Electrons drift towards the interface due to the electric field between the cathode and the gate electrodes. Important parameters used for simulating the S2 signal are given in Table 5.1.

S2 signal parameters	Design	SR0
Drift field (V/cm))	200	22.92
Drift velocity v_d (cm/ns)	0.000155	6.75 10^{-5}
Transverse diffusion D_T (cm^2/ns)	5.634 10^{-08}[159]	4.8 10^{-8} [159]
Longitudinal diffusion D_L(cm^2/ns)	2.439e-08[160]	4.45 10^{-8}
electron lifetime (ns)	4.5 10^6	13.9 10^6
electron extraction efficiency	0.96	0.55
g2 (pe/e)	40.9	17.1

Table 5.1 Parameters used to model S2 scintillation in liquid xenon by WFsim. The table includes values for the design parameters and those observed in SR0 conditions. [159, 160].

When drifting upward, the electrons follow the electric field lines. The drift velocity is calculated using the drift velocity map, inferred from the electric field simulations. Diffusion is modeled with Sorensen's diffusion model[161], as follows:

$$\sigma_{L,z} = \sqrt{\frac{2D_L t_d}{v_d^2}}, \tag{5.1}$$

$$\sigma_{L,R} = \sqrt{\frac{2D_T t_d}{v_d^2}}, \tag{5.2}$$

with v_d the average drift velocity, t_d the drift time, D_L and D_T the longitudinal and transverse diffusion constants. The average drift velocity and longitudinal and transverse diffusion constants are inferred using COMSOL electric field simulations.

The number of electrons drops exponentially due to the electrons sticking to impurities in the LXe, mainly H_2O and O_2. The loss is parametrized using the electron lifetime τ of the LXe:

$$N_e(t_d) = n_e(0)\exp[\frac{-t_d}{\tau}], \tag{5.3}$$

with $N_e(t_d)$ the number of surviving electrons at the LXe/GXe interface, $n_e(0)$ the number of electrons at the interaction position, t_d the drift time, and τ the electron lifetime.

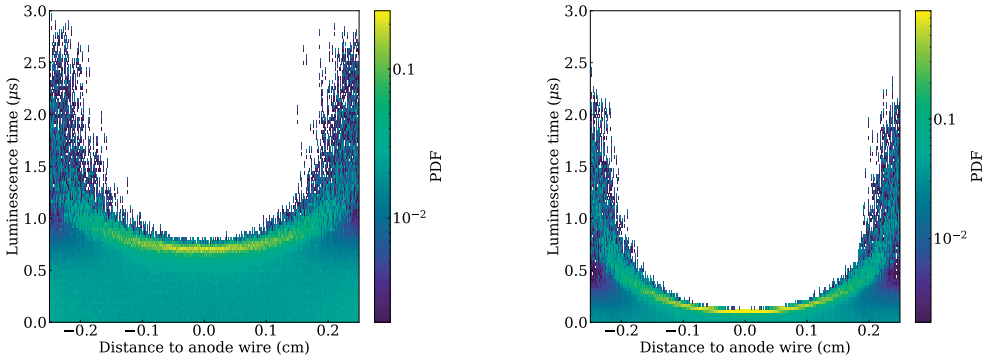

Figure 5.5 Scintillation delay as a function of the distance to the anode wires, as calculated by GARFIELD++[162] for XENONnT. The left plot corresponds to a liquid level of 3.2 mm above the gate, while the right plot corresponds to 6.7 mm. Electrons originating beneath the anode wire produce light on a shorter timescale compared to locations closer to a gate wire, an effect stronger for higher liquid levels.

Secondary Scintillation and Propagation Upon reaching the LXe/GXe interface, electrons are extracted into the GXe phase by the extraction field between the gate and anode. The electrons in the GXe gap generate the S2 signal through electroluminescence. The magnitude of this signal is influenced by the electric field in this region, GXe pressure, and the electron's path length within the gap. GARFIELD++, a simulation tool, has been employed to model the electroluminescence process in GXe[162]. Figure 5.5 shows variations in luminescence delay based on the gas gap size.

The electroluminescence time of the secondary scintillation process includes the excimer de-excitation extracted from NEST, which is similar to the approach for S1s. Subsequently, the propagation time of S2 photons is sampled from a Geant4 simulation. As the S2 signal is produced close to the top array, the propagation times for the top and bottom array are separated and shown in Figure 5.6

5.3.3 Pulse generation

After the S1 and S2 models calculate the photon arrival times and channels, the PMT pulses are simulated. The simulated photon arrival time is the photon's arrival time at the PMT's photocathode. This liberates an electron from the photocathode, which is amplified and generates a current. The time between the photon arriving at the photocathode and the generation of the PMT signal is sampled from a Gaussian distribution with a mean of 46 ns and a full-width half maximum of 9 ns[124] corresponding to the transit time spread (TTS) of

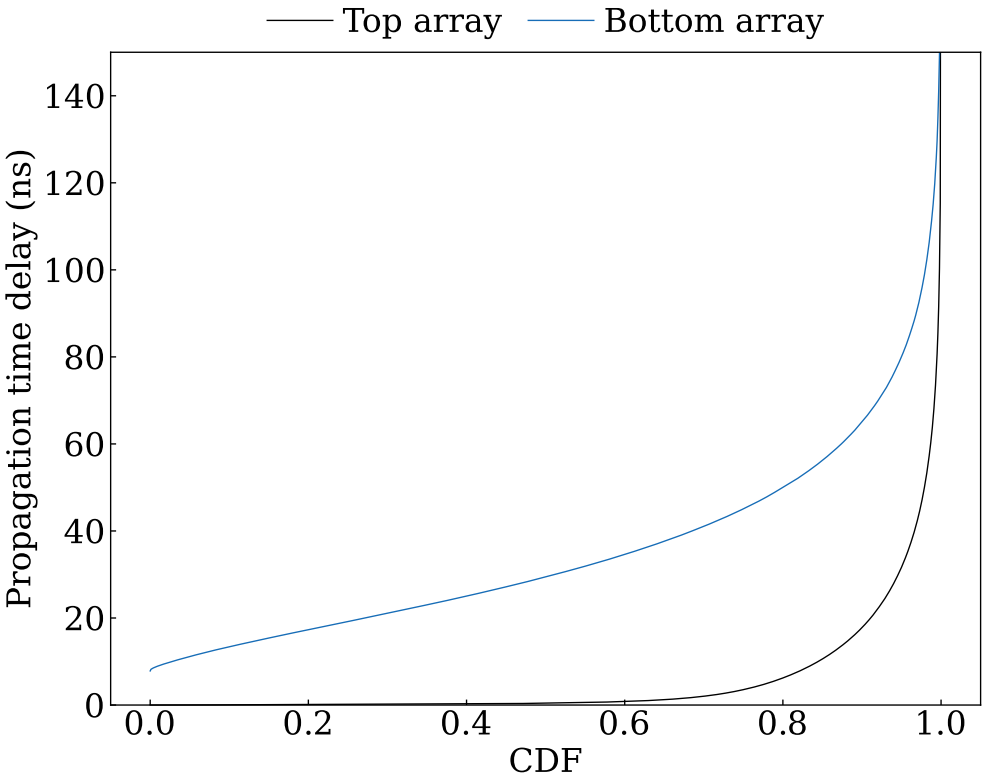

Figure 5.6 Propagation delay for S2 photons modeled by Geant4 for the top array (black) and the bottom array (blue) in XENONnT. The difference in time delay between the top and bottom array is due to the difference in path length as the S2 signal is generated close to the top array.

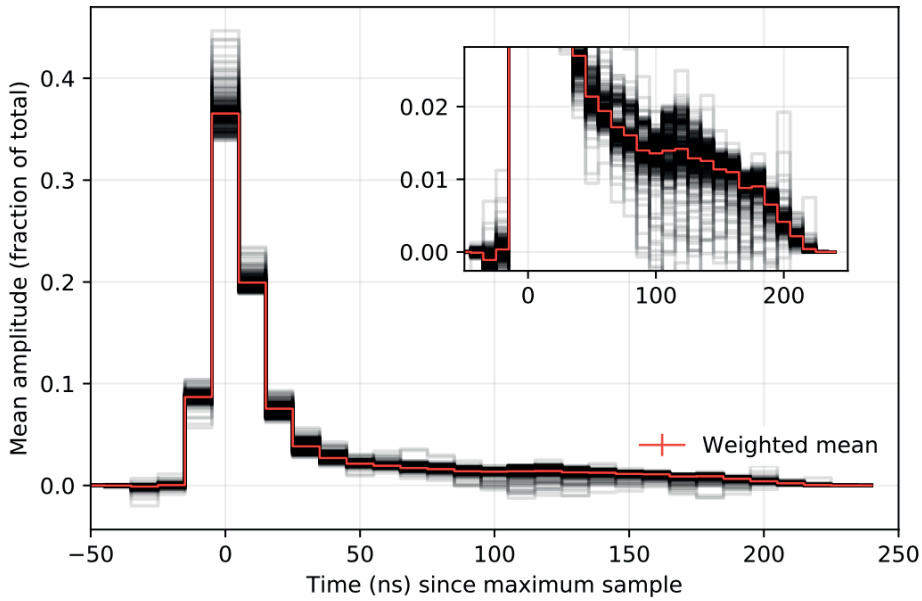

Figure 5.7 Averaged single photoelectron waveform shape in red. Black shows the single photoelectron waveform shape per PMT. The inset shows a zoom-in on the low-amplitude part of the waveform.

the Hamamatsu R11410.

The pulse shape of a single photoelectron (SPE) from a PMT is modeled on the average waveform of a lone hit, a peak from one photoelectron from one PMT. This average waveform is shown in Figure 5.7. The gray lines are the average waveform per channel; the red is the weighted mean waveform. The weighted mean waveform is fitted with an exponentially modified Gaussian and linear interpolation. The digitizers of XENONnT have a ten ns time resolution; however, the digitized pulse has a slight dependency on the time at which the photon arrived. To account for this, we shift the current of the SPE waveform with the remaining nanosecond precision. The amplitude of each photon is drawn from the SPE distribution on a per-channel basis. The resulting waveform data is written to a buffer.

5.3.4 Readout

The waveforms in the buffer require processing to look like real data. The amplitude of the simulated waveforms is in pe/sample. This is converted into

ADC/sample according to the formula:

$$ADC = \text{Baseline} - \frac{peRA2^b}{V}, \tag{5.4}$$

with R the PMT circuit load resistor (50 Ω), A the external amplification (10 for low energy channels, 0.5 for high energy channels), b the number of bits of the digitizer (14), and V the input voltage range of the digitizer (2 V). The baseline value is set to 16000. After conversion to ADC, noise is added to the signal with a sample of every individual PMT. Finally, the waveform is clipped at values above 2^{14} and below 0 to account for digitizer saturation.

To determine what data is written to disk, we run a self-triggering algorithm to find the time intervals where the data is above the threshold per PMT channel. The data written to disk are the intervals found with a pre-and post-threshold window of 50 samples, the same settings as used by the DAQ.

5.4 WFSim validation

Simulating particle interactions in a detector is crucial to get accurate and reliable data. WFSim is a tool that helps to simulate such interactions. However, to ensure the accuracy of the simulated data, it must be validated against known benchmarks. For this purpose, two distinct criteria are used.

The first criterion involves simulating monoenergetic gamma-ray lines to generate the Doke plot. This plot characterizes a detector's response to gamma rays of different energies.

The second criterion involves simulating the Low Energy Recoil (Low ER) background spectrum and comparing it to the observed data. The accurate simulation of these signals is crucial for dark matter searches as it helps to understand and distinguish interactions in the detector. Simulating low-energy signals is essential for dark matter searches. However, additional complexities come into play at higher energies, such as pair production for gamma rays above 1.02 MeV. Although these processes are essential for a comprehensive simulation, they are not the primary focus for simulating low-energy signals. Therefore, the validation presented here focuses on validating the Low ER background spectrum simulation.

5.4.1 Doke plot

To assess the accuracy of WFSim and the reconstruction carried out by the data processing software, we performed simulations of the monoenergetic gamma-ray lines of ^{83m}Kr, ^{131m}Xe, ^{60}Co, ^{208}Tl, ^{40}K, and ^{2}H. We used these simulations to calculate the doke plot, as described in Section 3.3.

Using equation 3.4, we derived the relationship between light yield (S1/E) and charge yield (S2/E), which is crucial for accurately modeling the signal response in the simulation. The equation is as follows:

$$\frac{S2}{E} = \frac{g_2}{W} - \frac{g_2}{g_1}\frac{S1}{E} \tag{5.5}$$

Here, g_1 represents the number of detected photoelectrons per emitted photon, and g_2 represents the number of detected photoelectrons per emitted electron.

We determined the g_1 and g_2 parameters, essential for accurately modeling the signal response in the simulation. These parameters help us understand the relationship between light and charge yield for monoenergetic gamma-ray lines.

Figure 5.8 shows the Doke plot, illustrating the relationship between light yield and charge yield for monoenergetic gamma-ray lines. The data points represent gamma-ray lines emitted by ^{83m}Kr, ^{131m}Xe, ^{60}Co, ^{208}Tl, ^{40}K, and ^{2}H. The linear fit represents the relationship between the two yields. Both values of g_1 (0.1547) and g_2 (15.92) are slightly below the configuration values in WFSim of g_1 (0.155) and g_2 (16.7). However, the overall agreement demonstrates the reliability of the simulation results.

5.4.2 Low ER spectrum

In this section, we will validate the simulation according to WFSim by simulating the SR0 background model and comparing it with the data. Specifically, we simulate the SR0 background model and compare it with the observed data. The background model used in the simulation is the XENONnT Low ER background model[163]. Figure 5.9 shows the data and the fitted background model with the separate components.

The simulation dataset is done by sampling the number of events found by the fit from the theoretical energy spectrum of each component up to 140 keV. ^{214}Pb and ^{85}Kr are taken from [164], solar ν and ^{133}Xe from [165], ^{124}Xe from [166], ^{136}Xe from [167], and the material background is a flat spectrum. The number of events generated equals a 2500 tonne-year exposure, and events are randomly distributed throughout the TPC. The resulting reconstructed energy depositions from the Monte Carlo simulation are presented in Figure 5.10 (depicted in red) alongside the SR0 background model (displayed in blue) and the data. The goodness-of-fit, quantified by the χ^2/dof value, is determined to be 0.6. This observation indicates a satisfactory agreement between the simulation and the experimental data, providing confidence in the simulation's ability to reproduce the data accurately.

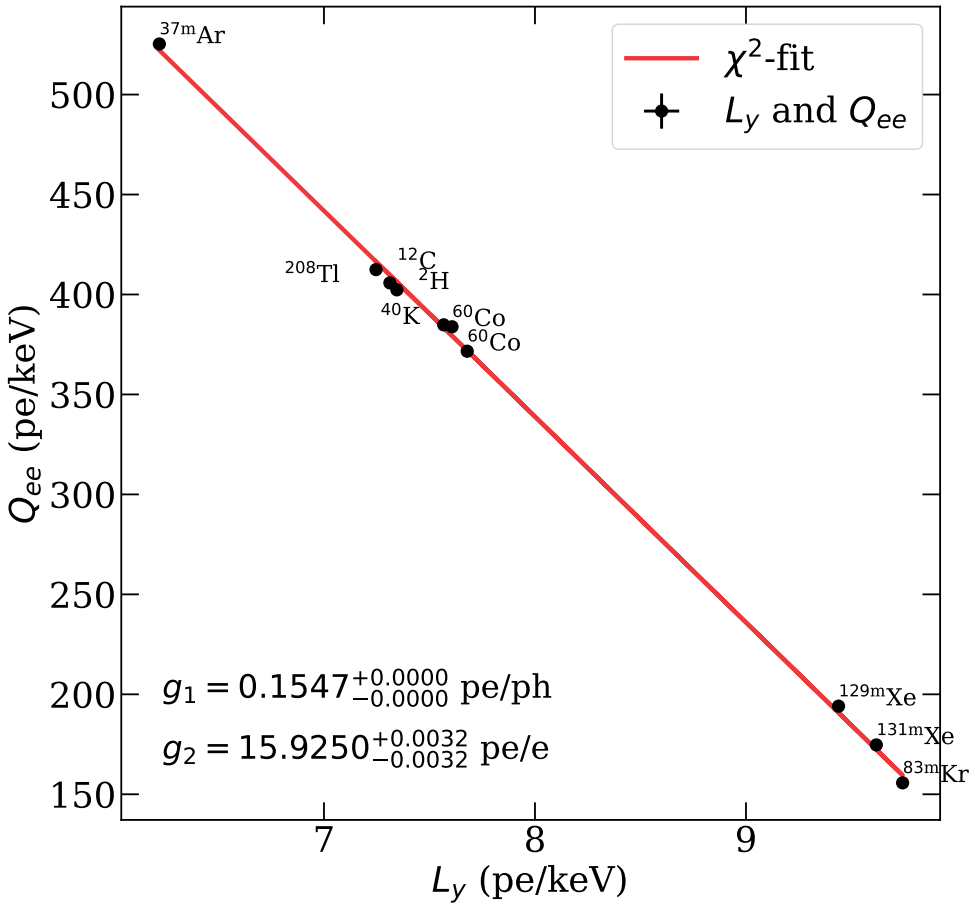

Figure 5.8 Doke plot illustrating the relationship between light yield and charge yield for monoenergetic gamma-ray lines. The data points correspond to gamma-ray lines emitted by ^{83m}Kr, ^{131m}Xe, ^{60}Co, ^{208}Tl, ^{40}K, and ^{2}H. The linear fit represents the relationship between the two yields. The fitted values of g_1 (0.1547) and g_2 (15.92) are slightly below the configured values in WFSim of g_1 (0.155) and g_2 (16.7).

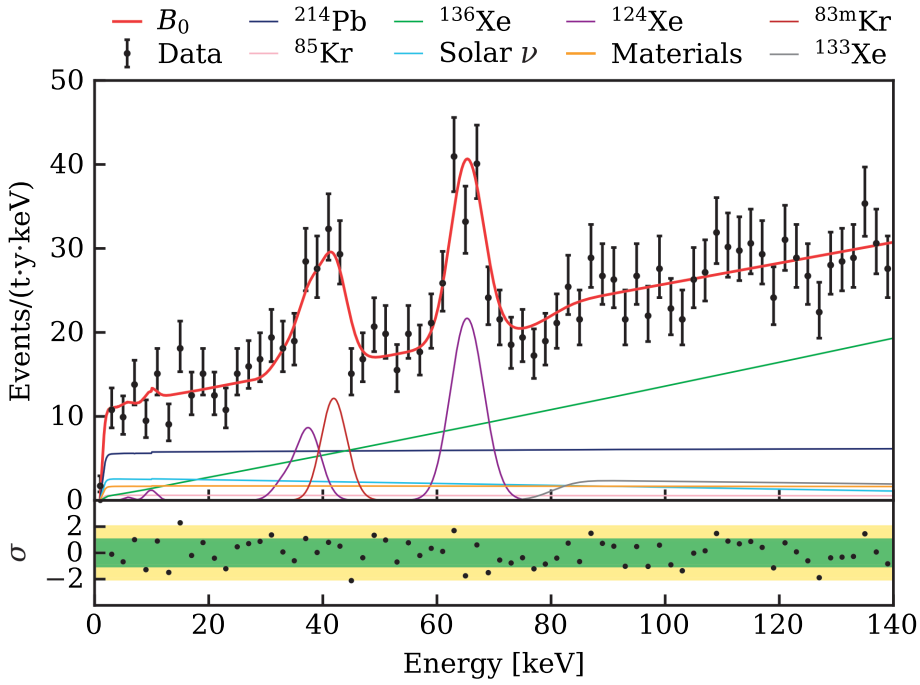

Figure 5.9 Fit to SR0 data using the background model B_0. The fit result of B_0 is the red line. Colored lines show the contributions of all components of the background model. From [163]

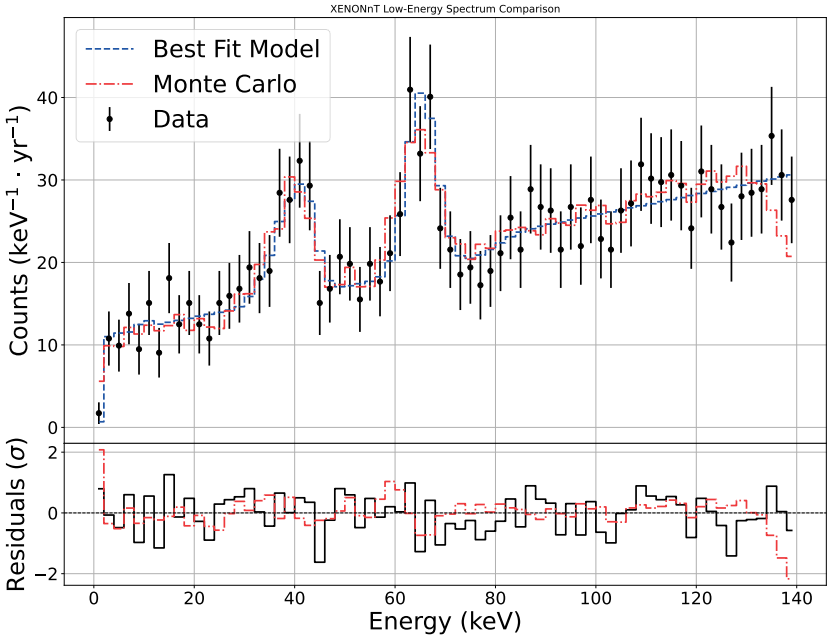

Figure 5.10 The figure compares the observed data, a Monte Carlo simulation, and the best-fit model to the data for the low-energy spectrum in XENONnT. The top plot displays the normalized data with uncertainties, the Monte Carlo simulation, and the best-fit model. The residuals, representing the differences between the data and Monte Carlo, are shown in the bottom plot. The $\chi^2/\text{dof} = 0.66$ suggest a good fit of the best-fit model to the experimental data. Counts are normalized per tonne year exposure per keV. The error bars on the data points are statistical.

5.5 Conclusion

In conclusion, the XENONnT Monte Carlo framework is for simulating particle interactions within the detector volume. It consists of three separate packages, GEANT4, EPIX, and WFSim, each responsible for a specific function, and follows a series of steps to generate the desired output. The entire framework is contained within a CVMFS container, making it easy to reproduce simulations.

To validate WFSim, we simulated monoenergetic gamma-ray lines of various isotopes and used them to calculate the doke plot. The doke plot illustrates the relationship between light yield and charge yield, and it is crucial input for accurately simulating the detector response. From the doke plot, we derived the values of g_1 and g_2. Although the fitted values of g_1 and g_2 were slightly below the configured values in WFSim, the overall agreement demonstrates the reliability of the simulation results.

In addition to the doke plot, we validated the simulation by simulating the Low Energy Recoil (Low ER) background spectrum and comparing it to the observed data. The simulation dataset is done by sampling the number of events found by the fit from the theoretical energy spectrum of each component up to 140 keV. The resulting reconstructed energy depositions from the Monte Carlo simulation are in good agreement with the observed data, indicating the reliability of WFSim in simulating the Low ER background spectrum.

This validation of WFSim provides confidence in its ability to simulate particle interactions in a detector accurately.

6

Radon induced background

Since the XENONnT experiment aims to measure rare events, $\mathcal{O}$ (1) per year, it is crucial to limit other interactions to a lower rate than the expected signal. We first must determine what can produce events within the detector to achieve this. Background events happen in the TPC in the liquid xenon (LXe) but originate from sources other than DM. Background NR events cannot be distinguished from a WIMP event when undergoing only a single scatter inside the TPC. These irreducible backgrounds will limit the ultimate sensitivity of a dark matter search. Backgrounds interacting as an NR are solar neutrinos undergoing coherent neutrino-nucleus scattering and radiogenic and muon spallation-induced neutrons. Electronic recoils are produced by electrons, gamma rays, and elastically scattering neutrinos on the electron shell of xenon and can be distinguished from an NR event by their S1/S2 ratio. A complete background model must contain all sources to deal with all backgrounds. This chapter consists of two parts. First, we start with the theory model of β-decay, as this is the main component of the background. Then, we describe the origin of the background sources and the Monte Carlo expectations, focusing on the low-energy part of the energy spectrum. In the second part, we discuss the analysis of ^{222}Rn chain events in the first Science Run of XENONnT (SR0). We will determine the rate of the various alpha decays in the ^{222}Rn and use this to infer the concentration of ^{214}Pb.

6.1 Beta decay spectra

The dominant background in LXe experiments comes from the direct to groundstate β decay of ^{214}Pb. Nuclear β decay is the process mediated by the weak interaction where the atomic number Z of the nucleus changes by one, while the total number of nucleons stays the same. The atomic number

increases in β^- decay and decreases for β^+ and electron capture. The nuclear reactions can be described as:

$$ {}^{A}_{Z}X \rightarrow {}^{A}_{Z+1}\,Y + e^- + \bar{\nu}_e \,(\beta^-\text{decay}), \tag{6.1} $$

$$ {}^{A}_{Z}X \rightarrow {}^{A}_{Z-1}\,Y + e^+ + \nu_e \,(\beta^+\text{decay}), \tag{6.2} $$

$$ {}^{A}_{Z}X + e^- \rightarrow {}^{A}_{Z-1}\,Y + \nu_e \,(\text{electroncapture}). \tag{6.3} $$

The energy distribution of emitted β particle depends on the weak interaction transition, and the atomic and nuclear structure of both the initial and final states. β decays are grouped based on the nuclear angular momentum and the spin-parity values of the initial and final states[168]. The change in nuclear angular momentum is called the *order* (K) of the decay.

The order of the decay is used to further classify different types of beta decay, with different selection rules for the angular momentum, and spin. These are:

- *Superallowed* decays. Superallowed decays are also referred to as Fermi decays. In this case, the order of the tranistion is 0, and
- *Allowed*
- *Forbidden*

Decays in which the maximum change in angular momentum Δ J = 1 and there is no change in parity between the initial and final state ($\Delta\pi = \pi_i\pi_j$=1) are *allowed* decays. For these decays, the electron and neutrino are both emitted with no orbital angular momentum, and the change in nuclear angular momentum is either zero or one.

Decays, where one or both of the emitted particles do carry angular momentum, are *forbidden* decays. Forbidden decays are further divided in unique and non-unique decays. A decay is unique if the change in parity and angular momentum satisfy the following relation:

$$ (-1)^{\Delta J}\Delta\pi = -1, \tag{6.4} $$

in which ΔJ $\geq$2.

For non-unique decays the change in parity and angular momentum follow:

$$ (-1)^{\Delta J}\Delta\pi = +1. \tag{6.5} $$

Allowed and forbidden unique transitions can be calculated without involving the initial and final nuclear state[169]. Non unique decays have strong dependence on the nuclear initial and final state.

The different classes of β-decay with the changes in parity, angular momentum, and order are listed in Table 6.1.

Transition	L	ΔI	$\Delta\pi$
Fermi (Superallowed)	0	0	0
Gamow-Teller (Allowed)	0	0,1	0
First forbidden	1	0,1,2	1
Second forbidden	2	1,2,3	0
Third forbidden	3	2,3,4	1
Fourth forbidden	4	3,4,5	0

Table 6.1 Change in angular momentum and parity for unique (top) and non-unique (bottom) β-decays of order K

6.1.1 Beta energy spectrum

Due to the three-body nature of β decay, the emitted electron, neutrino, and daughter nucleus have continuous energy spectra. The spectra depend on the decay being allowed, forbidden, and unique. BetaShape[169] is a commonly used program for calculating the emission probability of an electron per electron energy. It is based on the Behrens and Buhring formalism[170]:

$$\frac{dN}{dW} \simeq pWq^2F(Z,W)C(W)S(Z,W)R(Z,W), \tag{6.6}$$

The terms in this equation are:

- Z the atomic number of the daughter nucleus.
- W the total energy of the emitted electron.
- F(Z, W) is the Fermi function, to correct for the Coulomb interaction between the daughter nucleus and the electron. The Fermi function is calculated from the Coulomb amplitudes α_k of the relativistic electron wave functions, by numerically solving the Dirac equation with a uniform spherical charge[171].
- C(W) is the shape factor, describing the probability of the emitted beta particle to have a particular value of W. The complexity of the shape factor depends on the nature of the specific decay. For allowed and forbidden unique transitions it depends on the spin and parity of the initial and final states. For forbidden non-unique decays the nuclear matrix elements need to be taken into account. As this is a complicated calculated which needs to be done per isotope, this is typically not done and approximated by treating the decay as forbidden unique of the same order.

- R(Z, W) is to account for radiative corrections due to the energy loss of the electrons by moving through the electromagnetic field of the nucleus by internal bremsstrahlung and virtual photons[172].

- The final term, S(W, Z), is the screening correction. As the emitted β particle moves away from the daughter nucleus, the electron cloud will screen the amount of nuclear charge seen by the emitted particle. Two different approaches are included in BetaShape. The most commonly used method is by Rose[173], where a Thomas-Fermi potential V_0, dependent on the atomic number of the daughter nucleus, is subtracted from the total energy W of the emitted electron. A downside of this approach is the correction is only applied for $W \geq V_0$, which introduces a discontinuity in the energy spectrum. An alternative formulation is from Buhring, where Salvat's screened potentials[174].

The atomic exchange effect, which enhances the probability of the emitted electron in one of the electron shells, is not included to ensure fast calculations.

The effect of nuclear structure on the beta spectrum shape of the first forbidden non-unique decays is shown in Figure 6.1. This shows the beta spectrum of ^{207}Tl(1/2) $\rightarrow$ ^{207}Pb (top), ^{210}Bi $\rightarrow$ ^{210}Po (center) and ^{214}Bi $\rightarrow$ ^{214}Po (Bottom). The dependence on the nuclear structure is shown by the different colors, showing the spectrum for different values of the ratio of the weak couplings $\frac{g_A}{g_V}$. ^{210}Bi decay shows an especially strong dependence on this value. The method used to calculate these spectra is different from the one described above. The details are out of scope for this work and can be found in [175]. It should be pointed out that experimental results of the shape of ^{214}Bi $\rightarrow$^{214}Po favor the theory prediction from Betashape [176].

When higher precision at low energy is required, as for DM searches, the treatment of non-unique decays as unique decays is invalid. For this the exchange, and nuclear structure effects, and a more precise treatment of screening are required.[165][164]. The exchange effect occurs when the β-particle is emitted with the same energy as one of the atomic orbitals of the daughter nucleus. The electron previously occupying the atomic orbitals is emitted from the atom. This correction is taken into account by adding a correction factor to 6.6:

$$\frac{\mathrm{dN}}{\mathrm{d}W} \rightarrow \frac{\mathrm{dN}}{\mathrm{d}W} \times (1 + \eta_{ex}^{T}). \tag{6.7}$$

with η_{ex}^{T} the exchange correction, which depends on the electron wavefunctions of both the bound and continuum states of the daughter nucleus.

Lastly, radiative corrections need to be taken into account with higher precision. The details of these calculations are out of scope for this work and

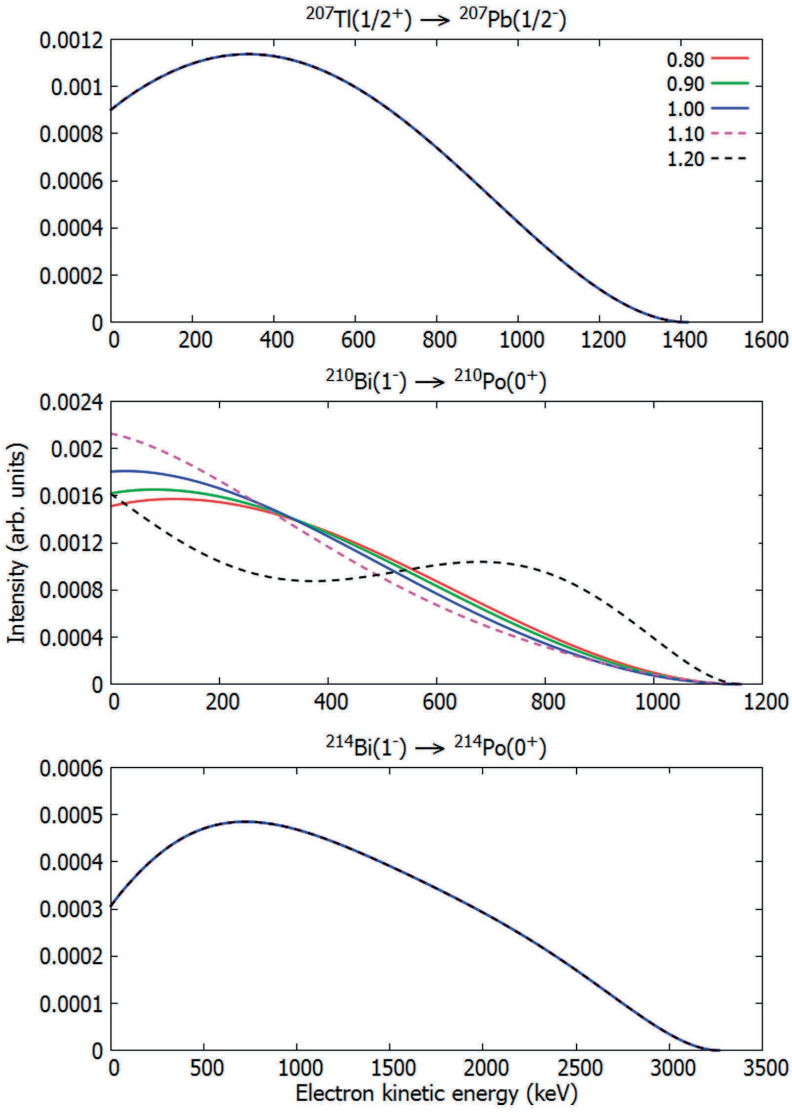

Figure 6.1 Normalized β spectrum for first forbidden non-unique ground-state-to-ground-state beta decays of ^{207}Tl, ^{210}Bi and ^{214}Bi. Colors indicate different values for the ration $\frac{g_a}{g_v}$. The spectrum of ^{210}Bi shows a strong dependence on the value of this ratio, while ^{207}Tl and ^{214}Bi are not affected. From [175].

can be found in [164]. As the above-described formalism requires separate calculations for every isotope, it has only been applied to three isotopes: ^{214}Pb, ^{212}pb, and ^{85}Kr. The differences between this calculation and the original one are shown in Figure 6.2

6.2 Backgrounds

For a low-energy ER rare-event search, it is crucial to understand background events from gamma-rays and βs in detail. These sources are classified as being either intrinsic or extrinsic.

- Intrinsic background sources are radioactive contaminants dissolved in the LXe. For the analysis presented in this thesis, two background sources are of particular importance: the beta-emitting ^{214}Pb and ^{85}Kr. ^{85}Kr (τ=10.76 yr, Q=687 keV)[177] is a noble gas soluble inside liquid xenon and therefore homogeneously distributed. ^{85}Kr is already present in the LXe as contamination. ^{214}Pb (τ=26.9 min, Q=1019 keV)[177] is not necessarily homogeneously distributed and produced by the decay of ^{222}Rn emanating from parts of the detector in contact with the xenon.

- Extrinsic sources emit particles outside the active detector volume and penetrate the LXe. These are radiogenic neutrons and muons, which can effectively be eliminated using the TPC's neutron and muon veto detectors. Neutrinos, originating from the atmosphere, sun, or supernovae, are also part of this background. When a neutrino scatters with the electronic shell of a xenon atom, it produces an ER signal, while if it undergoes coherent elastic neutrino-nucleus scattering (CEνNS), it will produce an NR background. Other extrinsic sources are radioactive isotopes outside the active detector volume or in the detector material whose radioactive decay products produce a signal in the LXe. These are either part of the primordial ^{238}U, ^{232}Th, or ^{40}K isotopes and decay products, or are radioactive isotopes produced in interaction with cosmic rays showers such as ^{60}Co, and ^{137}Cs produced by the spontaneous fission of ^{238}U. A more detailed discussion of the signals induced by these backgrounds will follow in section 6.3.

Material screening Before material was selected to be used in XENONnT, it had to be screened for contamination of different radioactive isotopes. Germanium detectors measured the contamination of ^{40}K, ^{60}Co, ^{137}Cs, ^{228}Th and the ^{238}U chain. A high-resolution Inductively Coupled Plasma Mass Spectrometry (ICP-MS)[178] was used to measure the primordial nuclides, the first part of

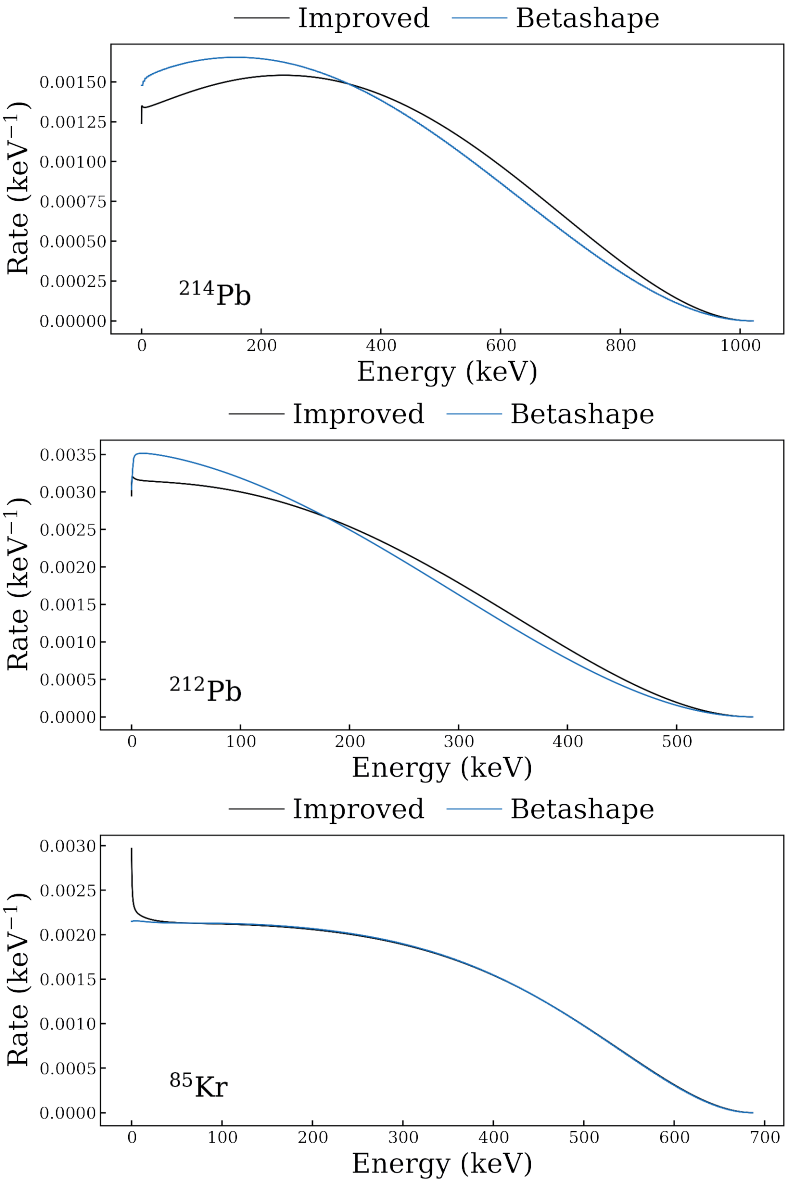

Figure 6.2 β decay spectrum for ^{214}Pb (top), ^{212}Pb (center), and ^{85}Kr (bottom) from betashape (blue) and [164] (black). Spectra are normalized over the entire energy range. The improved calculations show a decrease in the relative rate at low energy, with an increase at higher energy for ^{214}Pb and ^{212}Pb. The spectrum of ^{85}Kr is largely unaffected.

Component	Mass	Activity [mBq/kg]							
	[kg]	^{238}U	^{235}U	^{226}Ra	^{232}Th	^{228}Th	^{60}Co	^{40}K	^{137}Cs
Cryostat vessels	1120	3.2 (9)	0.37 (13)	0.37 (5)	0.29 (7)	0.45 (5)	2.5 (5)	2.1 (3)	$<$ 0.41
Cryostat flanges	730	1.4 (4)	0.06 (2)	$<$ 4	0.21 (6)	4.5 (6)	14.1 (9)	$<$ 5.6	$<$ 1.5
Bell and electrodes	190	3.2 (7)	0.57 (10)	0.62 (10)	0.36 (14)	0.46 (9)	0.78 (11)	1.6 (6)	$<$ 0.17
PTFE	128	0.12 (5)	$<$ 0.06	0.10 (2)	0.11 (5)	$<$ 0.06	$<$ 0.053	2.4 (3)	$<$ 0.038
Copper	355	$<$ 0.69	$<$ 0.28	0.033 (5)	$<$ 0.027	$<$ 0.023	0.11 (2)	$<$ 0.29	$<$ 0.016
PMTs and bases	98	53 (15)	2.2 (7)	4.6 (10)	3.5 (12)	4.2 (8)	7.1 (9)	73 (18)	0.9 (3)

Table 6.2 Table of radioactive contamination levels of main detector components in XENONnT, as measured in [179]. The contribution to the ER background is calculated by simulating every element separately. All other detector components (support structure, NV tank, etc.) contribute less than 4% to the total background rate. From [117]

^{238}U chain and ^{228}Th. As radon constitutes the most important background source in XENONnT, the surfaces of many materials were screened for radon emanation. The results are summarized in Table 6.2 and Figure 6.3, and a more detailed description of the methods and results can be found in [179].

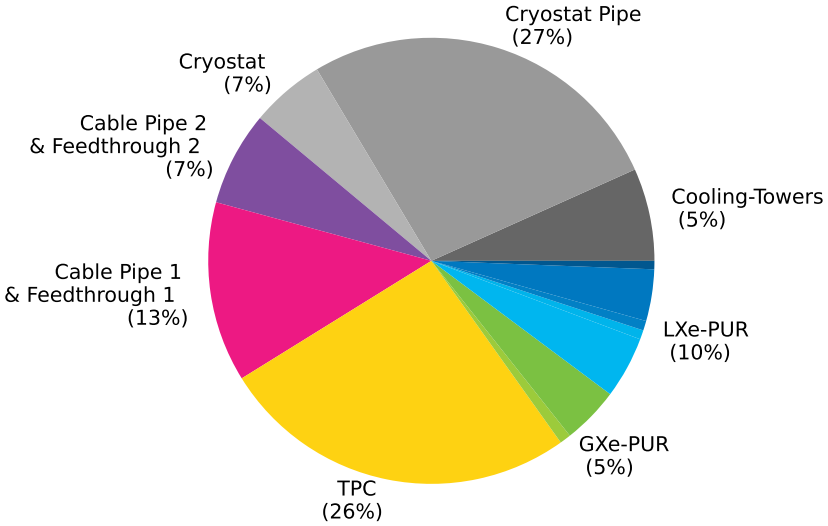

Figure 6.3 Pie chart of all contributing subsystems to the ^{222}Rn emanation in XENONnT. The percentages correspond to the central values listed in Table 6.2.

6.3 Low energy recoil spectrum

Monte Carlo simulations were done to estimate the observed background energy spectrum. For each isotope identified, 10^9 events were simulated, as well as 10^7 neutron events. The energy is Gaussian smeared with the resolution of XENON1T[180], as XENONnT was not constructed at the time. We select only single scattering events, as DM particles do not undergo multiple scatters in XENONnT. The energy region of interest (ROI) for the dark matter search is between 1 and 13 keV for NR and 5 to 50 keV for ER. Figures 6.4 and 6.6 shows the Monte Carlo energy spectrum of the ER and NR background in this energy range in the 4t inner volume. The high density ($\sim$ 3kg/l) and atomic number (Z=54) of LXe make it very efficient in stopping charged particles and radiation from penetrating the detector, so-called *self-shielding*. Due to this effect, most of the background events will be close to the edges of the TPC. The volume of the TPC, the *fiducial volume*, used for the dark matter searches, is chosen in such a way as to maximize the signal-to-background ratio while minimizing the contribution of the background. Of the material background, ^{60}Co is the largest contributor to the ER background. Below, we will describe the different components in more detail.

6.3.1 Electronic recoils

The energy spectrum of ERs in the DM region of interest is shown in Figure 6.4.

Materials Radioactive decay in the detector components can produce gamma rays. A gamma ray will contribute to the low energy background if it undergoes a single Compton scatter in the active LXe volume before escaping the detector. In the ROI, the spectrum is flat with a differential rate of 2.1 (keV t y)$^{-1}$. The most significant contributors to the total material background are the PMTs with 51% and the stainless steel cryostat vessels with 41%. The remaining 8% comes from the stainless steel bell, electrodes, PTFE, and copper [117][179].

Radon Radon is a noble gas without any stable isotopes. It is produced continuously by the alpha decay of ^{226}Ra and ^{228}Th isotopes. ^{226}Ra is part of the primordial ^{238}U and ^{228}Th is part of the ^{232}Th chain. These isotopes have extremely long half-lives, 10^9 year for ^{238}U and 10^{10} year for ^{232}Th, and trace amounts of these isotopes are mixed in all materials found on Earth. Since radon is chemically inert and in gas form at room conditions, it can emanate from materials when it is produced instead of staying trapped like its progenitors. Depending on the material the radon emanates from, this is either

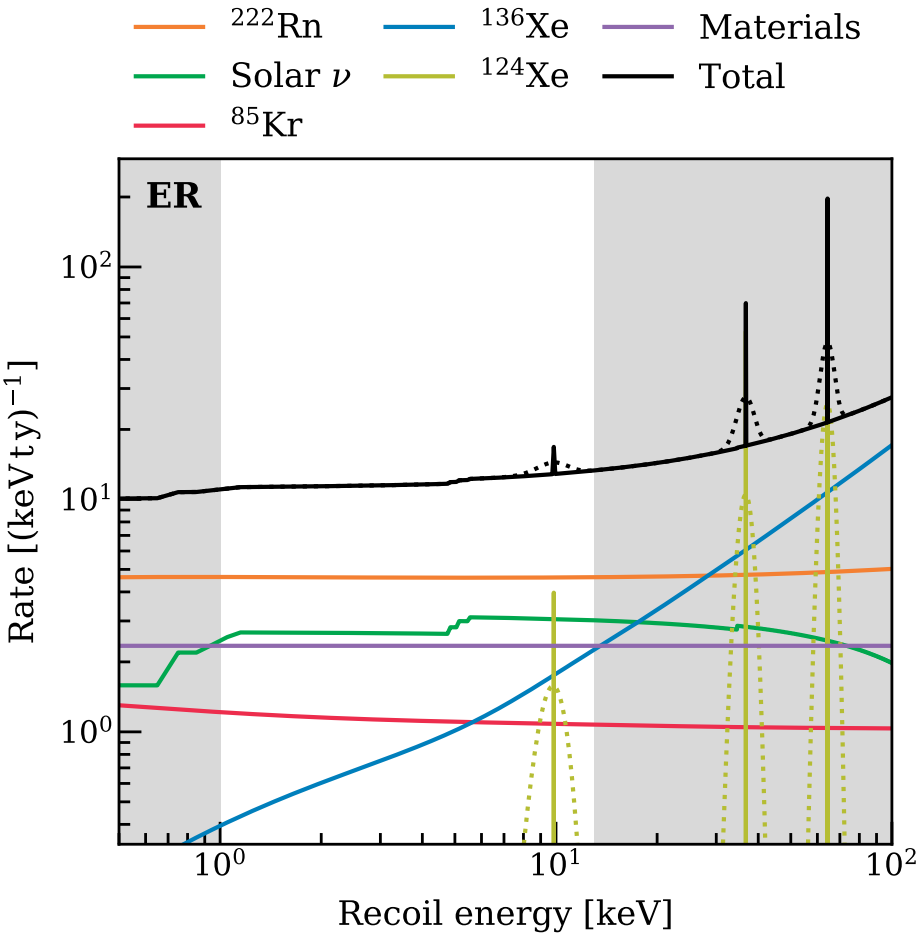

Figure 6.4 Expected energy spectra of ER background events in the 4 t fiducial volume of XENONnT. The unshaded region corresponds to the ER energy region relevant for DM search (1 - 13 keV). The dominant contribution comes from the direct-to-groundstate beta decay of ^{214}Pb of the ^{222}Rn chain. Other components are solar neutrinos, double-beta decay of ^{136}Xe (blue), double-electron capture decay of ^{124}Xe (brown), detector components (purple) and ^{85}Kr (red). The spectrum is smeared with the energy resolution of XENON1T[180] in dashed lines. From [117]

driven by diffusion, nuclear recoil energy from alpha decay, or both. Detector parts in contact with the LXe continuously emanate ^{222}Rn into the LXe. Since its half-life of 3.8 days is relatively long with respect to the circulation time of the LXe, ^{222}Rn isotopes will be homogeneously distributed throughout the LXe. The decay chain of ^{222}Rn is shown in Figure 6.5. Most of the decays in this chain are alpha decays with Q-values above 5 MeV. This is far above the energy region of interest for the dark matter search and can easily be tagged as background events. However, ^{214}Pb is a beta emitter that can decay directly to the ground state of ^{214}Bi in 10.9% of the decays with a Q-value of 1.02 MeV. The energy of the electron emitted during beta decay is continuous up to the Q-value, as illustrated in Figure 6.2. This decay forms the most prominent contribution to the low-energy spectrum. In Figure 6.4, a concentration of ^{222}Rn is 1 μBq/kgis assumed. The other beta decay in this chain, from ^{214}Bi, does not contribute to the background as it can easily be identified by the subsequent alpha decay of ^{214}Po. The expected background rate is 5.5 (keV t y)$^{-1}$ in the ROI. Similar to ^{222}Rn, ^{220}Rn also emanates from detector materials as part of the ^{232}Th chain. For this isotope, the most relevant contribution would come from ^{212}Pb, decaying through beta decay with a Q-value of 569.9 keV[177]. XENON1T measured the relative concentration of ^{220}Rn with respect to ^{222}Rn to be $\sim$ 0.3 %. Therefore, the contributions of ^{220}Rn are considered negligible and are ignored in further analysis. Due to the importance of the radon contribution to the background, we will discuss this in more detail in section 6.4.

Krypton Xenon is extracted from the atmosphere and contains a small amount of krypton. This krypton contains trace amounts of ^{85}Kr, which is mostly emitted by atmospheric nuclear weapons testing and nuclear fuel reprocessing plants. The activity of krypton was estimated to be 5500 PBq globally in 2009[182]. ^{85}Kr is a beta emitter with a half-life of 10.76 years with a Q-value of 687 keV. This contributes to the low energy spectrum shown in red in Figure 6.4. For this, a target concentration of 0.1 ppt $^{\text{nat}}$Kr/Xe is assumed to be reached. In 2019 the xenon inventory of XENONnT was distilled through a krypton distillation column. This column will also be used during operation for online distillation and has been shown to reach levels of $^{\text{nat}}$Kr/Xe < 50 ppq.

Xenon Natural Xenon consists of seven stable and two unstable, long-lived isotopes. These isotopes are listed in Table 6.3. The most important is ^{136}X with a natural abundance of 8.9% and a half-life of 2.17×10^{21} year[183], decaying through double beta decay with a Q-value of 2457 keV. The yield is

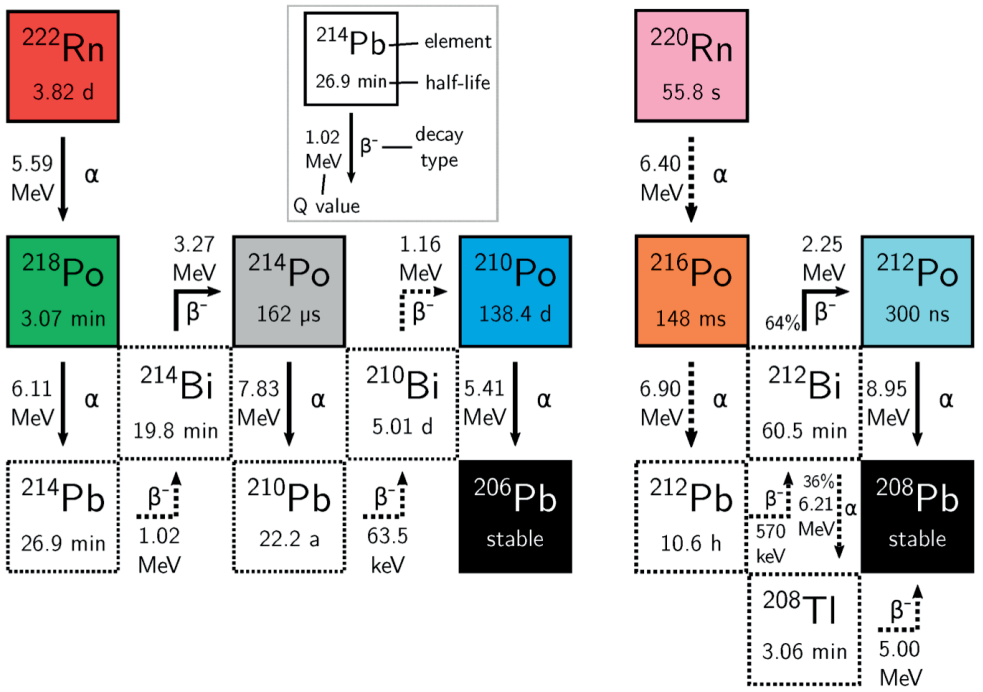

Figure 6.5 Illustration of the ^{222}Rn (Radon) and ^{220}Rn (thoron) decay chains (ignoring isotopes with a branching ratio $< 0.1\%$). The isotope color coding is kept throughout this chapter. All half-lives, branching ratios, and Q values are taken from[177]. From [181].

an average rate of 1.3 (keV t y)$^{-1}$ in the ROI.

Isotope	abundance	half-life
^{124}Xe	0.095%	1.8×10^{22}[183]
^{126}Xe	0.089%	stable
^{128}Xe	1.910%	stable
^{129}Xe	26.401%	stable
^{130}Xe	4.071%	stable
^{131}Xe	21.232%	stable
^{132}Xe	26.909%	stable
^{134}Xe	10.436	stable
^{136}Xe	8.857%	2.1×10^{21}[184]

Table 6.3 Natural occurring xenon isotopes

The other relevant isotope is ^{124}Xe decaying through double electron capture. The energy deposition of this decay is 9.8 keV if both captured electrons come from the L shell, which has a branching ratio of 1.7%. With the half-life measured to be $1{,}8 \times 10^{22}$ year and isotopic abundance of 0.099%, the estimated rate is 3.5(t y)$^{-1}$ at 9.8 keV.

Solar neutrinos Low energy ER signals can be caused by solar neutrinos scattering elastically off atomic electrons. The solar neutrinos are assumed to be produced in either the pp fusion process or electron capture by ^{7}Be. This accounts for 98% of the total solar neutrino flux[185]. This will be the second-largest contribution to the ER background with an expected rate of 2.8 (keV t y)$^{-1}$ in the ROI.

6.3.2 Nuclear recoils

The energy spectrum of nuclear recoils is shown in Figure 6.6.

Radiogenic neutrons Radiogenic neutrons are produced through spontaneous fission (SF) or (α, n) reactions in detector materials[117]. The Neutron Veto (NV) detector is operated around the TPC to reduce this background. NV events require a ten fold-coincidence of PMT signals and the signal to occur within 150 μs of a TPC event. The resulting tagging efficiency is $\sim$ 87%, leading to a reduction in the rate in the ROI from 0.321 (t y)$^{-1}$ to 0.041 (t y)$^{-1}$[117]. Note that this tagging efficiency is for Gd-doped water; in SR0, where the NV is operated with only pure water, the tagging efficiency is 0.68%[186]. The most significant contributions come from the SS cryostat vessel, the PMTs, and the PTFE components.

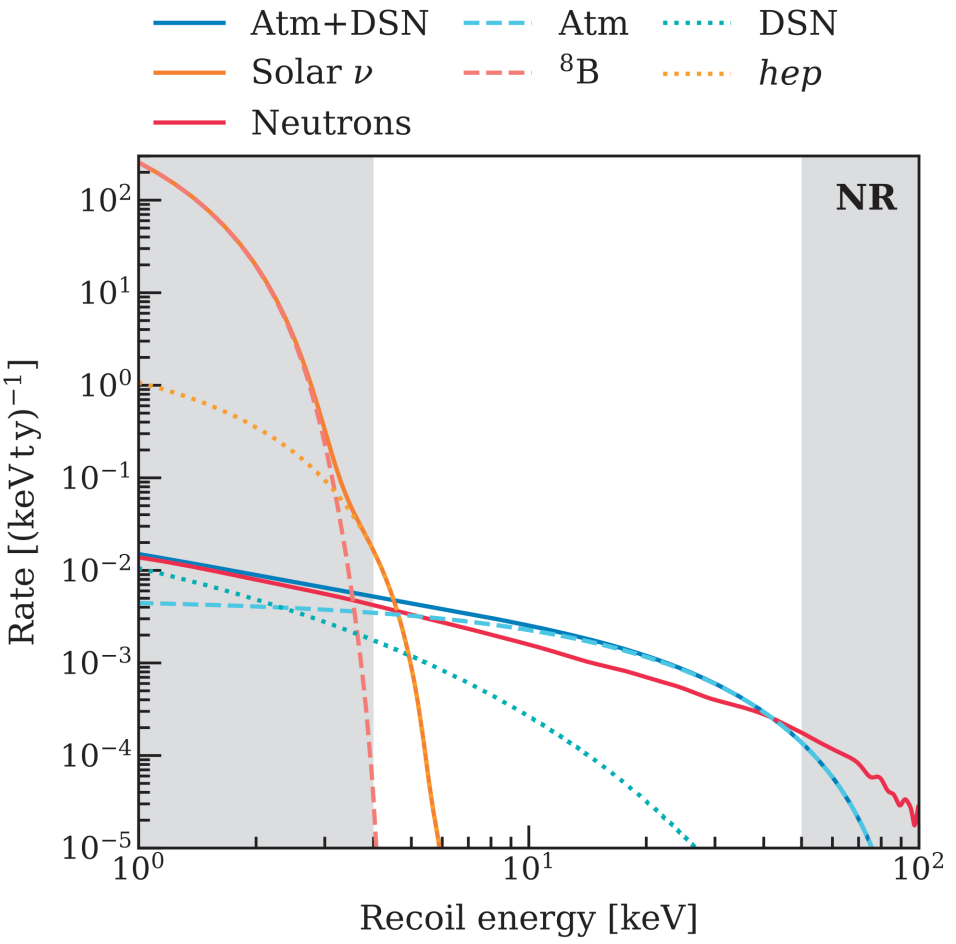

Figure 6.6 Expected energy spectra of NR background events in the 4 t fiducial volume of XENONnT. The unshaded region corresponds to the NR energy region relevant for DM search (4 - 50 keV). The contributions are from radiogenic neutrons (red) and CEνNS of solar neutrinos (orange), specifically ^{8}Be (dashed) and hep (dotted), atmospheric (dashed blue), and diffuse supernova neutrinos (dotted blue). The neutron spectrum is corrected for the expected tagging efficiency of the Neutron Veto. The spectrum is smeared with the energy resolution of XENON1T[180] in dashed lines. From [117].

Cosmogenic neutrons Cosmic ray muons are continuously produced in the atmosphere. These muons can travel through the rock and cause neutrons to be emitted by the concrete surrounding the detector. The water shield surrounding the TPC efficiently moderates such neutrons and suppresses the observed rate of cosmic-induced neutrons to $< 0.01(\mathrm{ty})^{-1}$.

CEνNS neutrinos Coherent Elastic neutrino-nucleus scattering contributes significantly to the NR background rate, especially towards the lower end of the spectrum[187][188]. These neutrinos originate from the sun, the atmosphere, and supernovae(DSN). The search for lighter WIMP masses, a few GeV/c^2, is severely limited by solar neutrinos. At the same time, atmospheric and DSN neutrinos' contributions are over a broader energy range.

Summary In Table 6.4, the background expectations for both ER and NR are summarized. The integrated rates are given going up to 200 keV, and for the energy region where the XENONnT detector is most sensitive to a 50 GeV/c^2 WIMP. The ROI goes from 1 to 13 keV in ER and 4 to 50 in NR.

Source	Rate $[(\mathrm{t\,y})^{-1}]$
ER background	
Detector radioactivity	25 ± 3
^{222}Rn	55 ± 6
^{85}Kr	13 ± 1
^{136}Xe	16 ± 2
^{124}Xe	4 ± 1
Solar neutrinos	34 ± 1
Total	148 ± 7
NR background	
Neutrons	$(4.1 \pm 2.1) \times 10^{-2}$
CEνNS (Solar ν)	$(6.3 \pm 0.3) \times 10^{-3}$
CEνNS (Atm+DSN)	$(5.4 \pm 1.1) \times 10^{-2}$
Total	$(1.0 \pm 0.2) \times 10^{-1}$

Table 6.4 Estimated integrated background event rates in the 4 t fiducial volume of XENONnT. The energy ROI in which the event rates are integrated is (1, 13) keV for ERs and (4, 50) for NRs. From [117].

With an expected number of 55 ± 6 events per tonne year, ^{214}Pb from ^{222}Rn has the most significant contribution to XENONnTs background. This chapter will be dedicated to further analysis of ^{222}Rn data.

6.4 Constraining the ^{214}Pb concentration

Since the background coming from ^{214}Pb is the dominant component of the ER background in XENONnT, it is crucial to get an accurate measurement of its rate. One method to constrain the ^{214}Pb rate is by measuring the rate of various alpha decays from the ^{222}Rn chain, to which ^{214}Pb belongs. The alternative is to fit the low-energy ER spectrum directly. We use the rate of ^{218}Po (^{214}Po) to set an upper (lower) limit on the expected rate of ^{214}Pb in the DM search data. Alpha decay events emit a very clean signal in the detector. These events have very large S1-signals of $> 10^4$ photoelectrons (pe), and there is minimal background in S1-S2 space close to the alpha event populations. There are two commonly used procedures for analyzing alpha events. These are:

Full event information We use all S1 and S2 information. With the complete event information, we use the standard data processing algorithms for position reconstruction and position-dependent signal corrections to correct for light yield variations throughout the TPC. The need for corrections is illustrated in Figure 6.7. This Figure shows the *position depend S1 light collection efficiency*(LCE), which is the fraction of photons arriving at the photocathode of the PMTs. Note that the full photon detection efficiency includes another 35% due to the quantum efficiency of the PMTs. As the LCE map is position-dependent, we need to correct variations in light collection efficiency before fitting the alpha spectrum. The position dependence arises from the variations in the path length of the photons through the LXe before arriving at one of the PMTs. The reconstructed positions of the events make estimating a fiducial mass in the analysis straightforward. As corrections are already available, we do not need custom corrections. This method has two drawbacks.

Firstly, there is a significant amount of time when the anode is switched off. There are no S2 signals in these data sets and can therefore not be used in an S1-S2 analysis. Although data taken during these periods is not considered for dark matter searches, including this data gives a better constraint on the ^{214}Pb rate.

The second drawback is related to the properties of the decays of various isotopes of interest, specifically ^{214}Po and, to a lesser extent, ^{210}Po. There are problems with the correct S1-S2 matching in the data processing software for these isotopes, which groups the largest S1 and S2 in an event.

^{214}Po has a half-life of 162 μs following the beta decay of ^{214}Bi. Alpha decays have a relatively large S1 compared to their S2; the S1 of the ^{214}Po can be matched to the S2 of the ^{214}Bi by the event reconstruction algorithm.

Further complications arise if the beta-decay of ^{214}Bi goes to an excited state of ^{214}Po instead of the ground state of ^{214}Po (branching ratio of 19%). The excited ^{214}Po decays to its ground state by emitting a possibly large number of gamma rays(>10)[189]. The algorithm matches the S1 of the ^{214}Po to the S2 of either the beta decay from ^{214}Bi or to one of the gamma rays emitted after the decay took place. This leads to a wrong position reconstruction and, thus, incorrect signal correction.

The other problematic isotope is ^{210}Po, a long-lived isotope with a half-life of 138.3 days, produced after the β-decay of ^{210}Pb with a half-life of 22.2 years. Since these half-lives are so long, ^{210}Po is not in equilibrium with the progenitor isotopes of the ^{222}Rn chain and is not mixed in the xenon but stuck to detector materials as polonium and lead are metals who stick to conductive surfaces, this process is known as *plate out*. This leads to the activity of ^{210}Po highest near the PTFE wall. Interactions close to the PTFE wall have a part of their S2 lost due to electrons sticking to the wall; this is a *charge-insensitive region*. As the largest part of the S2 from ^{210},Po is lost, the algorithm matches the S1 of ^{210}Po with the largest S2 happening at a similar time. Since the light distribution of the S2 is used for position reconstruction, ^{210}Po is reconstructed not on the position the decay happened but at the position of the S2. As ^{210}Po is not in equilibrium with ^{214}Pb, measuring the rate of this isotope is not required for this analysis.

S1 only The alternative is to use only the S1 signal. This method circumvents the issues with the anode being switched off and the incorrect S1-S2 matching for ^{214}Po and ^{210}Po.

Without the S2, we cannot use standard algorithms for position reconstruction and signal corrections. Therefore, this method requires the development of alternative ways for position reconstruction and new corrections.

In this analysis, we use the *S1-only* method. For the position reconstruction, we approximate the z-position using the *Area Fraction Top* (AFT) of the S1 signal, the fraction of light measured by the top array, and a center of gravity algorithm to reconstruct the x-y position. For the corrections, we take advantage of the known properties of the alpha decays. This method was first developed [190] for the determination of ^{222}Rn and daughter isotope concentrations in XENONnT. We apply three corrections to the data before fitting the alpha spectrum. First, we correct the AFT dependence of the S1 area (S1), cS1' . Second, we correct the AFT dependence of the reconstructed r^2_{cog} position to r^2_{c} . Finally, we correct the r^2_{c} dependence of cS1' to cS1 . The following sections will provide more details on all correction steps.

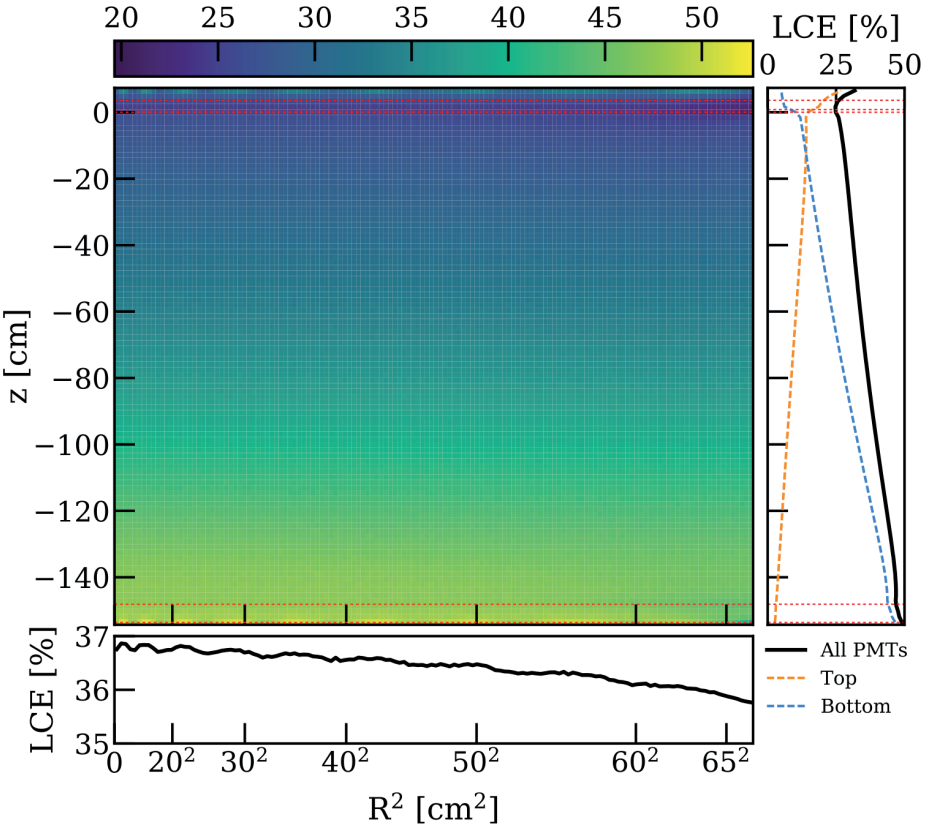

Figure 6.7 XENONnT S1 light collection efficiency (LCE) map. This map shows the position dependence of the fraction of S1 light observed inside the TPC. To fit the alpha spectrum, we correct for the spatial variations. The correction is such that the LCE is uniform throughout the TPC volume, normalized the center of the TPC.

Center of gravity position reconstruction For reconstructing the position of S1s, we cannot use the methods developed for S2 position reconstruction. These methods rely on a localized PMT hit pattern of the S2 in the top array to calculate the position. For S1s, the PMT hit pattern is much smoother over the top and bottom array. A simple method to reconstruct the position of S1s is a *Center of Gravity* (CoG) method. The x-y position of an S1 is the average of the positions of the PMTs weighted by the fraction of total light the PMT has received:

$$\begin{aligned} x_{\mathrm{s1}} &= \sum_{i}^{PMTs} \frac{S1_i * x_i}{\mathrm{S1}}, \\ y_{\mathrm{s1}} &= \sum_{i}^{PMTs} \frac{S1_i * y_i}{\mathrm{S1}}, \end{aligned} \tag{6.8}$$

with $\mathrm{S1}_i$ the signal measured by a single PMT, x_i (y_i) the x (y) position of this PMT, and S1 the total signal.

6.4.1 S1-only alpha analysis

For the S1-only analysis, the starting point is selecting all signals classified as an S1 with an area larger than 10^4 pe. The resulting S1 vs. AFT distribution is shown in Figure 6.8. The bands belonging to the alpha decays are at S1 $>$ 40 $\times 10^3$ pe and $0.15 <$ AFT < 0.6. The bands corresponding to the different isotopes are separated and have a clear AFT dependence. This shows a similar effect as the z dependence of the LCE map in Figure 6.7.

6.4.2 Area Fraction Top correction

The slanting of the lines in Figure 6.8 shows how the signal size (S1) varies as a function of depth in the TPC. The analysis is limited to AFT values between 0.15 and 0.455 to avoid events close to the cathode or anode originating from the gaseous xenon.

The AFT correction is for correcting the z-dependence of the LCE, the right panel in Figure6.7, to the value in the center of the TPC. We use the S1 signals from the ^{214}Po decay to calculate the required correction based on AFT. This is the rightmost population of events in Figure 6.8. As mentioned previously, the decay of ^{214}Po quickly, the half-life of 162 μs, follows the decay of ^{214}Bi with a half-life of 19.8 min. To select a clean sample of ^{214}Po events, we cut on the time difference to the previous S1 to be within 0.7 $\mu\mathrm{s} < dt <$ 550 μs. The lower limit on dt is to avoid selecting ^{212}Po whose half-life is 300

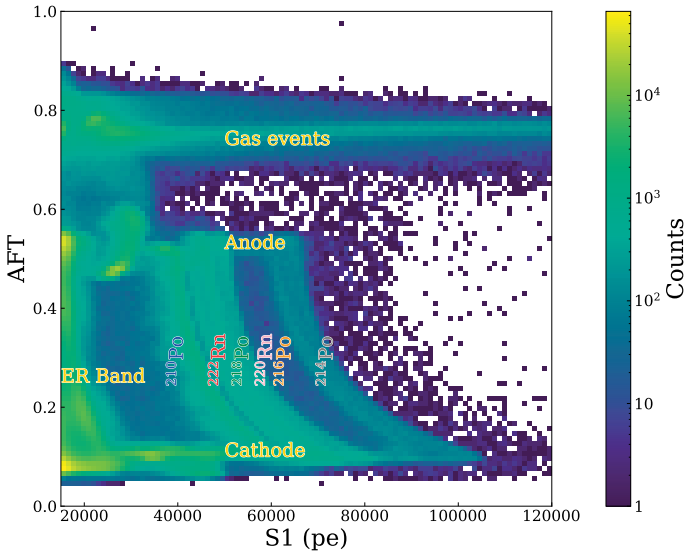

Figure 6.8 Distribution of the fraction of primary scintillation light (S1) light measured by the top array (Area Fraction Top; AFT) vs. total S1 area in photoelectrons (pe) for all S1 signals >1.8 $\times 10^4$ pe ($\sim$ 1 MeV) of all SR0 background runs. Starting above 4 $\times 10^4$ pe are six alpha lines visible from ^{210}Po, ^{222}Rn, ^{218}Po, ^{220}Rn, ^{216}Po, and ^{214}Po . The slanting of the lines to the lower S1 for higher AFT is due to the z-dependence of the LCE map shown in Figure 6.7.

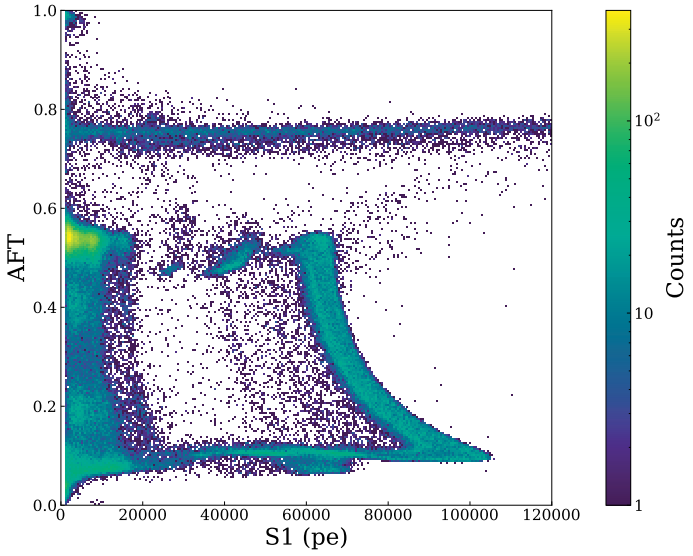

Figure 6.9 Data of Figure 6.8 with time difference cut to select ^{214}Po, while removing the other alpha decays.

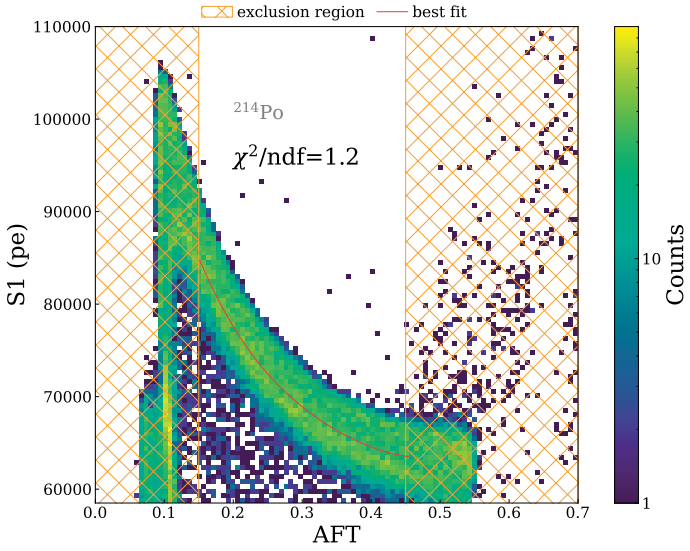

Figure 6.10 Rotated zoom in (S1 $>$ 6 $\times 10^4$) on ^{214}Po S1 events, S1 vs. AFT with time difference cut. The exclusion region is to cut away events from originating from the anode and cathode.

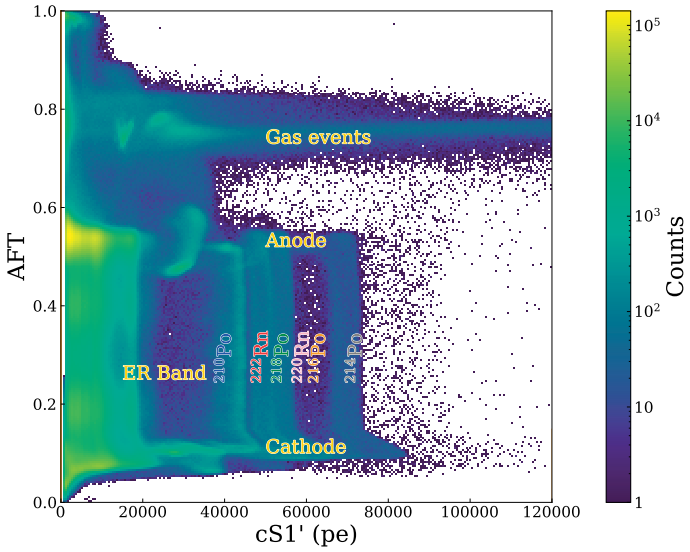

Figure 6.11 cS1' vs. AFT distribution of all S1 events in the TPC. After correcting, the alpha lines have less AFT dependence, although the lines still partially overlap.

ns. The events remaining after this selection are shown in Figure6.9. Figure 6.10 shows the finally selected ^{214}Po peaks with the S1 as a function of AFT.

The cS1' is defined as follows:

$$\mathrm{cS1}' = \mathrm{S1}\frac{p_1(AFT)}{p_1(AFT = 0.33)}, \tag{6.9}$$

with cS1' the S1 after AFT correction, AFT_{ref} the reference value AFT of 0.33, which is approximately the center of the TPC. p_1 is a second order polynomial fitted to the ^{214}Po data, shown in Figure 6.10. The resulting χ^2/ndf is 1.2.

The result of cS1' is shown in Figure6.11, in which the dashed orange line indicates the AFT bounds. The alpha lines no longer have an AFT dependence but are not separated.

6.4.3 x-y correction

The $x-y$ position reconstruction with the CoG method described in section 6.4 results in a $x-y$ position dependent on AFT. Figure 6.12 shows the relation between the r^2_{cog} reconstructed position versus AFT. The usage of CoG methods for position reconstruction has a large drawback. CoG tends to pull events inward to the center of the TPC, as there is a maximum radius from the size of the TPC. On top of that, the S1 light pattern is more homogeneously distributed over the PMTs, which will also result in the reconstructed positions closer to the center of the TPC. To correct for the AFT dependence, we use a source with a known position and correct r^2_{cog} such that these events are at the correct position. We select S1s from ^{210}Po for this. As mentioned before, due to the long half-life of both ^{210}Po (130 days) and its mother nuclei ^{210}Pb (22.2 yr), ^{210}Po is not in the LXe but stuck to the wall of the TPC and other detector materials. ^{210}Po is distributed at an r^2 of 4400 cm^2 (the PTFE wall). To select ^{210}Po, we cut on the corrected area to be $3.9 \times 10^4 < \mathrm{cS1}' < 4.4 \times 10^4$. The ^{210}Po selection is shown in Figure6.13.

The corrected position, r^2_{c} is defined as follows:

$$r^2_{\mathrm{c}} = r^2_{\mathrm{cog}}\frac{p_2(r^2_{\mathrm{cog}})}{p_2(r^2_{\mathrm{r^2=0}})}, \tag{6.10}$$

with r^2_{c} the corrected r^2_{cog} position, r^2_{cog} the r^2 value according to CoG and $\mathrm{r}^2_{\mathrm{PTFE\,wall}}$ the r^2 position of the PTFE wall. After the correction, r^2_{c} is scaled such that the mean of the ^{210}Po distribution corresponds to the r^2 of the PTFE wall. The correction function, p_2 is a fourth-order polynomial fitted with least square minimization, shown in Figure6.13. The χ^2/ndf is 3.3.

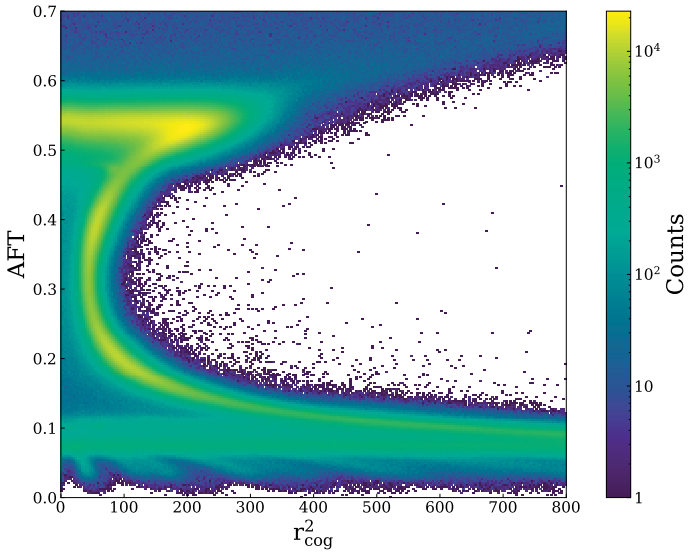

Figure 6.12 AFT vs. rr^2_{cog} distribution of S1 events. This shows the inward pull of the center of gravity method for events in the center of the TPC in z.

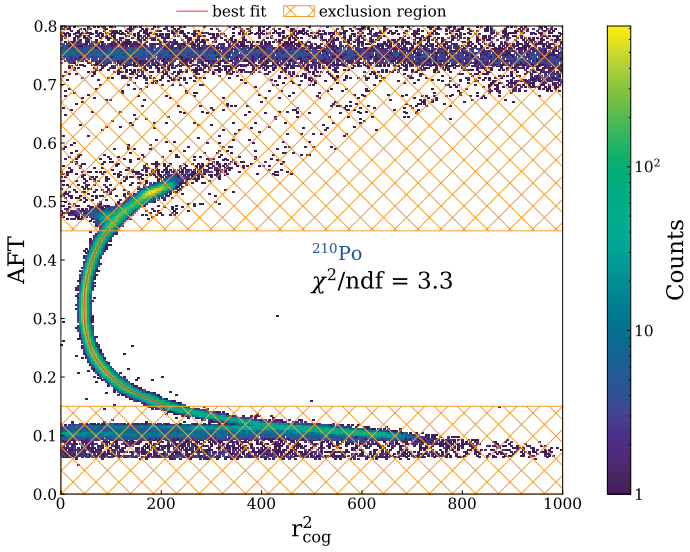

Figure 6.13 Data of Figure 6.12 with 3.9 $\times 10^4$ < cS1' < 4.4 $\times 10^4$ cut to select ^{210}Po events, located on the wall of the TPC.

The distribution of r_c^2 vs. AFT is shown in Figure 6.14. After correction, r_c^2 no longer depends on AFT, and the maximum of the r_c^2 distribution of ^{210}Po is set to a value of 4400, which is the position of the PTFE wall.

After correcting the reconstructed position, we correct the cS1' spectrum as a function of r_c^2 . The distribution of r_c^2 vs. cS1' is shown in Figure 6.15. The decrease in light yield at higher values of r_c^2 shows the same drop as in Figure 6.7 (bottom). For the correction, we select ^{214}Po, shown in Figure 6.16, which is homogeneously distributed throughout the TPC.

cS1 is defined as follows:

$$\mathrm{cS1} = \mathrm{cS1}' \frac{p_3(r_c^2)}{p_3(r_c^2 = 0)}, \tag{6.11}$$

with r_c^2 =0 the reference value at the center of the TPC. The correction function, p_3, is a third-order polynomial fitted with least square minimization, shown in Figure6.16. The χ^2/ndf is 1.9.

After correction, the cS1 spectrum as a function of r_c^2 is shown in Figure6.17, where the alpha lines are now straight for increasing r_c^2 .

6.4.4 Fiducial mass

To calculate the total mass of LXe within this volume, we map this coordinate system to the dimensions of the TPC. The relation between AFT and z is calculated using S1-S2 data. Figure 6.20 shows the distribution of AFT vs. z of S1+S2 data from July 2022, where the red line is a fit through the median values of z in slices of AFT of a third-order polynomial function. The z values corresponding to the AFT limits of $0.15 < \mathrm{AFT} < 0.445$ are $-116.8 < z < -25.4$.

To verify the bounds set on r_c^2 , we calculate the ratio between the number of ^{214}Po peaks within the selected volume and the total TPC volume in r_c^2 . As ^{214}Po is homogeneously distributed in the LXe, this fraction is the same as the fraction of xenon enclosed in the selected volume. This ratio is 0.356, making the upper bound of r_c^2 of 2700 correspond to 1326 cm^2. The total fraction enclosed in the fiducial volume for the total TPC volume is 0.22, corresponding to a mass of 1.38T LXe.

Figure 6.19 shows the r_c^2 vs. AFT distribution, with the orange lines indicating the selected fiducial volume fitting the alpha spectrum.

6.4.5 Spectral Fit

The fit is performed on the corrected area spectrum and is constrained to AFT and r_c^2 bounds listed in Table 6.5. The upper limit on r_c^2 removes ^{210}Po

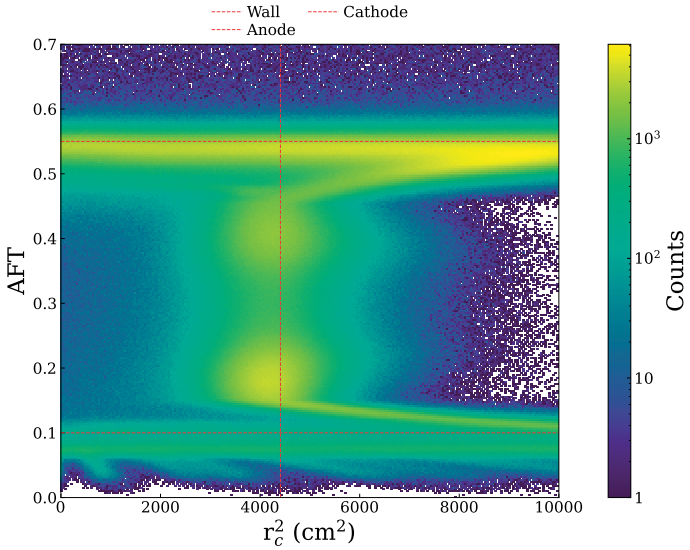

Figure 6.14 AFT vs. r_c^2 , after correction of r_{cog}^2 . The event distribution is no longer AFT-dependent. The maximum of the distribution of r_c^2 of ^{210}Po is set to 4400 cm^2, which is the position of the PTFE wall.

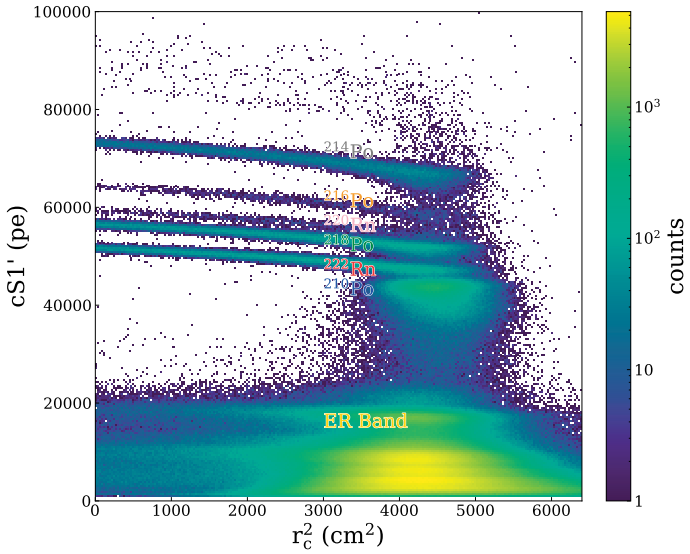

Figure 6.15 cS1' vs. r_c^2 vs. of all S1 events. The drop of the measured cS1' towards higher r_c^2 shows the decrease of the light yield at higher radii, as also shown in the LCE map (Figure 6.7).

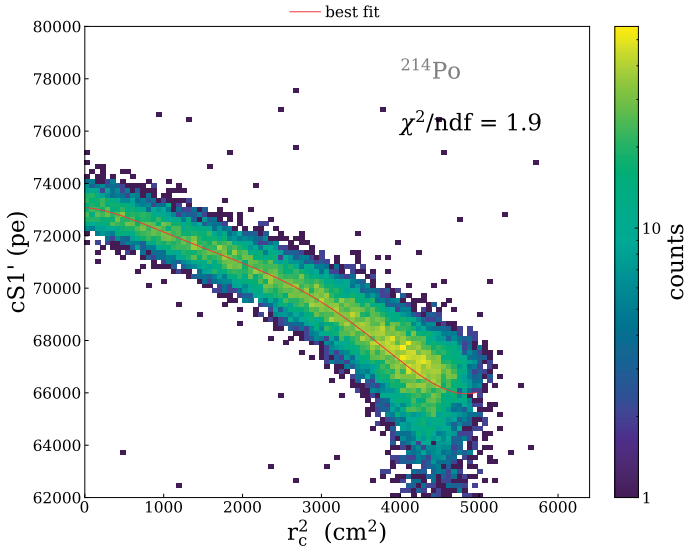

Figure 6.16 Zoom-in of ^{214}Po S1 events, used for correcting the r_c^2 dependency of cS1' . Median S1 of ^{214}Po S1 events binned in r_c^2 slices, with the third-order polynomial fit. The fit is used as input for the r_c^2 correction of cS1' .

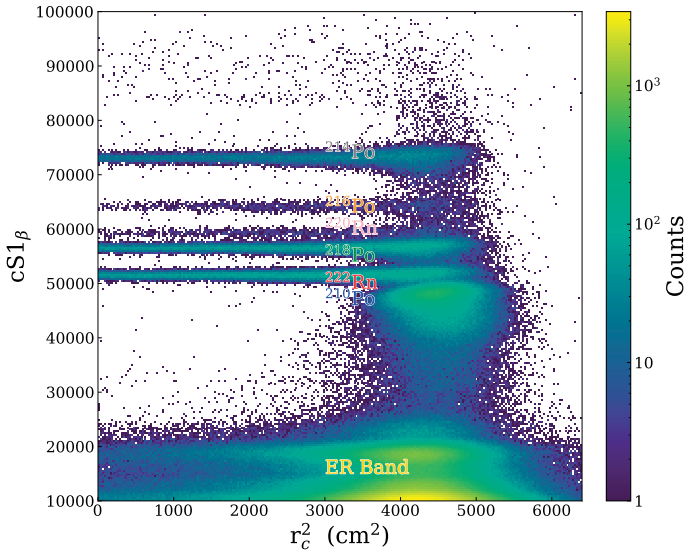

Figure 6.17 Distribution of cS1 vs r_c^2 . The alpha lines are now independent of r_c^2 ; the LCE is homogeneous for all r_c^2 .

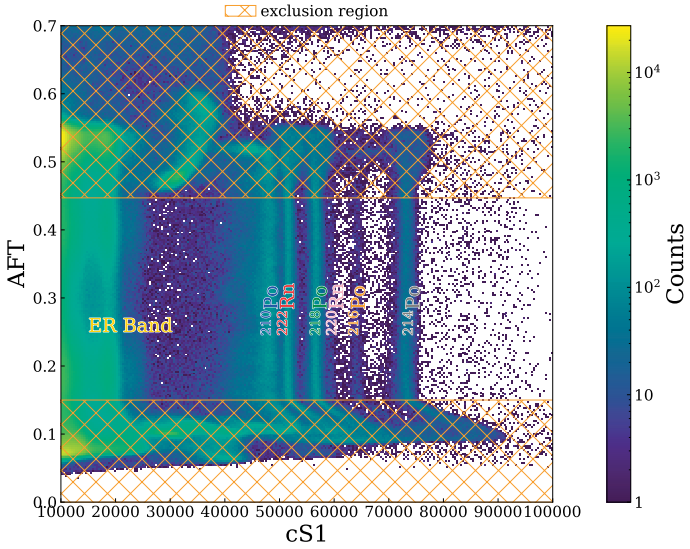

Figure 6.18 AFT vs. cS1 . The cS1 distributions of the alpha decays are independent of AFT and separated from each other with the applied corrections. The orange line indicates area fraction top bounds. The bands correspond to, from left to right, ER events, ^{210}Po, ^{222}Rn,^{218}Po,^{220}Rn,^{216}Po, and ^{214}Po.

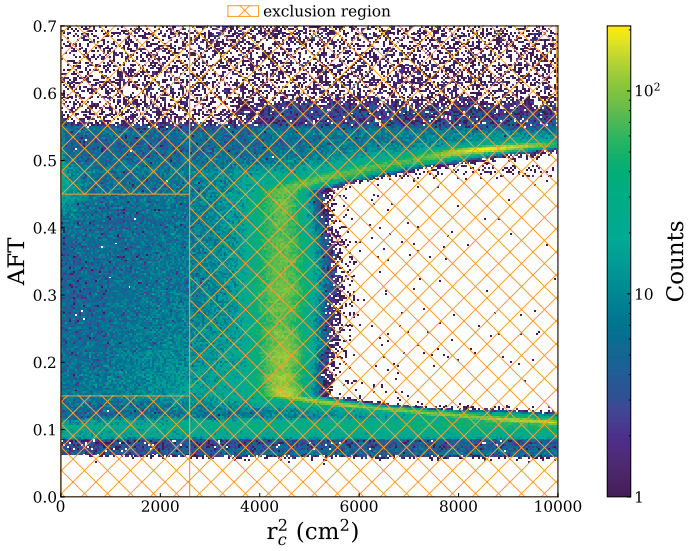

Figure 6.19 r_c^2 vs. AFT distribution for all events. The orange dashed box indicates the volume used for counting the alpha decays. The values of the bounds are listed in Table 6.5.

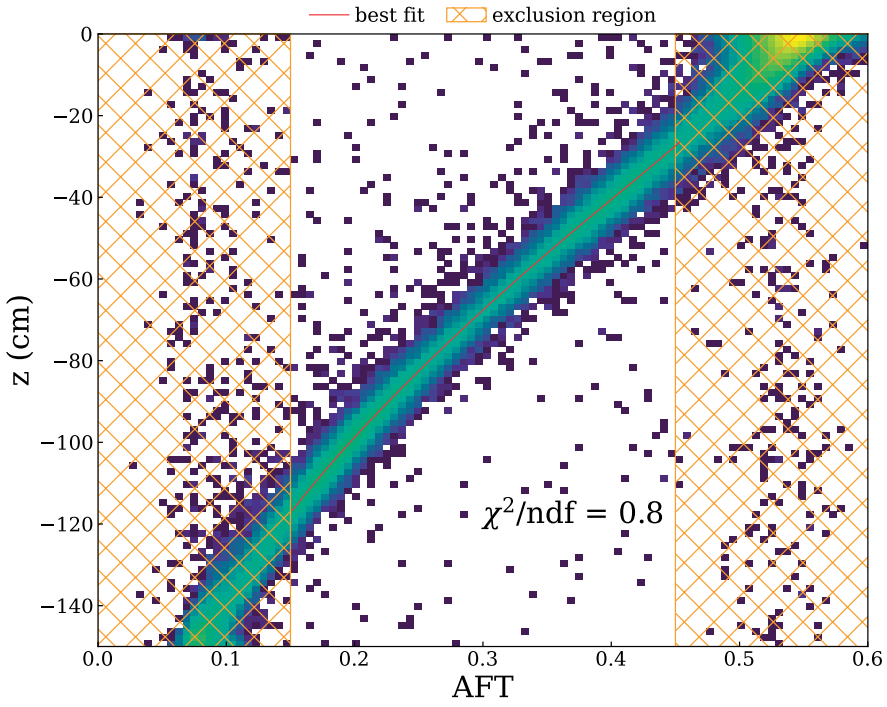

Figure 6.20 z vs. S1 AFT distribution of S1+S2 data from July 2021 shows the correlation between z and AFT. The red line is a third-order polynomial fit through the median value of z binned in AFT, used to map AFT to z.

Parameter	Lower bound	Upper bound
AFT	0.15	0.455
r_c^2	0	2700
z	-116.8 cm	-25.4 cm
r^2	0 cm^2	1326 cm^2

Table 6.5 Fiducial volume bounds used for the alpha spectrum fit. The volume is defined in AFT, and r_c^2 , z, and r^2 are the corresponding values of the bounds in the coordinate system of the TPC. The volume excludes events close to the PTFE wall, cathode, and anode. The total mass enclosed in this volume is 1.36 t.

from the spectrum, as this isotope's decay energy is close to that of ^{222}Rn, causing significant overlap between the two. Figure 6.21 shows the normalized Area spectrum. The five peaks are, in ascending order of energy, ^{222}Rn, ^{218}Po, ^{220}Rn, ^{216}Po and ^{214}Po. We fit a sum of five Gaussians to the spectrum via an unbinned minimum negative log-likelihood fit. The relative width of the Gaussians is set to be shared amongst the Gaussians except for ^{214}Po, as this is the most energetic decay. The mean and amplitudes are left as free parameters. The fit results are shown in Table 6.6.

Isotope	**Q-value** (MeV)	**Mean(μ) area** (pe)	**Width (σ)** (pe)
^{222}Rn	5.59	$(5.185 \pm 0.001) \cdot 10^4$	$(4.38 \pm 0.01) \cdot 10^2$
^{218}Po	6.12	$(5.687 \pm 0.001) \cdot 10^4$	$(4.80 \pm 0.01) \cdot 10^2$
^{220}Rn	6.4	$(5.960 \pm 0.003) \cdot 10^4$	$(5.04 \pm 0.01) \cdot 10^2$
^{216}Po	6.9	$(6.431 \pm 0.003) \cdot 10^4$	$(5.45\pm 0.01) \cdot 10^2$
^{214}Po	7.83	$(7.30 \pm 4.0) \cdot 10^4$	$(6.21 \pm 0.02) \cdot 10^2$

Table 6.6 Fit results of the S1-only alpha spectrum fit. The relative widths of ^{222}Rn, ^{218}Po, ^{220}Rn, and ^{216}Po are shared to improve fit convergence. The fitted ($\mu \pm 2\sigma$) region is used to define counting regions to measure the rate of the isotopes.

The goodness of fit is determined by binned Poisson χ^2, as the histogram has empty bins[191]. The resulting χ^2/ndf is 0.01. This low value is likely due to Gaussians not appropriately describing the LXe response to alpha decays. A more appropriate model is using skewed Gaussians. As the only interest of the fit are the means and widths, the use of Gaussians is correct, as skewed Gaussians will result in a better fit of the distribution's tails. The corrections introduce additional systematic uncertainty, which can lead to deviations of a Gaussian shape.

6.4.6 Rate determination

For determining the evolution of the ^{222}Rn rate over time, the fit results define counting regions for each isotope. We bin the data in time slices of 24 runs ($\sim$ 12 hours) and count the events in the region's isotope ($\mu \pm 2\ \sigma$). We correct for acceptance loss due to the two sigma region. The overlap region of ^{222}Rn and ^{218}Po, although the leakage in each other's regions is $\sim$ 0.1%, is accounted for in the final event count. The counts per time interval are divided by the total live time of the runs in the said interval and the fiducial mass to give the rate, expressed in μBq/kg.

The results of this are shown in Figure 6.22 for the ^{222}Rn chain and Figure 6.23 for the ^{220}Rn chain. The date where the Radon Distillation column is turned on (RAD start), 2021-07-05, is indicated with the blue line. After the

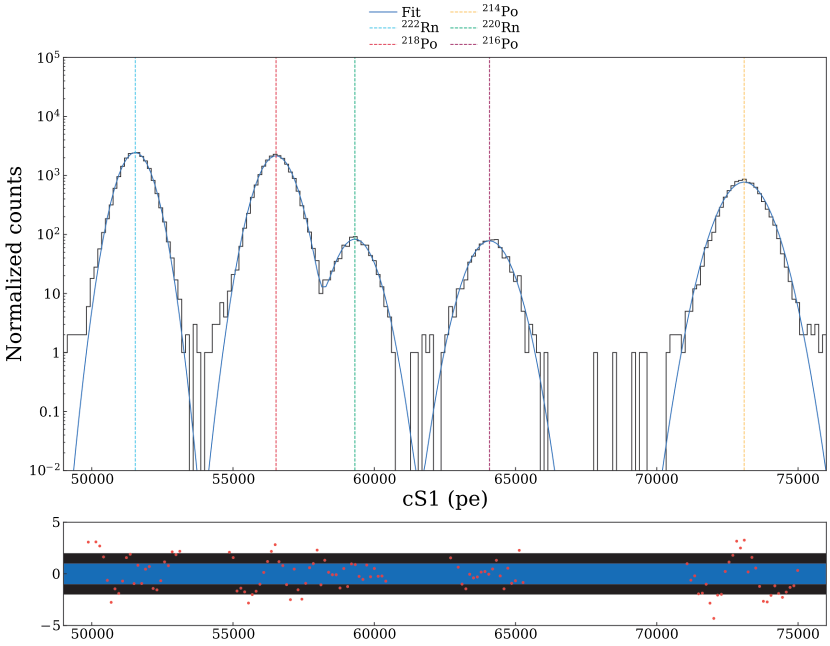

Figure 6.21 Fitted cS1 spectra in the alpha energy range 50× 10^5-80×10^5 within the fiducial volume as in Table 6.5. The peaks from left to right correspond to ^{222}Rn, ^{218}Po, ^{220}Rn, ^{216}Po and ^{214}Po. The spectrum is fitted with the sum of five Gaussians with the amplitudes and means left free and the relative width shared among all but ^{214}Po. The mean(μ) and width(σ) of the fit are used for determining the counting range for each isotope as ($\mu \pm 2\sigma$). Due to the cut on r_c^2 , ^{210}Po is removed as it is on the PTFE wall.

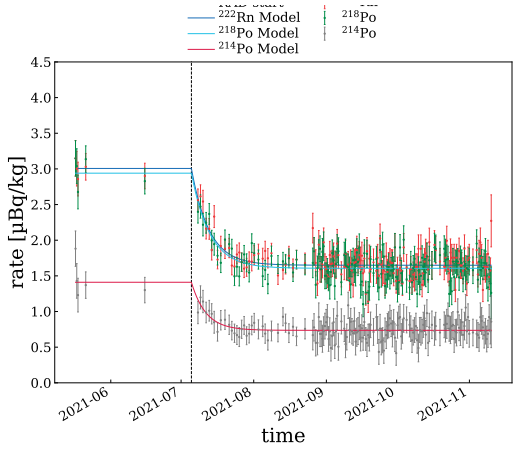

Figure 6.22 Rate evolution of ^{222}Rn (red), ^{218}Po (green), ^{214}Po (grey) over XENONnT SR0 background data. The rate is calculated by grouping together 24 subsequent runs (∼12 hours), summing all events within the counting range determined by the spectral fit for each isotope, and correcting for livetime and fiducial mass. The blue line indicates the start of the radon distillation column, causing an exponential decline of the alpha concentrations to an equilibrium value. The equilibrium value is calculated by fitting Eq. 6.12 for each isotope. The fit results are shown in dark blue (^{222}Rn), light blue (^{218}Po), and light red (^{214}Po), with the equilibrium values listed in Table 6.6

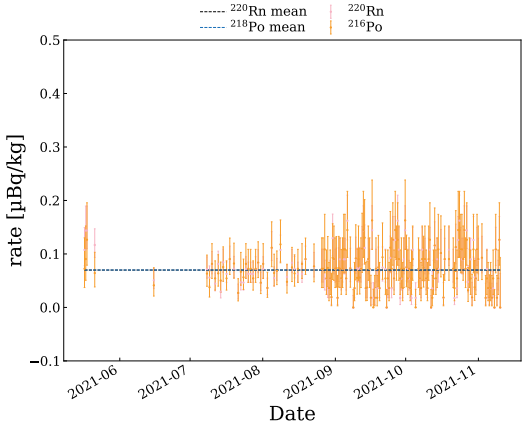

Figure 6.23 Rate evolution of ^{220}Rn (pink) and ^{216}Po (orange) during XENONnTs SR0 background data. The rate is calculated by grouping together 24 subsequent runs (∼12 hours), summing all events within the counting range determined by the spectral fit for each isotope, and correcting for livetime and fiducial mass. As the rate is already an order of magnitude below the ^{222}Rn chain, the ^{220}Rn chain is not affected by the radon distillation column. The equilibrium value is calculated as the median of all data points for ^{220}Rn (green) and ^{216}Po (red). The value is also listed in Table 6.6. The error is the standard deviation.

RAD start, the rate of all alpha decays exponentially decreased to a lower equilibrium rate. The final rates are calculated by fitting the following function to the ^{222}Rn chain data per isotope:

$$f(t) = (c_0 - c_1)\exp\Big[\frac{-(t-t_0)}{\tau}\Big] + c_1 \tag{6.12}$$

The constants c_0 and c_1 are the before and after RAD start equilibrium rates of isotopes, and τ a decay constant, all are left free for fitting.

For ^{220} Rn and ^{216}Po, the rate shows no decrease after the start of the RAD, so we take the mean value to calculate the equilibrium rate.

The final ^{222}Rn, ^{218}Po, ^{220}Rn, ^{216}Po, and ^{214}Po isotope rates XENONnT's SR0 are summarized in Table 6.7. The found rate of 1.65 μBq/kg of ^{222}Rn is slightly higher than the in Figure 6.4 assumed concentration of 1 μBq/kg. The ^{214}Po concentration is found to be only half of the ^{218}Po concentration. This is already seen in previous experiments like XENON1T and is assumed to be due to plate out on mainly the TPC cathode; this is the *cathode cleaning effect*. As the ionization fraction[192] of ^{218}Po after the ^{222}Rn decay is (50.3 ± 3)%, and that of^{214}Bi is (76.4 |± 5.7) following the ^{214}Pb decay, these ions are attracted due to the high negative voltage set to the cathode. The concentrations of ^{220}Rn and ^{216}Po of 0.7 μBq/kg. Using this concentration as an upper limit on the ^{212}Pb concentration, this shows the contamination of ^{212}Pb is more than a factor of 20 lower than ^{214}Pb. Thus, we can safely ignore this isotope.

Isotope	**Eq rate before** (μBq/kg)	**Eq rate after** (μBq/kg)
^{222}Rn	3.4 ± 0.1	1.67 ± 0.01
^{218}Po	3.3 ± 0.1	1.62 ± 0.01
^{220}Rn	0.07 ± 0.03	0.07 ± 0.03
^{216}Po	0.07 ± 0.03	0.07 ± 0.03
^{214}Po	1.5 ± 0.1	0.74 ± 0.01

Table 6.7 ^{222}Rn chain isotope rates before and after the start of the online radon distillation. The achieved reduction of factor 2.04 due to the online radon distillation agrees with the predicted reduction[193].

6.4.7 ^{214}Pb rate

Table 6.8 shows the expected ^{222}Rn and ^{214}Pb concentrations as determined by MC, emanation measurements, and the S1-only alpha analysis. The emanation measurement does not consider the effect of the online radon distillation, which results in a factor ∼two higher concentration. The last column shows the expected ^{214}Pb in the energy region of interest of (1,13) keV for ERs. The

number is calculated using a branching ratio of 10.9% for the direct-to-ground-state decay of ^{214}Pb, and the energy spectrum from [164]

Method	^{222}Rn (μBq/kg)	^{214}Pb (μBq/kg)	^{214}Pb [t · y]$^{-1}$ (RoI)
MC	1	1	55 ± 6
Emanation	$4.2 \pm {}^{0.5}_{0.7}$	$4.2 \pm {}^{0.5}_{0.7}$	$233 \pm {}^{28}_{39}$
S1-only analysis	1.67 ± 0.014	0.74 - 1.62	41 - 90

Table 6.8 Comparison of the expected and measured ^{222}Rn and ^{214}Pb concentrations in XENONnT SR0 from the MC[117], emanation measurements[179] and the S1-only alpha analysis. Note the emanation measurement does not include the effect of the online radon distillation, leading to factor ∼ two higher concentrations. The values for ^{214}Pb from the S1-only analysis are lower and upper limits based on the measured concentrations of ^{214}Po and ^{218}Po.

6.5 Conclusion

As XENONnT is designed as a low background experiment, verifying this goal is an important measurement. The dominant background in XENONnT comes from the low energy part of the beta decay from ^{214}Pb, which is part of the ^{222}Rn decay chain. ^{222}Rn continuously emanates from detector materials into the LXe. We set constraints on the ^{214}Pb concentration by doing an S1-only analysis of the alpha decays in the ^{222}Rn chain. The found concentrations of ^{218}Po (1.62 μBq/kg) and ^{214}Po (0.74 μBq/kg) set upper and lower limits on the ^{214}Pb concentration, in agreement with the MC expectation[117] and slightly below emanation measurements[179]. Both isotopes have a stable decay rate over XENONnT SR0. The found concentrations of ^{218}Po and ^{214}Po result in a rate between 41 - 90 [t y]$^{-1}$ in the low energy region of interest ((1,13) keV for ER) for DM search. This result shows XENONnT achieved its goal of a low-background experiment, suitable for DM searches.

An issue that is unaddressed so far is the issue due to the $\chi 2$/ndf of the fits required to do the correction. This leads to a systematic uncertainty. This is expected to result in a broadening of the fitted distributions in Figure 6.21. As the only isotopes with overlapping distributions, ^{218}Po and ^{220}Rn, and the low rate of the latter, this effect is considered negligible in the current analysis.

7

Solar axions

In this chapter, we present the result of a search for solar axions. XENONnT is sensitive to these axions if their couplings are of the order of $g_{ae} \sim 10^{-12}$ - 10^{-11} and $g_{a\gamma} \sim 10^{-12}$ - 10^{-8}, and are introduced in Section 2.3.1. The signal of solar axions is visible as an excess of low-energy ER events, similar to what was observed in XENON1T[165].

Rare event searches, as done in XENONnT, often use frequentist hypothesis testing to infer results on their results. The likelihood used in such cases revolves around the computation of the differential event rate. The standard method to compute the expected differential rate is by using large-scale Monte Carlo techniques to generate multi-dimensional histograms in the space of observables. Nuisance parameters are incorporated by simulation of the events for specific values of the nuisance parameter and interpolation between them. This simulation should be done on a fine grid with the most significant nuisance parameters to achieve high statistical accuracy. This is not possible from a practical point of view; the computation time scales with the binning and the number of nuisance parameters. Therefore, a choice has to be made to limit the number of relevant nuisance parameters and bins at the cost of statistical accuracy. This results in a lower signal and background discrimination power, making the analysis less robust[194].

The LXe TPC detector response model is relatively simple, which means that the differential rate can be expressed as an analytical function of observables. It also has nuisance parameters that are a function of these observables. Using TensorFlow[195] to implement the computation, we can access automatic differentiation, allowing the calculation to be done in reasonable computation time. Flamedisx[194] is an open-source Python package that provides an inference framework that works within six-dimensional space and offers good computing time. Section 7.1 describes some technical aspects of Flamedisx. In

Section 7.3, we present the results of statistical inference using this framework and the data obtained from XENONnT's first science data. We used this framework to search for excess events in the "Low ER" region from solar axions.

7.1 Flamedisx

The likelihood commonly used in DM searches is an extended unbinned profile likelihood[194]:

$$L = Poisson(N_{tot}|\mu) \prod_{i}^{events} \sum_{j}^{sources} \frac{R_j(s_i,\theta)}{\mu} + Constraints. \tag{7.1}$$

In this equation, Poisson is the Poisson probability mass function, $\mu = \sum_j \mu_j$ the total expected number of events from all sources, N_{tot} the total observed number of events. $R_j(s_i, \theta)$ is the differential rate for different signal or background sources:

$$R_j(s_i,\theta) = r_j \times M_j(s_i,\theta), \tag{7.2}$$

where r_j is the rate multiplier, and M_j is the differential rate as a function of observables s_i, and nuisance parameters θ used in the likelihood. In practice, the logarithm of equation 7.1 is used. Signals produced in LXe TPCs have position and time-dependent effects. To avoid having to account for these effects explicitly, the corrected S1 and S2 signals are used in the inference. Flamedisx (Fast Likelihood Analysis in MorE DImensionS for Xenon TPCs) uses all observables $S1, S2, x, y, z, t$. This allows all detector effects to be incorporated into the computation of the differential rate as a function of any of the observables.

7.1.1 XENONnT detector model

In Flamedisx, the detector model is implemented as a series of *model functions*. These model functions describe various processes like xenon scintillation, recombination, loss of electrons due to electron lifetime, reconstruction bias, and cut acceptances and are illustrated in Figure 7.1.

The LXe response model implemented for this analysis is the same as from [180]. The energy deposited by a particle interaction with LXe produces light and charge. The number of free quanta n_q is given by:

$$n_q = E/W, \tag{7.3}$$

with W (13.7 eV), the average energy required to produce one quantum. The probability of producing a number of quanta n_q for an energy deposition with

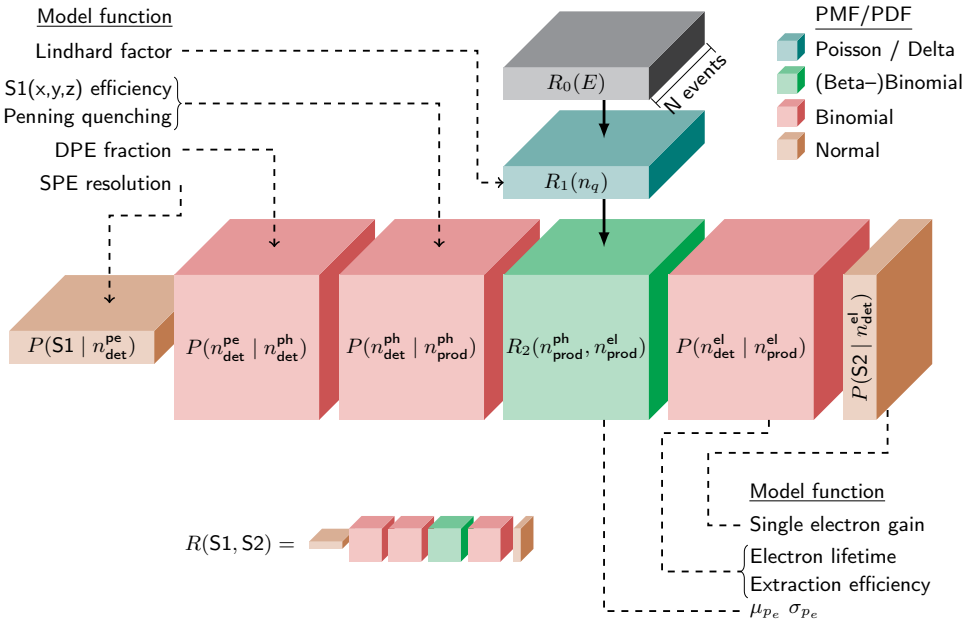

Figure 7.1 LXe emission model structure as implemented in Flamedisx. The color blocks represent different tensors corresponding to different steps in the calculation, with various model functions. The differential event rate is calculated as a multiplication of the tensors. The computation is batched over N events simultaneously to improve performance. From [194].

energy E is:

$$P(n_q, E) = \text{Poisson}(n_q E/W). \tag{7.4}$$

The differential rate of produced quanta, $R_1(n_q, \vec{x})$, is calculated with an input differential rate of energy, $R_0(E,\vec{x})$:

$$R_1(n_q, \vec{x}) = \sum_E P(n_q|E) R_0(E, \vec{x}). \tag{7.5}$$

The produced number of quanta n_q is divided over excitons n_{ex} and electron-ion pairs n_e. The number of produced ions and excimers depends on the exciton ion ratio:

$$n_i = \frac{n_q}{1 + \langle \frac{n_{ex}}{n_i} \rangle},$$
$$n_{ex} = n_q - n_i$$

The electron-ion pairs have a probability r to undergo recombination given by the modified Thomas-Imel box model:

$$r_{er} = 1 - \frac{\ln(1 + n_i \zeta_{er})}{n_i \zeta_{er}} \frac{1}{1 + e^{-(\epsilon - q_0/q_1)}},$$
$$\zeta_{er} = \gamma_{er} e^{-\epsilon/\omega_{er}} F^{-\delta_{er}}$$

where the recombination fluctuation δr is parametrized as:

$$\delta r = q_2(1 - e^{-\epsilon/q_3}), \tag{7.6}$$

with q_2 and q_3 free parameters. This empirical description reflects the observations that the recombination fluctuation goes down for smaller energy depositions and does not change energy depositions above $\sim$ 2 keV. The free parameters q_0, q_1, q_2, q_3, γ_{er}, ω_{er}, δ_{er} are obtained by fitting to calibration data, described in Section 7.2. The resulting probability of a quantum to produce an electron is then modeled as a Beta-Binomial distribution given by:

$$P(n^{el}_{prod}|n_q) = \text{BetaBinomial}(n^{el}_{prod}|n_q, r_{er}, \delta r) \tag{7.7}$$

We can now write the joint differential rate of the number of produced photons and electrons as:

$$R_2(n^{ph}_{prod}, n^{el}_{prod}, x) = \sum_{n_q} P(n^{el}_{prod}|n_q) R_q(n_q, \vec{x}) \delta(n_q - n_{ph} + n_{el}), \tag{7.8}$$

where the Dirac delta function guarantees the number of quanta is conserved.

Detection The detection probability of a quanta is described as a binomial multiplied by an acceptance function. The detection probability of a photon is given by:

$$P(n_{det}^{ph}|p_{prod}^{ph},\vec{x}) = f_{acc}(n_{ph})\text{Binom}(n_{det}|n_{prod},g_1(\vec{x})) \tag{7.9}$$

Here, g_1 is the average number of photoelectrons measured per photon, and the relative light yield is drawn from the normalized LCE map. f_{acc} is a photon acceptance and reconstruction efficiency function.

For electrons, the detection probability is a product of the extraction efficiency and the absorption probability due to the drift to the top of the TPC,

$$P(n_{det}^{el}|d_{prod}^{el}) = f^{el}(n_{det}^{el})\text{Binom}(n_{det}^{el}|n_{prod}^{el})\epsilon_{extr}e^{-t_{drift}/\tau}, \tag{7.10}$$

with $\text{f}^{el}(n_{det}^{el})$ the $S2$ acceptance and reconstruction bias function, a Gaussian distribution for the fluctuation of the number of photons produced per electron, extraction efficiency ϵ_{etr}, and an exponential to account for the loss of electrons due to the electron lifetime τ with drift time t_{drift}.

Differential rate The full differential rate $\text{R}(S1,S2,\vec{x})$ for an event given the model parameters is thus given by:

$$\begin{aligned} R(S1,S2,\vec{x}) = \sum_{n_{det}^{ph}}\sum_{n_{prod}^{ph}}\sum_{n_{prod}^{el}}\sum_{n_{det}^{el}} & P(S1|n_{det}^{ph})P(n_{det}^{ph}|n_{prod}^{ph}) \\ & R2(n_{prod}^{ph},n_{prod}^{el},\vec{x})P(n_{det}^{el}|n_{prod}^{el})P(S2|n_{det}^{el}). \end{aligned} \tag{7.11}$$

An alternative model is to have the quanta splitting done according to the latest NEST model[196]. The advantages of this are that it alleviates the need to fit an emission model and reduces the number of free parameters in the model. However, due to the current method of implementation, the RAM requirements of this model are so large that large-scale computation is unfeasible.

7.2 ER Band fitting

Fitting the recombination parameters described in Section 7.1 to data is challenging due to a high correlation between these parameters. As the model has many parameters, the minimizer can converge to non-sensible values even

with automatic differentiation. Furthermore, the available dataset is small, and a few outlying events can confuse the model. Additionally, the microphysical processes of xenon scintillation are not precisely known, and it is unclear whether the values are constant over an extensive energy range above 10 keV, which is relevant for solar axion analysis.

Previous measurements were used to constrain some of the parameters in the fitting procedure used here. The fit parameters are constrained by log normal to the best-fit values in [197].

The data used for the fit is obtained during calibration of the detector with ^{220}Rn up to 20 keV. The direct-to-ground state decay of ^{212}Pb at low energy provides a good dataset, where the input energy spectrum is the ^{212}Pb spectrum taken from [169]. Figure 7.2 shows the $cS1$ and $cS2$ distributions of an MC dataset of 10^6 simulated with the best-fit values and the calibration dataset. The goodness of fit is evaluated in cS1-cS2 space in equiprobable bins with binned Poisson χ^2 and is shown in Figure 7.3. The resulting goodness of fit is 0.1 up to 100 pe in $cS1$ ($\sim$ 10 keV) and 0.01 up to 150 pe ($\sim$ 15 keV). Almost the entire energy spectrum of Solar axions is below ten keV; this model is usable for Solar Axion search. But, this model is inappropriate for physics searches at higher energy, where the NEST model should be used.

Parameter	Constraint	Best fit
g_1 (pe/n$_{ph}$)	0.152	0.151 ± 0.001
single electron gain (n_{ph}/n_{el})	30.24	29.9 ± 0.1
$\langle \frac{n_{ex}}{n_i} \rangle$	0.09	0.08 ± 0.01
q_0 (keV)	0.76	0.94 ± 0.08
q_1 (keV)	0.65	0.59 ± 0.09
ω_{er} (keV)	29.19	43 ± 9
γ_{er}	0.145	0.13 ± 0.05
δ_{er}	-0.35	-0.31 ± 0.09
q_2	0.041,	0.042 ± 0.001
q_{3n_q} (keV)	17.59	18.3 ± 2.11

Table 7.1 ER model fit parameters, external constraints, and best-fit values. Parameters without a specified dimension are dimensionless.

7.3 Low ER analysis

This analysis uses Flamedisx as an inference framework to set constraints on the solar axion couplings g_{ae} and $g_{a\gamma}$. We use two Flamedisx ER sources with the model described in the previous sections. The background energy spectra

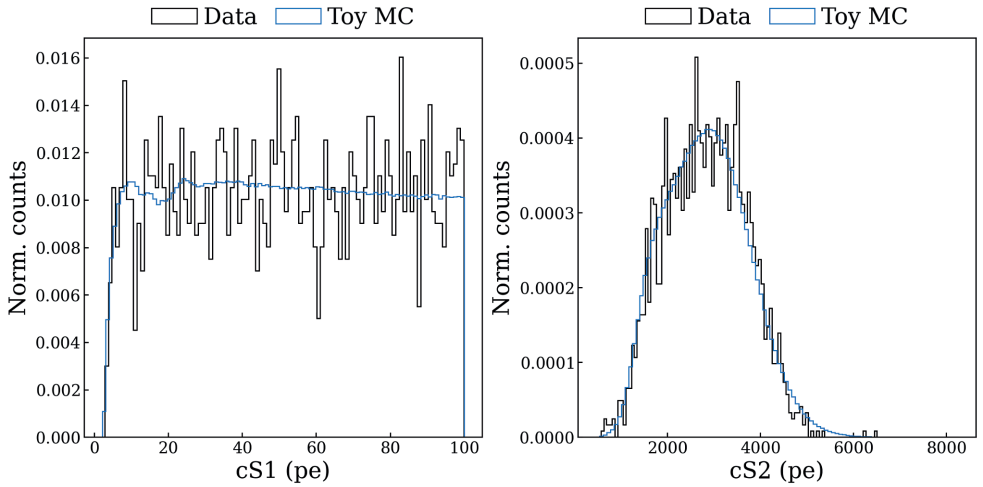

Figure 7.2 Histograms of $cS1$ (left) and $cS2$ (right) distributions for both ^{220}Rn calibration data (black) and toy MC simulations (blue), indicating good agreement between the data and the model.

for the ER sources are taken from theory and are the same as in the previous chapter. We use a four-component model for the Solar Axion spectrum. Axion production via the ABC and Primakov processes and detection to occur via the axio-electric and inverse-Primakov effects, as described in Section 2.3.1. Both spectra are shown in Figure 7.4, with fixed values of g_{ae} and $g_{a\gamma}$. The contribution of ^{57}Fe is ignored for simplicity. Figure 7.5 shows the XENONnT SR0 science run data overlaid on the 1, 2, and 3 sigma contours of the solar axion source (top) and the ER background source (bottom).

To set limits on the solar axion couplings, a test statistic q discriminates between signal and background-only hypotheses. The test statistic q is calculated as:

$$q = -2\log\left(\frac{L(\mu_s, \hat{\hat{\mu}}_b, \theta)}{L(\hat{\mu}_s, \hat{\mu}_b, \theta)}\right). \tag{7.12}$$

Here, L denotes the likelihood function defined as 7.1, μ_s the number of signal events, μ_b the number of background events, and θ the nuisance parameters. The set (μ_s, $\hat{\hat{\mu}}_b$, θ) are such that L is maximized for a given number of axion events μ_s and fixed nuisance parameters θ, as listed in Table 7.1. The set ($\hat{\mu}_s$, $\hat{\mu}_b$, θ) are the global best-fit values for fixed θ. The nuisance parameters θ are fixed to reduce computation time. The comparison between $L(\mu_s, \hat{\hat{\mu}}_b, \theta)$ and the global best fit $L(\hat{\mu}_s, \hat{\mu}_b, \theta)$ via q evaluates the compatibility of the data with the fixed signal hypothesis relative to the best-fit values. We calculate the value of q on a 10 by 10 grid with geometric spacing for $10^{-13} < g_{ae} <$

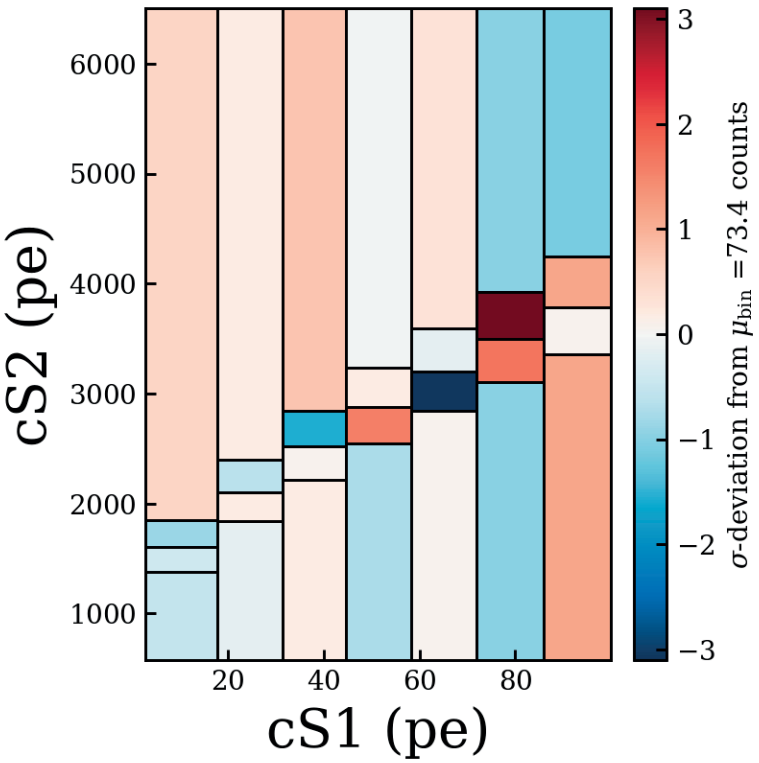

Figure 7.3 Deviation of the $cS1$ vs. $cS2$ distribution of ^{220}Rn calibration data compared to the toy MC simulation, binned in equiprobable bins. The color scale shows the data's positive (red) and negative (blue) deviations.

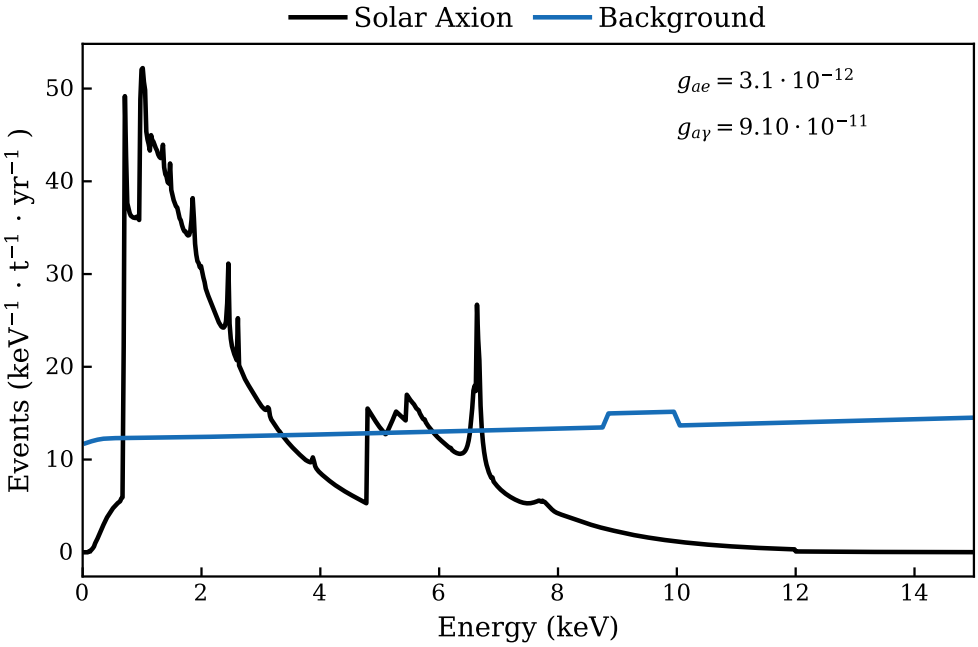

Figure 7.4 Energy spectrum of the Solar axion with $g_{ae} = 3.1 \times 10^{-12}$ and $g_{a\gamma}$=9.10 $\times 10^{-11}$ (black), and the ER background spectrum (blue). The background spectrum is dominated by ^{214}Pb and a bump at nine keV from the LL-shell of ^{124}Xe $2\nu\beta\beta$.

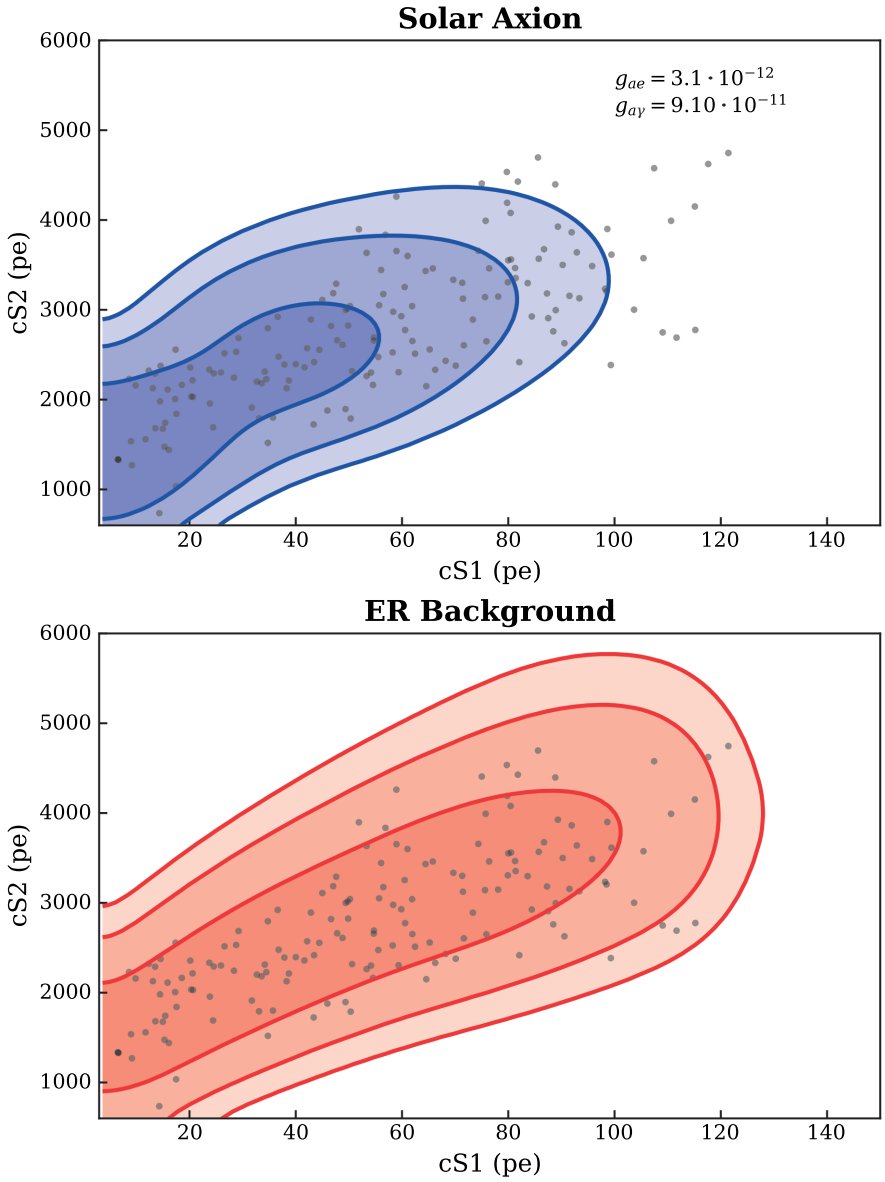

Figure 7.5 Scatter plots showing the $cS1$ vs. $cS2$ distribution of XENONnT SR0 science run data. The top plot displays the 1, 2, and 3 sigma contours of the solar axion source in blue with overlaid data, showcasing a higher differential rate for events at low energy. The bottom plot presents the corresponding contours for the ER background in red, exhibiting a consistent differential rate across the entire energy range.

3×10^{-12} and $10^{-12} < g_{a\gamma} < 10^{-9}$. The number of background events is constrained to the expected number of events according to the background best-fit model of [163].

An understanding of the test statistic distribution q is required to determine a limit. In this case, we assume Wilks theorem[198] to hold, and the q value follows a χ^2 distribution with 1 degree of freedom. Therefore, a 90% confidence exclusion limit is set at a q-value of 2.7. To calculate to what values of g_{ae} and $g_{a\gamma}$ this corresponds, we interpolate the calculated values of q on the g_{ae} - $g_{a\gamma}$ grid using a bivariate spline interpolation. The resulting limits of g_{ae} and $g_{a\gamma}$ are shown in Figure 7.6. This plot includes the limits from other experiments like LUX, PANDAX-II, Majorana, theory constraints on the KSVZ and DFSZ models, as well as astrophysical constraints from HB stars, red giants, white dwarfs, and solar neutrinos[163]. The blue band indicates the observed contour of the XENON1T excess[165]. This analysis follows the results from [163] very well, even with this simplified statistical approach.

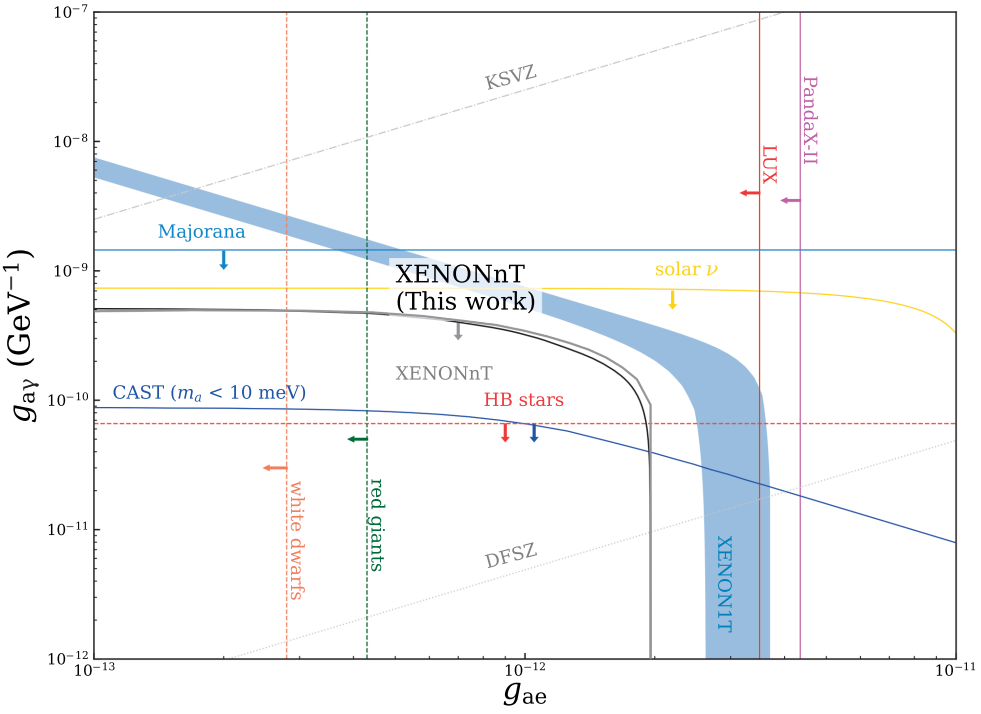

Figure 7.6 Limits on the Solar Axion couplings g_{ae} vs. $g_{a\gamma}$. The black line shows the limit of this analysis, and the grey line shows the limit of the official XENONnT result[163]. This result shows the feasibility of using Flamedisx to calculate the results of XENONnT in the future.

7.4 Conclusion

In this chapter, we present the search for solar axions using XENONnT's first science data and the use of Flamedisx as an inference framework. Flamedisx provides a powerful tool for searching for rare event signals, such as solar axions, by incorporating various detector effects into the computation of the differential rate as a function of any of the observables. Our approach serves as a necessary cross-check to ensure the compatibility of results obtained through different methodologies.

The use of Flamedisx in a solar axion search does not necessarily result in enhanced sensitivity. This is because we only use ER sources with the same position and time dependencies. In contrast, the NR source varies for a WIMP analysis, resulting in significant differences in differential rates.

However, it is important to note that Flamedisx has some limitations, such as assuming a relatively simple detector response and potentially sacrificing accuracy for computing time. Despite these limitations, Flamedisx remains a valuable tool for searching for rare event signals, such as solar axions, and provides a promising direction for future research. Overall, the search for solar axions using XENONnT's first science data provides an opportunity to test the axion-electron and axion-photon coupling strengths, and the results obtained from Flamedisx demonstrate the importance of using advanced statistical inference techniques in rare event searches.

In future investigations, we need to allow the axion couplings g_{ae} and $g_{a\gamma}$ to vary independently and to include the ^{57}Fe production channel. The rate multiplier depends on the square of the different axion couplings dependent on the different production and detection channels. However, the axion couplings are independent of each other and should be allowed to change freely.

For future Flamedisx analysis, further development of source implementations based on NEST models is crucial. This approach streamlines the convergence of model parameters, eliminating the need for external measurements. Furthermore, it allows for broader inference over a wider energy range, enabling a more straightforward analysis of phenomena such as Axion-like Particles up to hundreds of keV or Dark Matter Effective Field Theory (DM EFT) models with couplings peaking at higher energies. [199][200]

Summary of Electronic recoils in XENONnT

Chapter 1: Dark Matter Dark Matter is one of the biggest mysteries in modern astroparticle physics. Although it dominates the Universe, we cannot detect it directly because it does not interact with light. Astrophysical evidence supports the Dark Matter hypothesis. One piece of evidence comes from the Cosmic Microwave Background (CMB) analysis. The CMB, which is microwave radiation from the early Universe, shows tiny fluctuations that are attributed to density fluctuations caused by dark matter. The temperature anisotropies of the CMB have been studied by several satellites, and the resulting power spectrum provides constraints on the composition of the Universe. The CMB measurements suggest that our Universe is spatially flat and consists of 5% baryonic matter, 27% dark matter, and 68% dark energy. The presence of dark matter is necessary to explain the observed fluctuations in the CMB and the formation of observable galaxies. One of the ways to detect dark matter is through scattering, where a dark matter particle collides with an atomic nucleus, producing a signal that can be detected.

Chapter 2: Signals in a Dark Matter detector A dark matter detector can potentially detect signals of WIMP-nucleus interactions and other exotic particles such as solar axions and axion-like particles. The WIMP-nucleus cross-section depends on the WIMP-quark interaction and has both Spin Independent (SI) and Spin-Dependent (SD) contributions. Solar axions can be produced in the Sun via the ABC process, the Primakoff effect and a nuclear transition of ^{57}Fe. These axion could be detected by a dark matter detector via the axio-electric, or the inverse Primakoff effect. The rates and energy spectrum will depend on the couplings of the axion.

Chapter 3: The XENONnT experiment One type of dark matter detector is a dual-phase xenon Time Projection Chamber (TPC). The XENONnT

experiment, located at Laboratori Nazionali del Gran Sasso in Italy, is one such detector. The TPC is filled with liquid and gas xenon and enclosed by interlocking PTFE panels. A particle interacting with the xenon will produce direct scintillation light ($S1$) and ionization electrons. The S1 scintillation light is directly measured with Photomultiplier tubes (PMTs) at the top and bottom of the TPC. An electric field is used to drift the electron to the top of the TPC, where an extraction electric field is used to produce a secondary scintillation signal ($S2$). Based on the time delay between the S1 and S2, we calculate the z-coordinate of the interaction, and the hit pattern of the S2 is used for reconstructing the xy-coordinate. The sizes of the S1 and S2 depend on the energy deposited by the interacting particle. Using this information, we distinguish background from potential dark matter events.

Chapter 4: The XENONnT Data Acquisition System The XENONnT Data Acquisition System (DAQ) is a triggerless system designed to acquire data constantly without a global trigger. It uses custom readout logic to allow for independent readout of all detector channels while maintaining full time-synchronization. The data is stored on disk and physical interactions are identified later during processing. The DAQ is located in the XENONnT service building and consists of separate systems for the TPC, Muon Veto (MV), and Neutron Veto (NV) PMTs. The DAQ is designed to fulfill criteria such as low energy threshold, low noise, low dead time, high data rates, dual gain readout, fast data processing, and a high-energy veto. The hardware components of the DAQ include PMTs, custom-made amplifiers, and digitizer modules.

The DAQ can handle high data rates and has high live time. The system can operate independently or as a linked system. The dead time fraction is low during science data taking but increases during high-rate calibration. The system has taken data with rates up to 500 MB/s and provides high-level data for analysis. The electronic noise levels are low, and the system allows for online processing and monitoring of detector conditions.

Chapter 5: XENONnT Monte Carlo framework The XENONnT MC framework consists of three separate packages: Geant4, EPIX, and WFSim. Geant4 is used to simulate particle interactions within the detector, EPIX converts energy deposits into detectable photons and electrons, and WFSim simulates the detector response. Each package has specific functions and follows a series of steps to generate the desired output. The simulation framework is contained within a CernVM File System container. Geant4 accurately models the XENONnT detector and its optical properties. EPIX uses the DBSCAN

algorithm to cluster energy deposits and convert them into detectable quanta. WFSim simulates the detector response for a given number of quanta and interaction positions. The simulation framework is a crucial tool in assessing detector feasibility and providing input for data analysis.

The XENONnT Monte Carlo framework includes modeling photon arrival time on the photocathode and simulating the S2 signal. The modeling of the S2 signal involves the transport of electrons towards the LXe/GXe interface, where they are extracted into the GXe phase and generate the S2 signal through electroluminescence. The magnitude of the S2 signal is influenced by the electric field in this region, GXe pressure, and the electron's path length within the gap. The propagation time of S2 photons is sampled from a Geant4 simulation. The simulated PMT pulses are generated by sampling the photon arrival times and channels, and the resulting waveform data is processed to resemble real data.

We present two separate results to validate the Monte Carlo framework's accuracy. The detector parameters g_1 and g_2, the number of measured photo-electrons by the PMTs per produced photon (g_1) or electron (g_2), are important input parameters for the simulation. We simulate the signals produced by mono-energetic electron capture and gamma-ray sources to reconstruct the values of g_1 and g_2. The values are slightly below the configuration values, but overall, they demonstrate the reliability of the simulation. Additionally, we validated the simulation by comparing the background model of the first science run of XENONnT with the observed data and found a satisfactory agreement between the two ($\chi_2/dof = 0.66$).

Chapter 6: Radon induced background We summarize the background expectations for both ER and NR events in XENONnT. The most significant contribution to the ER background is from ^{214}Pb, which comes from the decay of ^{222}Rn. The ^{214}Pb rate can be constrained by measuring the rate of various alpha decay from the ^{222}Rn chain.

The analysis focuses on correcting for various dependencies of the S1 signals in the TPC. The S1-only alpha analysis selects S1 signals larger than 10^4 pe and shows bands corresponding to alpha decays. The spectral fit is performed on the corrected area spectrum using five Gaussians. The fit results are used to determine counting regions for each isotope. The rate exponentially decreases after the Radon Distillation column is turned on. The concentration of ^{214}Pb is determined to be between 0.74 and 1.62 μBq/kg, compatible with the Monte Carlo expectation of 1 μBq/kg.

Chapter 7: Solar axions We present the results of a solar axion search using the data of the first science run of XENONnT using Flamedisx as an inference framework. Flamedisx calculates the differential rate of all events using six observables ($S1$, $S2$, x, y, z, t), and the likelihood is minimized using TensorFlow's auto differentiation to calculate the gradient and Hessian. The implemented LXe emission models are based on the same model as used for the XENONnT WIMP results, and the detector response is modeled as analytical functions depending on, at most, six observables. We include scatter plots showing the distribution of events from the solar axion source and the ER background, with corresponding contours. We test statistic distribution q is calculated, and a limit is set using Wilks' theorem. The resulting limits on the axion couplings g_{ae}, and $g_{a\gamma}$ are shown in Figure 7.7. The analysis serves as an important cross-check and shows the feasibility of using Flamedisx to calculate the results of XENONnT.

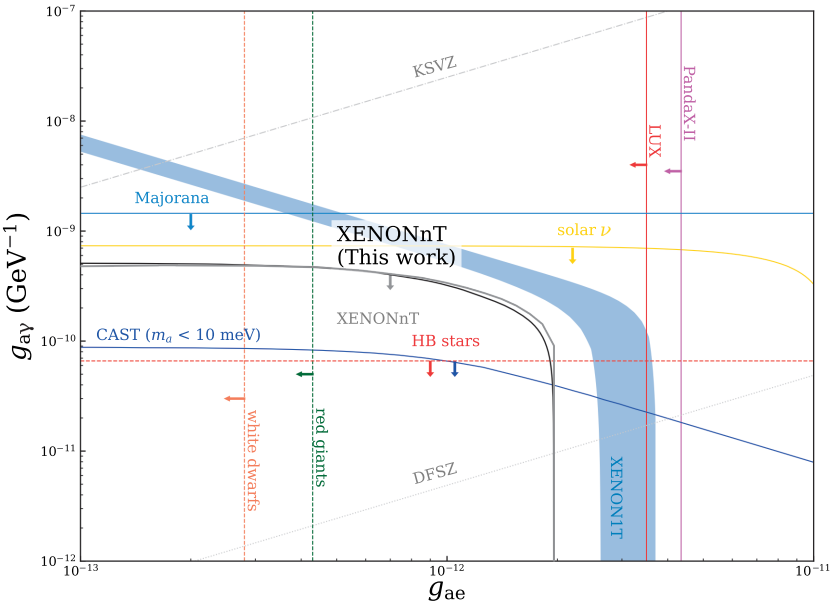

Figure 7.7 Limits on the Solar Axion couplings g_{ae} vs. $g_{a\gamma}$. The black line shows the limit of this analysis, and the grey line shows the limit of the official XENONnT result[163]. This result shows the feasibility of using Flamedisx to calculate the results of XENONnT in the future. Corresponds to Figure 7.6

Samenvatting van Electronic recoils in XENONnT

Donkere Materie is een van de grootste mysteries in de moderne astrodeeltjesfysica. Hoewel het het universum domineert, kunnen we het niet direct detecteren omdat het niet direct reageerd met licht. Astrofysisch bewijs ondersteunt de hypothese van Donkere Materie. Een hiervan komt van de analyse van de Cosmic Microwave background (CMB). De CMB, die microgolfstraling is uit het vroege universum, toont kleine fluctuaties die worden toegeschreven aan dichtheidsfluctuaties veroorzaakt door donkere materie. De temperatuuranisotropieën van de CMB zijn bestudeerd door verschillende satellieten, en het resulterende spectrum geeft beperkingen op de samenstelling van het Universum. De CMB-metingen suggereren dat ons universum ruimtelijk vlak is en bestaat uit 5% baryonische materie, 27% donkere materie, en 68% donkere energie. De aanwezigheid van donkere materie is noodzakelijk om de waargenomen fluctuaties in de CMB en de vorming van waarneembare sterrenstelsels te verklaren. Een van de manieren om donkere materie te detecteren is door verstrooiing, waarbij een deeltje donkere materie botst met een atoomkern, wat een signaal produceert dat kan worden gedetecteerd.

Hoofdstuk 2: Signalen in een Donkere Materie detector Een detector voor donkere materie kan mogelijk signalen van WIMP-nucleusinteracties en andere exotische deeltjes zoals solar-axions en axion like paricles detecteren. De WIMP-nucleus doorsnede is afhankelijk van de WIMP-quark interactie en heeft zowel Spin Onafhankelijke (SI) als Spin Afhankelijke (SD) bijdragen. Solar axions kunnen in de zon worden geproduceerd via het ABC-proces, het Primakoff-effect en een nucleaire overgang van ^{57}Fe. Deze axionen kunnen worden gedetecteerd door een detector voor donkere materie via het axio-elektrische, of het inverse Primakoff-effect. De hoeveelheid en het energiespectrum zullen afhangen van de koppelingen van de axion.

Hoofdstuk 3: Het XENONnT experiment Een type detector voor donkere materie is een dual phase xenon Time Projection Chamber (TPC). Het XENONnT-experiment, gelegen in Laboratori Nazionali del Gran Sasso in Italië, is zo'n detector. De TPC is gevuld met vloeibare en gasvormige xenon en omgeven door PTFE-panelen. Een deeltje dat interactie heeft met het xenon zal scintillatielicht ($S1$) en ionisatie-elektronen produceren. Het S1-scintillatielicht wordt direct gemeten met fotomultiplicatorbuizen (PMT's) aan de boven- en onderkant van de TPC. Een elektrisch veld wordt gebruikt om het electron naar de bovenkant van de TPC te drijven, waar een extractie-elektrisch veld wordt gebruikt om een secundair scintillatiesignaal ($S2$) te produceren. Op basis van de tijdvertraging tussen de S1 en S2 berekenen we de z-coördinaat van de interactie, en het trefferpatroon van de S2 wordt gebruikt voor het reconstrueren van de xy-coördinaat. De groottes van de S1 en S2 zijn afhankelijk van de energie depositie door het inkomende deeltje. Met deze informatie onderscheiden we achtergrond van potentiële donkere materie-evenementen.

Hoofdstuk 4: Het XENONnT Data-acquisitiesysteem Het XENONnT Data-acquisitiesysteem (DAQ) is een systeem ontworpen om continu gegevens te verwerven zonder een globale trigger. Het gebruikt uitleeslogica om onafhankelijke uitlezing van alle detector kanalen mogelijk te maken. De gegevens worden opgeslagen op een harde schrijf schijf en interacties worden later tijdens de data verwerking geïdentificeerd. Het DAQ bevindt zich in het XENONnT servicegebouw en bestaat uit afzonderlijke systemen voor de TPC, Muon Veto (MV), en Neutron Veto (NV) PMT's.

Het systeem kan onafhankelijk of als een gekoppeld systeem werken. Het systeem heeft gegevens verzameld met snelheden tot 500 MB/s en levert gegevens van hoog niveau voor analyse. Het elektronische ruisniveau is laag, en het systeem maakt online verwerking en monitoring van detectorcondities mogelijk.

Hoofdstuk 5: XENONnT Monte Carlo framework Het XENONnT MC framework bestaat uit drie afzonderlijke delen: Geant4, EPIX en WFSim. Geant4 wordt gebruikt om deeltjesinteracties binnen de detector te simuleren, EPIX zet energiedeposities om in detecteerbare fotonen en elektronen, en WFSim simuleert de reactie van de detector. Elk deel heeft specifieke functies en volgt een reeks stappen om de gewenste uitvoer te genereren. Het simulatieframework is opgenomen in een CernVM-container. Geant4 modelleert nauwkeurig de XENONnT-detector en zijn optische eigenschappen. EPIX gebruikt het DBSCAN-algoritme om energiedeposities te clusteren en ze om te

zetten in detecteerbare quanta. WFSim simuleert de reactie van de detector voor een gegeven aantal quantums en interactieposities. Het simulatieframework is een cruciaal hulpmiddel bij het beoordelen van de haalbaarheid van de detector en het leveren van input voor data-analyse.

Het XENONnT Monte Carlo framework omvat het modelleren van de aankomsttijd van fotonen op de fotokathode en het simuleren van het S2-signaal. Het modelleren van het S2-signaal omvat het transport van elektronen naar de LXe/GXe-interface, waar ze worden geëxtraheerd naar de GXe-fase en het S2-signaal genereren door elektroluminescentie. De grootte van het S2-signaal wordt beïnvloed door het elektrische veld in dit gebied, de GXe-druk en de padlengte van het elektron binnen de spleet. De propagatietijd van S2-fotonen wordt bemonsterd uit een Geant4-simulatie. De gesimuleerde PMT-pulsen worden gegenereerd door het bemonsteren van de aankomsttijden van fotonen en kanalen, en de resulterende golfvormgegevens worden verwerkt om op echte gegevens te lijken.

We presenteren twee afzonderlijke resultaten om de nauwkeurigheid van het Monte Carlo framework te valideren. De detectorparameters g_1 en g_2, het aantal gemeten foto-elektronen door de PMT's per geproduceerd foton (g_1) of elektron (g_2), zijn belangrijke invoerparameters voor de simulatie. We simuleren de signalen die worden geproduceerd door mono-energetische elektronenvangst en gammastraalbronnen om de waarden van g_1 en g_2 te reconstrueren. De waarden liggen iets onder de configuratiewaarden, maar over het geheel genomen demonstreren ze de betrouwbaarheid van de simulatie. Daarnaast hebben we de simulatie gevalideerd door het achtergrondmodel van de eerste wetenschappelijke run van XENONnT te vergelijken met de waargenomen gegevens en vonden we een bevredigende overeenkomst tussen de twee ($\chi_2/dof = 0.66$).

Hoofdstuk 6: Radon geïnduceerde achtergrond We vatten de achtergrondverwachtingen samen voor zowel ER- als NR-evenementen in XENONnT. De meest significante bijdrage aan de ER-achtergrond komt van ^{214}Pb, dat voortkomt uit het verval van ^{222}Rn. De ^{214}Pb-concentratie kan indirect bepaalt worden door het meten van verschillende isotopen uit de ^{222}Rn-vervalsketen.

De analyse richt zich op het corrigeren van verschillende afhankelijkheden van de S1-signalen in de TPC. De S1-only-alfa-analyse selecteert S1-signalen groter dan 10^4 pe en toont banden die overeenkomen met alfavervallen. De resultaten van de aanpassing worden gebruikt om telgebieden voor elk isotoop te bepalen. De concentratie van de vervalsproducten neemt exponentieel af nadat de Radon Distillatiekolom is ingeschakeld, Van ^{214}Pb wordt bepaald de concentratie tussen 0.74 en 1.62 μBq/kg te liggen, compatibel met de Monte

Carlo verwachting van 1 μBq/kg.

Hoofdstuk 7: Solar axions We presenteren de resultaten van een zoektocht naar solar axions met behulp van de data van de eerste wetenschappelijke run (SR0) van XENONnT, gebruikmakend van Flamedisx. Flamedisx berekent het differentiële rate van alle events met zes observabelen ($S1$, $S2$, x, y, z, t), en de waarschijnlijkheid wordt geminimaliseerd met behulp van TensorFlow's auto-differentiatie om de gradiënt en Hessian te berekenen. De geïmplementeerde LXe-emissiemodellen zijn gebaseerd op hetzelfde model als gebruikt voor de XENONnT WIMP-resultaten, en de detectorrespons wordt gemodelleerd als analytische functies afhankelijk van, hooguit, zes observabelen. We berekenen de teststatistiekverdeling q, en zetten een limiet met behulp van Wilks' theorema. De resulterende limieten op de axionkoppelingen g_{ae} en $g_{a\gamma}$ worden getoond in Figuur 7.8. De analyse dient als een belangrijke kruiscontrole en toont de haalbaarheid van het gebruik van Flamedisx om de resultaten van XENONnT te berekenen.

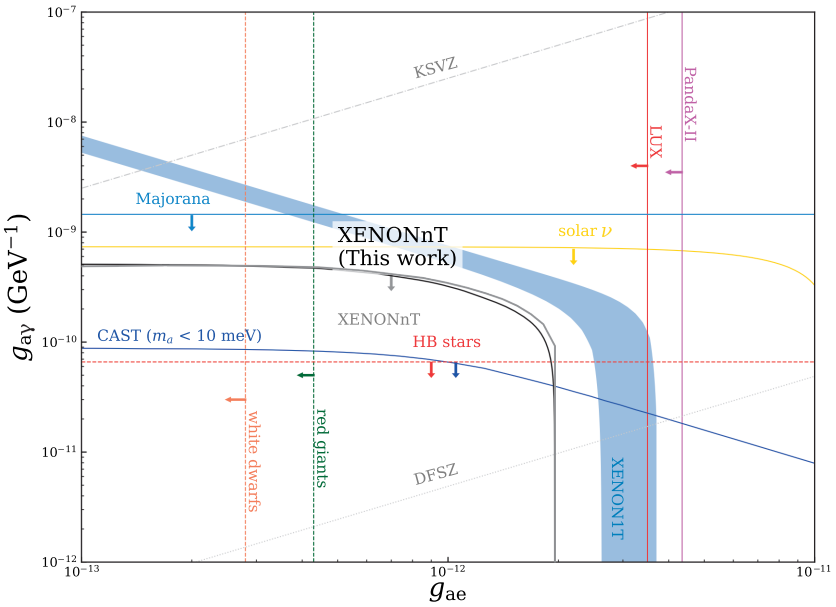

Figure 7.8 Limieten voor de Axion-koppelingen g_{ae} tegen $g_{a\gamma}$. De zwarte lijn toont de limiet van deze analyse en de grijze lijn toont de limiet van het officiële XENONnT-resultaat[163]. Dit resultaat laat zien dat het haalbaar is om Flamedisx te gebruiken om de resultaten van XENONnT in de toekomst te berekenen. Komt overeen met Figuur 7.6.

Acknowledgments

My deepest thanks go to my supervisors, Patrick and Auke-Pieter, for your unwavering support and guidance throughout my PhD journey. Your ability to let me carve my own path and your readiness to assist whenever I reached out has been invaluable, even though I seldom did.

Central to my experience were my postdoc, Stefan, and fellow PhD student, Joran. Your presence made my PhD extremely enjoyable. From engaging in debates on eccentric software or theoretical radon discussions to enduring many Bergfests together, you've enriched my PhD experience immeasurably. Memorable moments like braving the Egmond half marathon in winter, our trip to Chicago, and cabling the DAQ for three weeks, remain highlights. And Lodewijk, for not just joining in our Bergfests but also taking the leap to go skydiving with me. Alvaro, Bouke, Clara, Eleftheria, Evelin, Rob, Zhanna, Gijs, Lucas, Olivier, Gino, Brian, Ariane, and Ashley – your company was always a delight.

I want to express my gratitude to the "old guard" — Jelle, Sander, and Erik. Despite our brief overlap, your foundational support and advice on everything from plots to software documentation were crucial to my start. I also want to thank Chris for looking after me, especially in the beginning when I'd be the only PhD student attention software workshops. Those were a bit intimidating.

A heartfelt thank you to the next wave of the Dark Matter group: Carlo, Maricke, Vikas, Kelly, Marjolein, Pranati, Saad, Maxime, and James. Remember, don't forget to live.

To my friends from the gravitational waves group – Anna, Jesse, Maria, John, Michele, Nathan, and Tony – our Friday night "brainstorming" is legendary. We solved all the world's problems and could have claimed all Nobel Prizes with just the puppy CV, or the eagle - platypus bomber. And yes, barbecuing on a boat in the rain in the winter is just a brilliant idea.

Special thanks to my XENON friends, especially Diego, for being a lifeline on Slack during the lockdowns. Those daily exchanges were a beacon of joy. To the XENON DAQ group – Dan, Jelle, Joran, Alexey, and Darryl – it's nothing short of a miracle how well everything worked, considering our intricate web of

cables.

I can't overlook my "non-physics" friends, Pieter and Hessel, for offering a glimpse of normalcy and grounding me with their perspective.

Finally, to Veronica, Kees, Jim, Cornalien, Vincent, and Anne, your support has been my stronghold, particularly through the challenging final years. Thank you for being there for me throughout this entire endeavor.

Bibliography

1. Bertone, G. & Hooper, D. History of dark matter. *Reviews of Modern Physics* **90,** 045002 (2018).
2. Secchi, A. L'astronomia in Roma nel pontificato DI Pio IX. *Roma* (1877).
3. Zwicky, F. The redshift of extragalactic nebulae. *Helvetica Physica Acta* **6,** 110–127 (1933).
4. Clausius, R. XVI. On a mechanical theorem applicable to heat. *The London, Edinburgh, and Dublin Philosophical Magazine and Journal of Science* **40,** 122–127 (1870).
5. Martin, S. P. in *Perspectives on supersymmetry II* 1–153 (World Scientific, 2010).
6. Cheng, H.-C., Feng, J. L. & Matchev, K. T. Kaluza-Klein Dark Matter. *Physical Review Letters* **89.** ISSN: 1079-7114. `http://dx.doi.org/10.1103/PhysRevLett.89.211301` (2002).
7. Grupen, C., Cowan, G., Eidelman, S. & Stroh, T. *Astroparticle physics* (Springer, 2005).
8. Raby, S. Grand unified theories. *arXiv preprint hep-ph/0608183* (2006).
9. Ling, S. J., Sanny, J. & Moebs, W. *Evolution of Universe after the Big Bang* `https://pressbooks.online.ucf.edu/osuniversityphysics3/chapter/evolution-of-the-early-universe/` ().
10. Einstein, A. Approximative integration of the field equations of gravitation. *Sitzungsber. Preuss. Akad. Wiss. Berlin (Math. Phys.)* **1916,** 1 (1916).
11. Bertone, G. *Particle Dark Matter: Observations, Models and Searches* (Cambridge University Press, 2010).
12. Penzias, A. A. & Wilson, R. W. A measurement of excess antenna temperature at 4080 Mc/s. *The Astrophysical Journal* **142,** 419–421 (1965).

13. Smoot, G. F. *et al.* Structure in the COBE differential microwave radiometer first-year maps. *The Astrophysical Journal* **396,** L1–L5 (1992).

14. Bennett, C. L. *et al.* The Microwave Anisotropy Probe* Mission. *The Astrophysical Journal* **583,** 1 (2003).

15. Ade, P. A. *et al.* Planck 2015 results-xiii. cosmological parameters. *Astronomy & Astrophysics* **594,** A13 (2016).

16. Hu, W. & Dodelson, S. Cosmic Microwave Background Anisotropies. *Annual Review of Astronomy and Astrophysics* **40,** 171–216. ISSN: 1545-4282. http://dx.doi.org/10.1146/annurev.astro.40.060401.093926 (2002).

17. Ridpath, I. *A dictionary of astronomy* (Oxford University Press, 2012).

18. Rubin, V. C., Burstein, D., Ford Jr, W. K. & Thonnard, N. Rotation velocities of 16 SA galaxies and a comparison of Sa, Sb, and SC rotation properties. *The Astrophysical Journal* **289,** 81–98 (1985).

19. Bosma, A. 21-cm line studies of spiral galaxies. II. The distribution and kinematics of neutral hydrogen in spiral galaxies of various morphological types. *The Astronomical Journal* **86,** 1825–1846 (1981).

20. Portail, M., Gerhard, O., Wegg, C. & Ness, M. Dynamical modelling of the galactic bulge and bar: the Milky Way's pattern speed, stellar and dark matter mass distribution. *Monthly Notices of the Royal Astronomical Society* **465,** 1621–1644. ISSN: 1365-2966. http://dx.doi.org/10.1093/mnras/stw2819 (2016).

21. Liu, C. *et al.* Mapping the Milky Way with LAMOST I: method and overview. *Research in Astronomy and Astrophysics* **17,** 096 (2017).

22. Deason, A. J. *et al.* The edge of the Galaxy. *Monthly Notices of the Royal Astronomical Society* **496,** 3929–3942 (2020).

23. Sofue, Y., Honma, M. & Omodaka, T. Unified Rotation Curve of the Galaxy — Decomposition into de Vaucouleurs Bulge, Disk, Dark Halo, and the 9-kpc Rotation Dip —. *Publications of the Astronomical Society of Japan* **61,** 227–236. https://doi.org/10.1093%2Fpasj%2F61.2.227 (2009).

24. *Chandra :: Six galaxy clusters :: March 26, 2015,* https://chandra.harvard.edu/photo/2015/dark/.

25. Clowe, D., Gonzalez, A. & Markevitch, M. Weak-Lensing Mass Reconstruction of the Interacting Cluster 1E 0657-558: Direct Evidence for the Existence of Dark Matter. *The Astrophysical Journal* **604,** 596–603. ISSN: 1538-4357. http://dx.doi.org/10.1086/381970 (2004).

26. Diemand, J. *et al.* Clumps and streams in the local dark matter distribution. *Nature* **454,** 735–738. ISSN: 1476-4687. http://dx.doi.org/10.1038/nature07153 (2008).

27. Johnston, K. V., Zhao, H., Spergel, D. N. & Hernquist, L. Tidal streams as probes of the Galactic potential. *The Astrophysical Journal Letters* **512,** L109 (1999).

28. Bovy, J., Erkal, D. & Sanders, J. L. Linear perturbation theory for tidal streams and the small-scale CDM power spectrum. *Monthly Notices of the Royal Astronomical Society* **466,** 628–668 (2017).

29. Banik, N., Bovy, J., Bertone, G., Erkal, D. & de Boer, T. Novel constraints on the particle nature of dark matter from stellar streams. *Journal of Cosmology and Astroparticle Physics* **2021,** 043. ISSN: 1475-7516. http://dx.doi.org/10.1088/1475-7516/2021/10/043 (2021).

30. Lin, T. *TASI lectures on dark matter models and direct detection* 2019. arXiv: 1904.07915 [hep-ph].

31. Sin, S.-J. Late-time phase transition and the galactic halo as a Bose liquid. *Physical Review D* **50,** 3650 (1994).

32. Klypin, A., Kravtsov, A. V., Valenzuela, O. & Prada, F. Where are the missing galactic satellites? *The Astrophysical Journal* **522,** 82 (1999).

33. Boylan-Kolchin, M., Bullock, J. & Kaplinghat, M. Too big to fail? The puzzling darkness of massive Milky Way subhaloes, MNRAS 415 (July, 2011) L40–L44. *arXiv preprint arXiv:1103.0007.*

34. Baudis, L. The search for dark matter. *European Review* **26,** 70–81 (2018).

35. Peccei, R. D. & Quinn, H. R. Constraints imposed by CP conservation in the presence of pseudoparticles. *Phys. Rev. D* **16,** 1791–1797. https://link.aps.org/doi/10.1103/PhysRevD.16.1791 (6 1977).

36. Goldstone, J., Salam, A. & Weinberg, S. Broken symmetries. *Physical Review* **127,** 965 (1962).

37. Turner, M. S. Windows on the Axion. *Physics Reports* **197,** 67–97 (1990).

38. Ballou, R. *et al.* New exclusion limits on scalar and pseudoscalar axionlike particles from light shining through a wall. *Physical Review D* **92.** ISSN: 1550-2368. http://dx.doi.org/10.1103/PhysRevD.92.092002 (2015).

39. Ferreira, E. G. M. *Ultra-Light Dark Matter* 2021. arXiv: 2005.03254 [astro-ph.CO].

40. Tremaine, S. & Gunn, J. E. Dynamical role of light neutral leptons in cosmology. *Physical Review Letters* **42,** 407 (1979).

41. Davoudiasl, H., Denton, P. B. & McGady, D. A. Ultralight fermionic dark matter. *Physical Review D* **103,** 055014 (2021).

42. Boyarsky, A., Ruchayskiy, O. & Iakubovskyi, D. A lower bound on the mass of dark matter particles. *Journal of Cosmology and Astroparticle Physics* **2009,** 005–005. ISSN: 1475-7516. http://dx.doi.org/10.1088/1475-7516/2009/03/005 (2009).

43. Lee, B. W. & Weinberg, S. Cosmological Lower Bound on Heavy-Neutrino Masses. *Phys. Rev. Lett.* **39,** 165–168. https://link.aps.org/doi/10.1103/PhysRevLett.39.165 (4 1977).

44. Pospelov, M., Ritz, A. & Voloshin, M. Secluded WIMP dark matter. *Physics Letters B* **662,** 53–61. ISSN: 0370-2693. http://dx.doi.org/10.1016/j.physletb.2008.02.052 (2008).

45. Dodelson, S. & Widrow, L. M. Sterile neutrinos as dark matter. *Physical Review Letters* **72,** 17–20. ISSN: 0031-9007. http://dx.doi.org/10.1103/PhysRevLett.72.17 (1994).

46. Boyarsky, A., Drewes, M., Lasserre, T., Mertens, S. & Ruchayskiy, O. Sterile neutrino Dark Matter. *Progress in Particle and Nuclear Physics* **104,** 1–45. ISSN: 0146-6410. http://dx.doi.org/10.1016/j.ppnp.2018.07.004 (2019).

47. Adhikari, R. *et al.* A White Paper on keV sterile neutrino Dark Matter. *Journal of Cosmology and Astroparticle Physics* **2017,** 025–025. ISSN: 1475-7516. http://dx.doi.org/10.1088/1475-7516/2017/01/025 (2017).

48. Martin, S. P. *A Supersymmetry Primer* 2016. arXiv: hep-ph/9709356 [hep-ph].

49. Servant, G. & Tait, T. M. Is the lightest Kaluza–Klein particle a viable dark matter candidate? *Nuclear Physics B* **650,** 391–419. ISSN: 0550-3213. http://dx.doi.org/10.1016/S0550-3213(02)01012-X (2003).

50. Birkedal, A., Noble, A., Perelstein, M. & Spray, A. Little Higgs dark matter. *Physical Review D* **74.** ISSN: 1550-2368. http://dx.doi.org/10.1103/PhysRevD.74.035002 (2006).

51. Bauer, M. & Plehn, T. *Yet another introduction to dark matter* 2018.

52. Dodelson, S. Modern Cosmology Academic Press (2003). *See particularly.*

53. Hogenbirk, E. *DMPlots* version v1.1.0. 2018. https://doi.org/10.5281/zenodo.1479669.

54. Kobzarev, I. Y., Okun, L. B. & Pomeranchuk, I. Y. On the possibility of experimental observation of mirror particles. *Sov. J. Nucl. Phys.* **3,** 837–841 (1966).

55. Kaplan, D. E., Krnjaic, G. Z., Rehermann, K. R. & Wells, C. M. Atomic dark matter. *Journal of Cosmology and Astroparticle Physics* **2010,** 021–021. ISSN: 1475-7516. http://dx.doi.org/10.1088/1475-7516/2010/05/021 (2010).

56. Cline, J. M. *Dark atoms and composite dark matter* 2021. arXiv: 2108.10314 [hep-ph].

57. Milgrom, M. A modification of the Newtonian dynamics as a possible alternative to the hidden mass hypothesis. *The Astrophysical Journal* **270,** 365–370 (1983).

58. Bekenstein, J. Relativistic gravitational theory for the MOND paradigm. *Phys. Rev. D* **70** (2005).

59. Dodelson, S. The real problem with MOND. *International Journal of Modern Physics D* **20,** 2749–2753 (2011).

60. Abbott, B. P. *et al.* GW170817: observation of gravitational waves from a binary neutron star inspiral. *Physical review letters* **119,** 161101 (2017).

61. Kahya, E. & Woodard, R. A generic test of modified gravity models which emulate dark matter. *Physics Letters B* **652,** 213–216 (2007).

62. Boran, S., Desai, S., Kahya, E. & Woodard, R. GW170817 falsifies dark matter emulators. *Physical Review D* **97,** 041501 (2018).

63. Boveia, A. & Doglioni, C. Dark matter searches at colliders. *Annual Review of Nuclear and Particle Science* **68,** 429–459 (2018).

64. Kahlhoefer, F. Review of LHC dark matter searches. *International Journal of Modern Physics A* **32,** 1730006 (2017).

65. Ackermann, M. *et al.* TheFermiGalactic Center GeV Excess and Implications for Dark Matter. *The Astrophysical Journal* **840,** 43. ISSN: 1538-4357. http://dx.doi.org/10.3847/1538-4357/aa6cab (2017).

66. Goodman, M. W. & Witten, E. Detectability of certain dark-matter candidates. *Phys. Rev. D* **31,** 3059–3063. https://link.aps.org/doi/10.1103/PhysRevD.31.3059 (12 1985).

67. Aprile, E. *et al.* Exclusion of leptophilic dark matter models using XENON100 electronic recoil data. *Science* **349,** 851–854 (2015).

68. Evans, N. W., O'Hare, C. A. J. & McCabe, C. *SHM^{++}: A Refinement of the Standard Halo Model for Dark Matter Searches in Light of the Gaia Sausage* 2018. https://arxiv.org/abs/1810.11468.

69. Baxter, D. *et al.* Recommended conventions for reporting results from direct dark matter searches. *Eur. Phys. J. C* **81,** 907. arXiv: 2105.00599 [hep-ex] (2021).

70. Lewin, J. & Smith, P. Review of mathematics, numerical factors, and corrections for dark matter experiments based on elastic nuclear recoil. *Astroparticle Physics* **6,** 87–112 (1996).

71. Schnee, R. W. in *Physics of the Large and the Small: TASI 2009* 775–829 (World Scientific, 2011).

72. Freese, K., Lisanti, M. & Savage, C. Annual modulation of dark matter: a review. *arXiv preprint arXiv:1209.3339* (2012).

73. Schumann, M. Direct detection of WIMP dark matter: concepts and status. *Journal of Physics G: Nuclear and Particle Physics* **46,** 103003. ISSN: 1361-6471. http://dx.doi.org/10.1088/1361-6471/ab2ea5 (2019).

74. Dūda, G., Kemper, A. & Gondolo, P. Model-independent form factors for spin-independent neutralino–nucleon scattering from elastic electron scattering data. *Journal of Cosmology and Astroparticle Physics* **2007,** 012 (2007).

75. Helm, R. H. Inelastic and elastic scattering of 187-Mev electrons from selected even-even nuclei. *Physical Review* **104,** 1466 (1956).

76. Engel, J. Nuclear form factors for the scattering of weakly interacting massive particles. *Physics Letters B* **264,** 114–119 (1991).

77. Ressell, M. & Dean, D. Spin-dependent neutralino-nucleus scattering for A 127 nuclei. *Physical Review C* **56,** 535 (1997).

78. Preskill, J., Wise, M. B. & Wilczek, F. Cosmology of the invisible axion. *Physics Letters B* **120,** 127–132 (1983).

79. Dimopoulos, S., Frieman, J., Lynn, B. W. & Starkman, G. D. Axiorecombination: a new mechanism for stellar axion production. *Physics Letters B* **179,** 223–227 (1986).

80. Redondo, J. Solar axion flux from the axion-electron coupling. *Journal of Cosmology and Astroparticle Physics* **2013,** 008 (2013).

81. Moriyama, S. Proposal to search for a monochromatic component of solar axions using 57 Fe. *Physical review letters* **75,** 3222 (1995).

82. Andriamonje, S. *et al.* Search for 14.4 keV solar axions emitted in the M1-transition of 57Fe nuclei with CAST. *Journal of Cosmology and Astroparticle Physics* **2009,** 002 (2009).

83. Primakoff, H. Photo-production of neutral mesons in nuclear electric fields and the mean life of the neutral meson. *Physical Review* **81,** 899 (1951).

84. Peccei, R. D., Kuster, M., Raffelt, G. & Beltrán, B. Axions: Theory, cosmology, and experimental searches (2008).

85. Dimopoulos, S., Starkman, G. D. & Lynn, B. W. Atomic enhancements in the detection of axions. *Modern Physics Letters A* **1,** 491–500 (1986).

86. Dimopoulos, S., Starkman, G. D. & Lynn, B. W. Atomic enhancements in the detection of weakly interacting particles. *Physics Letters B* **168,** 145–150 (1986).

87. Shockley, E. *Study of Excess Electronic Recoil Events in XENON1T* (The University of Chicago, 2020).

88. Abe, T., Hamaguchi, K. & Nagata, N. Atomic form factors and inverse Primakoff scattering of axion. *Physics Letters B* **815,** 136174. ISSN: 0370-2693. `http://dx.doi.org/10.1016/j.physletb.2021.136174` (2021).

89. Dent, J. B., Dutta, B., Newstead, J. L. & Thompson, A. Inverse Primakoff Scattering as a Probe of Solar Axions at Liquid Xenon Direct Detection Experiments. *Physical Review Letters* **125.** ISSN: 1079-7114. `http://dx.doi.org/10.1103/PhysRevLett.125.131805` (2020).

90. Ye, J. XENON Collaboration internal communication (2021).

91. Giunti, C. & Studenikin, A. Neutrino electromagnetic properties. *Physics of Atomic Nuclei* **72,** 2089–2125 (2009).

92. Bell, N. F., Gorchtein, M., Ramsey-Musolf, M. J., Vogel, P. & Wang, P. Model independent bounds on magnetic moments of Majorana neutrinos. *Physics Letters B* **642,** 377–383 (2006).

93. Fujikawa, K. & Shrock, R. E. Magnetic moment of a massive neutrino and neutrino-spin rotation. *Physical Review Letters* **45,** 963 (1980).

94. Agostini, M. *et al.* Limiting neutrino magnetic moments with Borexino Phase-II solar neutrino data. *Physical Review D* **96,** 091103 (2017).

95. Arceo-Díaz, S., Schröder, K.-P., Zuber, K. & Jack, D. Constraint on the magnetic dipole moment of neutrinos by the tip-RGB luminosity in ω-Centauri. *Astroparticle Physics* **70,** 1–11 (2015).

96. Díaz, S. A., Schröder, K.-P., Zuber, K., Jack, D. & Barrios, E. E. B. Constraint on the axion-electron coupling constant and the neutrino magnetic dipole moment by using the tip-RGB luminosity of fifty globular clusters. *arXiv preprint arXiv:1910.10568* (2019).

97. Vogel, P. & Engel, J. Neutrino electromagnetic form factors. *Physical Review D* **39,** 3378 (1989).

98. Pospelov, M., Ritz, A. & Voloshin, M. Bosonic super-WIMPs as keV-scale dark matter. *Physical Review D* **78,** 115012 (2008).

99. Arisaka, K. *et al.* Expected sensitivity to galactic/solar axions and bosonic super-WIMPs based on the axio-electric effect in liquid xenon dark matter detectors. *Astroparticle Physics* **44,** 59–67 (2013).

100. Plante, G. *The XENON100 dark matter experiment: design, construction, calibration and 2010 search results with improved measurement of the scintillation response of liquid xenon to low-energy nuclear recoils* PhD thesis (Columbia University, 2012).

101. Stampfli, P. Theory for the electron affinity of clusters of rare gas atoms and polar molecules. *Physics Reports* **255,** 1–77 (1995).

102. Aprile, E. *et al.* Constraining the Spin-Dependent WIMP-Nucleon Cross Sections with XENON1T. *Physical Review Letters* **122.** ISSN: 1079-7114. `http://dx.doi.org/10.1103/PhysRevLett.122.141301` (2019).

103. Aprile, E. *et al.* Observation of two-neutrino double electron capture in 124Xe with XENON1T. *Nature* **568,** 532–535. ISSN: 1476-4687. `http://dx.doi.org/10.1038/s41586-019-1124-4` (2019).

104. Albert, J. B. *et al.* Improved measurement of the 2νββ half-life of136Xe with the EXO-200 detector. *Physical Review C* **89.** ISSN: 1089-490X. `http://dx.doi.org/10.1103/PhysRevC.89.015502` (2014).

105. Aprile, E. & Doke, T. Liquid xenon detectors for particle physics and astrophysics. *Reviews of Modern Physics* **82,** 2053 (2010).

106. Althüser, L. *Light collection efficiency simulations of the xenon1t experiment and comparison to data* (2017).

107. Jortner, J., Meyer, L., Rice, S. A. & Wilson, E. Localized excitations in condensed ne, ar, kr, and xe. *The Journal of chemical physics* **42,** 4250–4253 (1965).

108. Hitachi, A. Properties of liquid xenon scintillation for dark matter searches. *Astroparticle Physics* **24,** 247–256 (2005).

109. Szydagis, M. *et al.* NEST: a comprehensive model for scintillation yield in liquid xenon. *Journal of Instrumentation* **6,** P10002–P10002. `https://doi.org/10.1088%2F1748-0221%2F6%2F10%2Fp10002` (2011).

110. Szydagis, M. *et al.* A Review of NEST Models, and Their Application to Improvement of Particle Identification in Liquid Xenon Experiments. arXiv: `2211.10726 [hep-ex]` (2022).

111. Aprile, E. *et al.* The XENONnT Dark Matter Experiment (2024).

112. Aprile, E. *et al.* XENONnT Technical Design Report (2018).

113. Aprile, E., Bolotnikov, A. E., Bolozdynya, A. I. & Doke, T. *Noble gas detectors* (John Wiley & Sons, 2006).

114. Aprile, E. *et al.* Dark Matter Search Results from a One Tonne Year Exposure of XENON1T. *arXiv preprint arXiv:1805.12562* (2018).

115. Aalbers, J. *et al.* First dark matter search results from the LUX-ZEPLIN (LZ) experiment. *arXiv preprint arXiv:2207.03764* (2022).

116. Aprile, E. *et al.* Conceptual design and simulation of a water Cherenkov muon veto for the XENON1T experiment. *Journal of instrumentation* **9,** P11006 (2014).

117. Aprile, E. *et al.* Projected WIMP sensitivity of the XENONnT dark matter experiment. *Journal of Cosmology and Astroparticle Physics* **2020,** 031 (2020).

118. Leinweber, G. *et al.* Neutron capture and total cross-section measurements and resonance parameters of gadolinium. *Nuclear Science and Engineering* **154,** 261–279 (2006).

119. Platzman, R. Total ionization in gases by high-energy particles: An appraisal of our understanding. *The International Journal of Applied Radiation and Isotopes* **10,** 116–127 (1961).

120. Aprile, E. *et al.* The XENON1T data acquisition system. *JINST* **14,** P07016–P07016 (2019).

121. Aprile, E. *et al.* Light Dark Matter Search with Ionization Signals in XENON1T. *Physical Review Letters* **123.** `https://doi.org/10.1103%2Fphysrevlett.123.251801` (2019).

122. Aprile, E. *et al.* Emission of Single and Few Electrons in XENON1T and Limits on Light Dark Matter. *arXiv preprint arXiv:2112.12116* (2021).

123. Redshaw, M., Wingfield, E., McDaniel, J. & Myers, E. G. Mass and Double-Beta-Decay Q Value of Xe 136. *Physical review letters* **98,** 053003 (2007).

124. Hamamatsu Photonics. *Photomultiplier Tubes and assemblies* (Apr. 2017).

125. Antochi, V. *et al.* Improved quality tests of R11410-21 photomultiplier tubes for the XENONnT experiment. *Journal of Instrumentation* **16,** P08033. `https://doi.org/10.1088/1748-0221/16/08/p08033` (2021).

126. Tintori, C. WP2081 digital pulse processing in nuclear physics. *CAEN White Paper,* 1–21 (2011).

127. CAEN. `https://caen.it`.

128. CAEN. *User Manual UM5954 DPP-DAW Digital Pulse Processing for Dynamic Acquisition Window* 2019.

129. *Digital Pulse Processor for Nuclear Physics* SkuTek Instrumentation (Sept. 27, 2023). `https://www.skutek.com/ddc10_box.htm`.

130. Elykov, A. *Background modeling & data acquisition for XENON detectors* PhD thesis (Dissertation, Universität Freiburg, 2021, 2021).

131. De Deo, M. *et al.* Accurate GPS-based timestamp facility for Gran Sasso National Laboratory. *JINST* **14,** P04001–P04001 (2019).

132. Antonioli, P. *et al.* SNEWS: the supernova early warning system. *New Journal of Physics* **6,** 114 (2004).

133. Fujitsu. `https://www.fujitsu.com/global/`.

134. Weil, S. A., Brandt, S. A., Miller, E. L., Long, D. D. & Maltzahn, C. *Ceph: A scalable, high-performance distributed file system* in *Proceedings of the 7th symposium on Operating systems design and implementation* (2006), 307–320.

135. *CRU understanding RAID* `https://www.cru-inc.com/data-protection-topics/understanding-raid/`. Nov. 23, 2022.

136. Barisits, M. *et al.* Rucio: Scientific data management. *Computing and Software for Big Science* **3,** 1–19 (2019).

137. Aprile, E. *et al.* Conceptual design and simulation of a water Cherenkov muon veto for the XENON1T experiment. *Journal of Instrumentation* **9,** P11006–P11006. `https://doi.org/10.1088%2F1748-0221%2F9%2F11%2Fp11006` (2014).

138. Masson, D. *et al. AxFoundation/redax: Version 2.3.0* version v2.3.0. 2022. `https://doi.org/10.5281/zenodo.5882717`.

139. MongoDB. `https://mongodb.com`.

140. Angevaare, J. R. *et al. XENONnT/straxen: v1.2.4* version v1.2.4. 2022. `https://doi.org/10.5281/zenodo.5834311`.

141. Aalbers, J. *et al. AxFoundation/strax: v1.1.5* version v1.1.5. 2022. `https://doi.org/10.5281/zenodo.5833114`.

142. Harris, C. R. *et al.* Array programming with NumPy. *Nature* **585,** 357–362 (2020).

143. Pivarski, J., Lange, D. & Jatuphattharachat, T. *Toward real-time data query systems in HEP* 2017. https://arxiv.org/abs/1711.01229.

144. Harris, C. R. *et al.* Array programming with NumPy. *Nature* **585,** 357–362. https://doi.org/10.1038/s41586-020-2649-2 (2020).

145. Lam, S. K., Pitrou, A. & Seibert, S. *Numba: A LLVM-based python JIT compiler* in *Proceedings of the Second Workshop on the LLVM Compiler Infrastructure in HPC* (2015), 1–6.

146. Aalbers, J. & Tunnell, C. The pax data processor v6.4.2 (2017).

147. Slack. https://www.slack.com/. Nov. 23, 2022.

148. Aprile, E. *et al.* The Triggerless Data Acquisition System of the XENONnT Experiment. *arXiv preprint arXiv:2212.11032* (2022).

149. Agnes, P. *et al.* The Electronics and Data Acquisition System of the DarkSide Dark Matter Search. *arXiv preprint arXiv:1412.2969* (2014).

150. Agostinelli, S. *et al.* GEANT4—a simulation toolkit. *Nuclear instruments and methods in physics research section A: Accelerators, Spectrometers, Detectors and Associated Equipment* **506,** 250–303 (2003).

151. García, D. R. *et al. XENONnT/epix: v0.3.4* version v0.3.4. 2023. https://doi.org/10.5281/zenodo.7777552.

152. Zhu, T. & Gaemers, P. W. *github.com/XENONnT/WFSim: v0.15.13* version v0.5.13. 2022. https://doi.org/10.5281/zenodo.5865873.

153. Buncic, P. *et al. CernVM–a virtual software appliance for LHC applications* in *Journal of Physics: Conference Series* **219** (2010), 042003.

154. Ramírez García, D. *Simulating the XENONnT dark matter experiment: backgrounds and WIMP sensitivity* PhD thesis (Dissertation, Universität Freiburg, 2022).

155. Pia, M. G., Basaglia, T., Bell, Z. W. & Dressendorfer, P. V. *Geant4 in scientific literature* in *2009 IEEE nuclear science symposium conference record (NSS/MIC)* (2009), 189–194.

156. Brown, D. A. *et al.* ENDF/B-VIII. 0: the 8th major release of the nuclear reaction data library with CIELO-project cross sections, new standards and thermal scattering data. *Nuclear Data Sheets* **148,** 1–142 (2018).

157. Hitachi, A. *et al.* Effect of ionization density on the time dependence of luminescence from liquid argon and xenon. *Physical Review B* **27,** 5279 (1983).

158. Kubota, S., Hishida, M., Suzuki, M. & Ruan(Gen), J.-z. Dynamical behavior of free electrons in the recombination process in liquid argon, krypton, and xenon. *Phys. Rev. B* **20,** 3486 (1979).

159. Albert, J. *et al.* Measurement of the drift velocity and transverse diffusion of electrons in liquid xenon with the EXO-200 detector. *Physical Review C* **95,** 025502 (2017).

160. Kaufman, L. J. *Measurements of electron transport in liquid and gas Xenon using a laser-driven photocathode* tech. rep. (SLAC National Accelerator Lab., Menlo Park, CA (United States)).

161. Sorensen, P. Anisotropic diffusion of electrons in liquid xenon with application to improving the sensitivity of direct dark matter searches. *Nuclear Instruments and Methods in Physics Research Section A: Accelerators, Spectrometers, Detectors and Associated Equipment* **635,** 41–43 (2011).

162. Veenhof, R. *Garfield, a drift chamber simulation program* in *Conf. Proc. C* **9306149** (1993), 66–71.

163. Aprile, E. *et al.* Search for new physics in electronic recoil data from XENONnT. *Physical Review Letters* **129,** 161805 (2022).

164. Haselschwardt, S., Kostensalo, J., Mougeot, X. & Suhonen, J. Improved calculations of β decay backgrounds to new physics in liquid xenon detectors. *Physical Review C* **102,** 065501 (2020).

165. Aprile, E. *et al.* Excess electronic recoil events in XENON1T. *Physical Review D* **102,** 072004 (2020).

166. Aprile, E. *et al.* Double-weak decays of Xe 124 and Xe 136 in the XENON1T and XENONnT experiments. *Physical Review C* **106,** 024328 (2022).

167. Kotila, J. & Iachello, F. Phase-space factors for double-β decay. *Physical Review C* **85,** 034316 (2012).

168. Blatt, J. M. & Weisskopf, V. F. *Theoretical nuclear physics* (Courier Corporation, 1991).

169. Mougeot, X. *BetaShape: A new code for improved analytical calculations of beta spectra* in *EPJ Web of Conferences* **146** (2017), 12015.

170. Behrens, H. & Bühring, W. *Electron radial wave functions and nuclear betadecay* **67** (Oxford University Press, USA, 1982).

171. Mougeot, X. Reliability of usual assumptions in the calculation of β and ν spectra. *Physical Review C* **91,** 055504 (2015).

172. Sirlin, A. General properties of the electromagnetic corrections to the beta decay of a physical nucleon. *Physical Review* **164,** 1767 (1967).

173. Rose, M. E. A note on the possible effect of screening in the theory of beta-disintegration. *Physical Review* **49,** 727 (1936).

174. Salvat, F., Martnez, J., Mayol, R. & Parellada, J. Analytical dirac-hartree-fock-slater screening function for atoms (z= 1–92). *Physical Review A* **36,** 467 (1987).

175. Ejiri, H., Suhonen, J. & Zuber, K. Neutrino–nuclear responses for astro-neutrinos, single beta decays and double beta decays. *Physics Reports* **797,** 1–102 (2019).

176. Fuselli, C. *Beta decays in XENONnT* (Master Thesis, University of Amsterdam, 2022).

177. Laboratoire National Henri Becquerel. *Table de Radio nucleides* 2010. `http://www.nucleide.org/DDEP_WG/DDEPdata.htm`.

178. Nisi, S., Di Vacri, A., Di Vacri, M., Stramenga, A. & Laubenstein, M. Comparison of inductively coupled mass spectrometry and ultra low-level gamma-ray spectroscopy for ultra low background material selection. *Applied Radiation and Isotopes* **67,** 828–832 (2009).

179. Aprile, E. *et al.* Material radiopurity control in the XENONnT experiment. *arXiv preprint arXiv:2112.05629* (2021).

180. Aprile, E. *et al.* XENON1T dark matter data analysis: Signal and background models and statistical inference. *Phys. Rev. D* **99,** 112009. `https://link.aps.org/doi/10.1103/PhysRevD.99.112009` (11 2019).

181. Breur, P. A. *Backgrounds in XENON1T* PhD thesis (University of Amsterdam, Amsterdam The Netherlands, 2019).

182. Ahlswede, J., Hebel, S., Ross, J. O., Schoetter, R. & Kalinowski, M. B. Update and improvement of the global krypton-85 emission inventory. *Journal of environmental radioactivity* **115,** 34–42 (2013).

183. Aprile, E. *et al.* Observation of two-neutrino double electron capture in 124Xe with XENON1T. *Nature* **568** (2019).

184. EXO-200 Collaboration and others. J. Albert et al., An improved measurement of the $2\nu\beta\beta$ half-life of Xe-136 with EXO-200. *arXiv preprint arXiv:1306.6106.*

185. Chen, J.-W., Chi, H.-C., Liu, C.-P. & Wu, C.-P. Low-energy electronic recoil in xenon detectors by solar neutrinos. *Physics Letters B* **774,** 656–661 (2017).

186. Wenz, D. XENON Collaboration internal communication (2021).

187. Newstead, J. L., Lang, R. F. & Strigari, L. E. Atmospheric neutrinos in next-generation xenon and argon dark matter experiments. *Physical Review D* **104,** 115022 (2021).

188. Billard, J., Figueroa-Feliciano, E. & Strigari, L. Implication of neutrino backgrounds on the reach of next generation dark matter direct detection experiments. *Physical Review D* **89,** 023524 (2014).

189. Bé, M.-M. *et al.* Table of radionuclides (Vol. 1-A= 1 to 150). *Bureau International des Poids et Mesures, France: Sèvres,* 10–45 (2004).

190. Cichon, D. XENON Collaboration internal communication (2021).

191. Baker, S. & Cousins, R. D. Clarification of the Use of Chi Square and Likelihood Functions in Fits to Histograms. *Nucl. Instrum. Meth.* **221,** 437–442 (1984).

192. Albert, J. *et al.* Measurements of the ion fraction and mobility of α- and β-decay products in liquid xenon using the EXO-200 detector. *Physical Review C* **92,** 045504 (2015).

193. Murra, M., Schulte, D., Huhmann, C. & Weinheimer, C. Design, construction and commissioning of a high-flow radon removal system for XENONnT. *arXiv preprint arXiv:2205.11492* (2022).

194. Aalbers, J., Pelssers, B., Antochi, V. C., Tan, P. L. & Conrad, J. Finding dark matter faster with explicit profile likelihoods. *Physical Review D* **102,** 072010 (2020).

195. TensorFlow Developers. *TensorFlow* version v2.5.0. 2021. `https://doi.org/10.5281/zenodo.4758419`.

196. James, R., Palmer, J., Kaboth, A., Ghag, C. & Aalbers, J. FlameNEST: explicit profile likelihoods with the Noble Element Simulation Technique. *Journal of Instrumentation* **17,** P08012 (2022).

197. Aprile, E. *et al.* First dark matter search with nuclear recoils from the XENONnT experiment. *Physical Review Letters* **131,** 041003 (2023).

198. Wilks, S. S. The large-sample distribution of the likelihood ratio for testing composite hypotheses. *The annals of mathematical statistics* **9,** 60–62 (1938).

199. Bishara, F., Brod, J., Grinstein, B. & Zupan, J. Chiral effective theory of dark matter direct detection. *Journal of Cosmology and Astroparticle Physics* **2017,** 009 (2017).

200. Hoferichter, M., Klos, P., Menéndez, J. & Schwenk, A. Dark-matter-nucleus scattering in chiral effective field theory. *arXiv preprint arXiv:1903.11075* (2019).